Downloaded from orbit.dtu.dk on: May 05, 2023

DTU Library

Development of tomographic reconstruction methods in materials science with focus on advanced scanning methods

Lyckegaard, Allan

Publication date:
2011

Document Version
Publisher's PDF, also known as Version of record

Link back to DTU Orbit

Citation (APA):
Lyckegaard, A. (2011). *Development of tomographic reconstruction methods in materials science with focus on advanced scanning methods*. Risø National Laboratory for Sustainable Energy, Technical University of Denmark. Risø-PhD No. 73(EN)

General rights
Copyright and moral rights for the publications made accessible in the public portal are retained by the authors and/or other copyright owners and it is a condition of accessing publications that users recognise and abide by the legal requirements associated with these rights.

- Users may download and print one copy of any publication from the public portal for the purpose of private study or research.
- You may not further distribute the material or use it for any profit-making activity or commercial gain
- You may freely distribute the URL identifying the publication in the public portal

If you believe that this document breaches copyright please contact us providing details, and we will remove access to the work immediately and investigate your claim.

Development of tomographic reconstruction methods in materials science with focus on advanced scanning methods

Risø-PhD-Report

Allan Lyckegaard
Risø–PhD–73(EN)
June 2011

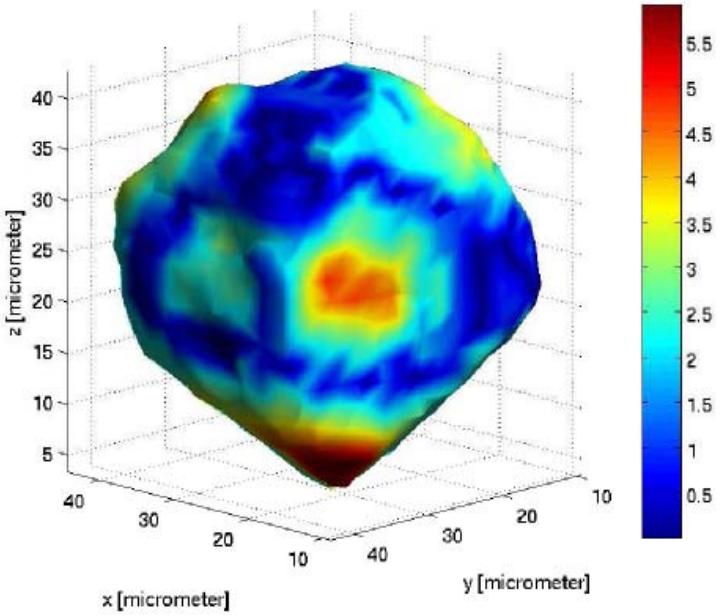

Risø DTU
National Laboratory for Sustainable Energy

Author: Allan Lyckegaard
Title: Development of tomographic reconstruction methods in materials science with focus on advanced scanning methods
Division: Materials

Risø-PhD-73
January 2011

Abstract (max. 2000 char.):
Techniques for obtaining 3 dimensional information of individual crystals, socalled grains, in polycrystalline materials are important within the eld of materials science for understanding and modeling the behavior of materials.In the last decade, a number of non-destructive X-ray diffraction techniques have been developed, which basically group into two classes: imaging techniques and scanning techniques each having their advantages and drawbacks. The imaging techniques have fast acquisition times but have reached the limit in resolution and the scanning techniques suffer from slow acquisition times.
The purpose of this PhD-project is to develop and implement a new technique, the Boxscan technique, which positions itself between imaging and scanning techniques. The Boxscan technique bases its spatial information on a scanning approach but uses extended line-beams known from the imaging techniques.
Combining this with a novel 6-dimensional indexing routine it is possible to determine grain centers, radii and orientations of hundreds of individual grains in a sample. The grain centers are found with a precision which is better than the stepping size, and thus provides a road towards future non-destructive 3D studies of nanomaterials.
It is furthermore shown that the Boxscan technique can be extended to provide full 3D grain maps by using either Laguerre tessellations or iterative reconstruction methods such as e.g. the algebraic reconstruction technique (ART). A 3D grain map of a meta-stable beta titanium alloy comprising 1265 grains has been produced as part of a collaboration on spatial resolved strain measurements with Cornell University, USA, and the Advanced Photon Source, USA.

ISBN 978-87-550-3882-0

Sponsorship:
Grundforskningsfonden. The Danish National Research Foundation.

Cover : The distance between the surface of a grain reconstructed using the algebraic reconstruction technique and a verication grain found using phase contrast tomography. The colors denote the distance

Information Service Department
Risø National Laboratory for Sustainable Energy
Technical University of Denmark
P.O.Box 49
DK-4000 Roskilde
Denmark
Telephone +45 46774005
bibl@risoe.dtu.dk
Fax +45 46774013
www.risoe.dtu.dk

Abstract

Techniques for obtaining 3 dimensional information of individual crystals, so-called grains, in polycrystalline materials are important within the field of materials science for understanding and modeling the behavior of materials.In the last decade, a number of non-destructive X-ray diffraction techniques have been developed, which basically group into two classes: imaging techniques and scanning techniques each having their advantages and drawbacks. The imaging techniques have fast acquisition times but have reached the limit in resolution and the scanning techniques suffer from slow acquisition times.

The purpose of this PhD-project is to develop and implement a new technique, the Boxscan technique, which positions itself between imaging and scanning techniques. The Boxscan technique bases its spatial information on a scanning approach but uses extended line-beams known from the imaging techniques. Combining this with a novel 6-dimensional indexing routine it is possible to determine grain centers, radii and orientations of hundreds of individual grains in a sample. The grain centers are found with a precision which is better than the stepping size, and thus provides a road towards future non-destructive 3D studies of nanomaterials.

It is furthermore shown that the Boxscan technique can be extended to provide full 3D grain maps by using either Laguerre tessellations or iterative reconstruction methods such as e.g. the algebraic reconstruction technique (ART). A 3D grain map of a meta-stable beta titanium alloy comprising 1265 grains has been produced as part of a collaboration on spatial resolved strain measurements with Cornell University, USA, and the Advanced Photon Source, USA.

Resumé

Teknikker til at opnå 3-dimensionel information om de enkelte krystaller, såkaldte korn, i polykrystalline materialer er vigtige indenfor materialeforskningen for at forstå og modellere materiallers egenskaber. Indenfor det sidste årti er der blevet udviklet et antal ikke-destruktive røntgendiffraktionsteknikker som indddeler sig i to grupper: billeddannende teknikker og skanneteknikker som hver især har deres fordele og ulemper. De billeddannende teknikker måler hurtigt men har nået grænsen for opløsning og skanneteknikkerne måler meget langsomt.

Formålet med dette ph.d-projekt er at udvikle og implementere en ny teknik, Boxscan-teknikken, som lægger sig i mellem de billeddannende teknikker og skannenteknikkerne. Boxscan-teknikken baserer den spatielle information på skanning men benytter en udvidet linje-røntgenstråle som er kendt fra de billeddannende teknikker. En kombination af dette og en ny 6-dimensionel indekseringsrutine muliggør bestemmelse af korncentre, radius og orientering af hundredvis af individuelle korn i en prøve. Korncentrene er fundet med en præcision som er bedre end afstanden imellem målepunkter med røntgenstrålen og viser derfor vejen imod fremtidige 3D studier af nanomaterialer.

Endvidere er det vist at Boxscan-teknikken kan udvides til at producdere 3D kornmaps ved at benytte Laguerre tessellations eller en iterative teknik som f.eks. algebraic reconstruction technique (ART). Et 3D kornmap af en metastabil beta-titanium-legering med 1265 korn er blevet produceret som del af et samarbejde i mellem Cornell University, USA og Advances Photon Source, USA.

Preface

This PhD-project was carried out within the Centre of Fundamental Research: Metal Structures in Four Dimensions at Risø-DTU, Technical University of Denmark. The fundings from The Danish National Research Foundation are gratefully acknowledged.
During my PhD I have visited both ESRF in Grenoble, France, and APS in Chicago, USA, for work related to experiments. In relation to this I would like to thank Ulrich Lienart, APS, and Carsten Gundlach, ESRF for making the stays pleasant and for many fruitful discussions.
At the Materials Research Division at Risø I would like to thank all my colleagues. Especially I thank Søren Schmidt, Henning Friis Poulsen, Henning Osholm Sørensen and Andreas Alpers for helping me with many scientific questions throughout my PhD.
The many long hours at the office would have been a lot tougher if it was not for the company of Tianbo, Masafumi and in particular Naoya. I really enjoyed sharing an office with all of you guys.
A special thanks goes to my supervisor Erik Mejdal Lauridsen for much support during the entire project. Even when things seemed impossible you still believed that it was possible and helped over many obstacles in the process of reaching this goal.
Finally, I would like to thank my family and friends for all their support through this PhD-project - both at times where it was tough and where it was not so tough.

Roskilde, January 2011

Allan Lyckegaard

List of publications

During this PhD-project the author has published and submitted articles. The articles are listed here and can be found in the appendix.

On the Use of Laguerre Tessellations for Representations of 3D Grain Structures Allan Lyckegaard, Erik Mejdal Lauridsen, Wolfgang Ludwig, Richard Warren Fonda, Henning Friis Poulsen. *Advanced Engineering Materials*. In print.

Recrystallization Kinetics of 50% Cold-Rolled Aluminium S. O. Poulsen, A. Lyckegaard, J. Oddershede, E. M. Lauridsen, C. Gundlach , C. Curfs and D. Juul Jensen. *Risø International Symposium on Materials Science 31, 2010*, 391-396.

3D grain reconstruction from boxscan data A. Lyckegaard, A. Alpers, W. Ludwig, R.W. Fonda, L. Margulies, A. Götz, H.O. Sørensen, S.R. Dey, H.F. Poulsen and E. M. Lauridsen. *Risø International Symposium on Materials Science 31, 2010*, 329-366.

Correction of Ring Artifacts in X-ray Tomographic Images Allan Lyckegaard, Greg Johnson and Paul Tafforeau. Submittet to *International Journal of Tomography and Statistics*.

List of Figures

1.1 2D surface of the 3D microstructure of duplex steel. 1

2.1 Definition of the unit cell 8
2.2 Plane family for a cubic crystal 8
2.3 X-ray photon elastically scattered from an atom 11

3.1 Experimental setup of the Boxscan technique 16
3.2 Coordinate system definitions 18
3.3 Boxscan z-profile 19
3.4 Boxscan y-profile 20
3.5 Profiles for the same grain at different ω-values 23
3.6 Intersections in real space and Rodrigues space 25
3.7 Schematic layout of the database structure 29
3.8 Detector image of a diffraction signal 30
3.9 Caked detector image 31
3.10 Intensity as a function of η, $I(\eta)$ 32
3.11 (ω, η)-values for spots for a given ring and a given y- or z-position 33
3.12 Profile from experimental data 34
3.13 $x_s y_s$-plane of 6D space 36
3.14 Distribution of grain radius found using the Boxscan technique . 39
3.15 Cross section of the reconstructed D15 sample 40
3.16 Grain structure before and after the ring correction 41
3.17 D15 sample segmented from phase contrast tomography 44
3.18 Subset of Boxscan and phase contrast tomography results 45

4.1 A Voronoi tessellation and a Laguerre tessellation 49
4.2 Laguerre cell 50
4.3 Solution with ART in two dimensions 52
4.4 Feasible region in 2D 56
4.5 Feasible region in 3D 56
4.6 2D slice of grain structure and Laguerre tessellation 60
4.7 3D renderings of grain structures 61
4.8 3D grain size distribution 62
4.9 Distribution of # of wrong neighbors 63

4.10 Grain face distribution 64
4.11 Evolution of the figure of merit 67
4.12 ART versus verification grain 68
4.13 Layer from ART solution 69
4.14 The distance between the grain boundaries 69
4.15 Reconstruction error for beam angle 71
4.16 Reconstruction error for number of beams 71
4.17 Reconstruction error for width of interval 72
4.18 Reconstruction error for step size 73
4.19 Reconstruction error for beam width 74
4.20 Convex and grain shapes 75
4.21 Average of the norm of the reconstruction error 77
4.22 Percent perfect reconstructions for convex and grain shapes . . . 78

5.1 Sample for experiment 82
5.2 Cross-sectional view of the sample 84
5.3 Grain size distribution in the sample 84
5.4 Grain map produced by a Laguerre tesselation 85
5.5 Comparison of grain size distributions 86

List of Tables

1.1 Advantages and drawback for non-destructive techniques 4

3.1 Parameter constraints for in the Levenberg-Marquardt algorithm 32
3.2 Experiment parameters for the D15 Boxscan experiment 37
3.3 Miller indices and 2θ-values for the Boxscan experiment 38
3.4 Steps of the ring correction method 42
3.5 Steps of the ring correction method 43

4.1 Figures of merit for Laguerre and Voronoi tessellations 62
4.2 Average number of grain faces 63
4.3 Average figures of merit 64

5.1 Parameters for the data analysis 83

Contents

Abstract **i**

Resumé **iii**

Preface **v**

List of publications **vii**

1 Introduction and background **1**

2 Diffraction from polycrystals **7**
2.1 Crystals and crystal planes 7
2.1.1 Crystal lattices and unit cells 7
2.1.2 Crystal planes and Miller indices 8
2.1.3 Crystal orientation 8
2.2 X-rays and crystals 10
2.2.1 X-ray sources 10
2.2.2 X-ray scattering 11
2.2.3 Reciprocal space 12
2.3 Summary 13

3 Boxscan Technique **15**
3.1 Experimental setup 15
3.1.1 X-ray beam and slits 15
3.1.2 Rotation stage ω 16
3.1.3 Translation stages x, y, z 16
3.1.4 Detector 17
3.1.5 Additional equipment 17
3.1.6 Coordinate system of the laboratory 17
3.2 Scanning procedure 18
3.2.1 Vertical scan 19
3.2.2 Horizontal scan 20
3.2.3 Boxscan scan versus point scan technique 20
3.3 Indexing in 6 dimensional space 21
3.3.1 Profile information 21

3.3.1.1 Orientation information . . . 21
3.3.1.2 Center of mass information . . . 22
3.3.2 Grain indexing in 6 dimensions . . . 22
3.3.2.1 Profile matching . . . 22
3.3.2.2 Indexing of subinterval . . . 24
3.4 Implementation . . . 26
3.4.1 Data storage and data type definitions . . . 26
3.4.1.1 Rings and hkls . . . 26
3.4.1.2 Images . . . 27
3.4.1.3 Spots . . . 27
3.4.1.4 Reflections . . . 27
3.4.1.5 Profiles . . . 27
3.4.1.6 Matches . . . 28
3.4.1.7 Grains . . . 28
3.4.1.8 Graphical layout of database . . . 28
3.4.2 Data processing . . . 28
3.4.2.1 Initializations . . . 28
3.4.2.2 From images to spots . . . 28
3.4.2.3 From spots to reflections . . . 33
3.4.2.4 From reflections to profiles . . . 34
3.4.2.5 Profile matching . . . 35
3.4.2.6 Grain indexing . . . 35
3.5 Verification of the Boxscan technique . . . 36
3.5.1 Boxscan experiment . . . 37
3.5.1.1 Experimental . . . 37
3.5.1.2 Data analysis . . . 38
3.5.1.3 Results . . . 39
3.5.2 Phase contrast tomography verification experiment . . . 39
3.5.2.1 Experimental . . . 39
3.5.2.2 Data analysis . . . 40
3.5.2.3 Results . . . 41
3.5.3 Comparison . . . 41
3.5.4 Discussion . . . 44

4 Reconstruction of 3D grain maps 47
4.1 Laguerre tessellation-based 3D grain maps . . . 47
4.1.1 Introduction . . . 47
4.1.2 Laguerre tessellations . . . 48
4.1.3 Implementation . . . 50
4.2 Algebraic reconstruction technique . . . 51
4.2.1 Introduction . . . 51
4.2.2 Algebraic Reconstruction Technique . . . 51
4.2.3 Constructing linear systems from boxscan data . . . 52
4.2.4 Implementation . . . 53
4.3 Linear programming . . . 54
4.3.1 Introduction . . . 54

4.3.2 Linear Programming . . . 55
4.3.3 Shape Reconstruction . . . 57
4.3.3.1 Data . . . 57
4.3.3.2 Applying linear programming to shape reconstruction data . . . 57
4.3.3.3 Finding solutions using CPLEX . . . 57
4.4 Verification . . . 58
4.4.1 Laguerre tessellations . . . 58
4.4.1.1 Experimental . . . 58
4.4.1.2 Results . . . 58
4.4.1.3 Discussion . . . 65
4.4.1.4 Summary . . . 65
4.4.2 Algebraic reconstruction technique . . . 66
4.4.2.1 Application to single grain . . . 66
4.4.2.2 Results from single grain . . . 66
4.4.2.3 Discussion on reconstruction of a single grain . . . 67
4.4.2.4 Parameter study . . . 68
4.4.2.5 Results of the parameter study . . . 70
4.4.2.6 Parameter study discussion and conclusion . . . 73
4.4.3 Linear programming . . . 74
4.4.3.1 Data . . . 74
4.4.3.2 Application of CPLEX to data . . . 75
4.4.3.3 Results . . . 76

5 Application of the Boxscan technique 81
5.1 Full volume scan of a β-titanium alloy . . . 81
5.1.1 Introduction . . . 81
5.1.2 Experimental . . . 82
5.1.2.1 Sample . . . 82
5.1.2.2 Boxscan experiment . . . 82
5.1.2.3 Measured data . . . 82
5.1.2.4 Data analysis . . . 83
5.1.3 Results . . . 83
5.1.3.1 Grain centers and grain sizes . . . 83
5.1.3.2 Grain map from Laguerre tessellation . . . 85
5.2 Discussion and conclusion . . . 86

6 Summary and outlook 89

A Publications 93
A.1 On the Use of Laguerre Tessellations for Represention of 3D grain structures . . . 93
A.2 Recrystallization Kinetics of 50% Cold-Rolled Aluminium . . . 100
A.3 3D grain reconstruction from boxscan data . . . 107
A.4 Correction of Ring Artifacts in X-ray Tomographic Images . . . 116

Chapter 1

Introduction and background

In our everyday life we surround ourselves with polycrystalline materials almost everywhere, e.g. metals, rocks, ceramics and ice. A polycrystal is a material which is composed of many small crystals, also known as grains, in a network structure. Each crystal or grain is a set of atoms or molecules arranged in a periodic lattice in three dimensions. Two neighboring grains are distinguished by their lattice orientation, i.e. the rotation of the lattice with respect to a given reference coordinate system. The three dimensional arrangement of the grains in the polycrystal is called the microstructure or grain structure. Figure 1.1 shows the 2D surface of a 3D grain structure. Many macroscopic properties such as mechanical, thermal, magnetic and conductive properties of the material can be directly linked to the microstructure, hence knowledge of the microstucture is invaluable in industrial use and in materials science.

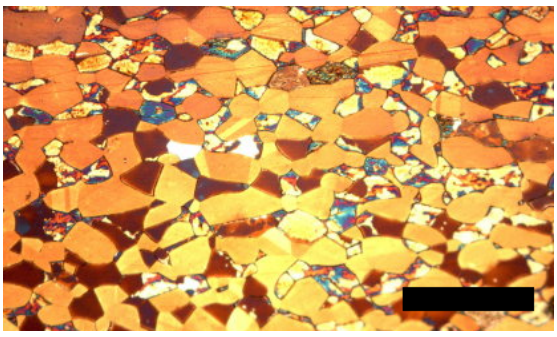

Figure 1.1: 2D surface of the 3D microstructure of duplex steel (ferrite/austenite) as seen through an optical microscope using polarized light. Scale bar corresponds to 100 micrometers.

To acquire knowledge of the microstructure, such as grain size, grain position or grain orientation, a number of methods have been developed through the years. From Sörby's first use of optical microscopes [1] in the late 19th century, the next major step in characterization techniques was the invention of the electron microscope in 1932[2]. The electron microscope has since then been improved into two of the main work horses in materials science: the scanning electron microscope(SEM) [3] and the transmission electron microscope(TEM) [4]. Adding a backscatter camera to the SEM made it possible to measure diffraction patterns from a polycrystal (electron backscatter diffraction, EBSD[5] which are of high interest for materials scientists. Alternatively, the use of a focused low-energy X-ray beam for characterization of individual surface grains was proposed by Hirsch and Keller[6, 7].

All the above mentioned methods are surface methods: Low-energy X-rays penetrate a few micrometers into the surface, electrons less than one micrometer and visible light even less [8]. To examine materials non-destructively in the bulk it is therefore necessary to use alternatives, such as neutrons or high-energy X-rays. Neutrons can penetrate millimeter thick specimens and are therefore useful for studying bulk materials [9]. The drawbacks of neutrons are the difficulties of focusing the beam, and thereby resolving the individual grains, and the low flux, which makes neutrons less favorable for dynamic studies. With the development of synchrotrons, high-energy X-rays or hard X-rays ($E > 50$ keV) have become more and more available[10]. Hard X-rays have a high enough energy to penetrate several millimeters into a metallic sample, even several centimeters for lower atomic numbers, and the flux is orders of magnitude higher compared to neutrons.

The pioneering work by Hounsfield and Cormack in the late 1970s on X-ray computed tomography has had an enormous impact on the use of X-rays for non-destructive 3D characterization, not only in the medical community but also in materials science. Since then numerous reconstruction methods have been developed for solving the inverse problem posed by absorption contrast tomography (see e.g. [10]). In conventional X-ray computed tomography the reconstructions rely on the measured attenuation (absorption) of the X-ray beam, and thus enable three dimensional structural maps if there is a mass density variation in the specimen [11, 12]. In order to map specimens with a small differences in mass density, phase contrast tomgraphy[13, 14, 15] or holo-tomography can be used[16]. The resolution of these methods is dependent on the detector resolution but is typically around 0.5 micrometer. When it comes to information on grain structure (i.e. crystallographic information on grain orientations etc.) neither absorption contrast tomography or phase contrast tomography is capable of providing this information and alternative contrast mechanisms must be employed.

By serial sectioning and characterizing the surface of a specimen with optical microscopy [17] or SEM [18], it is possible to get three dimensional information of grain positions and with SEM/EBSD also grain orientations. This approach of course destroys the sample and prohibits dynamical studies of e.g. the effect of mechanical processing in a before-after scenario. To overcome this problem,

a number of non-destructive methods applying the principle of X-ray diffraction [19] have been developed.

The three dimensional X-ray diffraction (3DXRD) method described in [8] was the first method to utilize a combination of hard X-rays and micrometer focusing to study microstructures on a micrometer-scale. Illuminating the specimen with a monochromatic X-ray line-beam and recording the diffracted signal simultaneously on a near-field- and a far-field-detector during rotation makes it possible to get information about both the grain shape and the grain orientation.
A technique based on some of the same principles is diffraction contrast tomography (DCT [13, 14, 15]). In the case of DCT, the sample is illuminated with an extended (square) monochromatic beam similar to the one used in regular tomography. A detector is positioned so close to the sample that it records both the direct extinction image as well as the diffraction image from the sample during rotation. The DCT technique gives information on both grain shape and orientation of the individual grains.
The differential-aperture X-ray microscope (DAXM [20]) is a scanning technique which uses a point-shaped polychromatic microbeam in combination with wire scanning. Only a single detector is needed to get both information on grain shape as well as grain and subgrain orientations. X-ray diffraction computed tomography (XRD-CT, [21]) is a traditional point scanning technique using a small monochromatic pencil-beam to probe a sample and produce a multi-modal grain map of both physical and chemical features by recording several signals, such as diffraction, absorption and fluorescence.

Both 3DXRD, DCT, DAXM and XRD-CT rely on indexing routines, hence they find the result by computing "backwards" from the available data. The method of high energy X-ray diffraction microscopy (HEDM) presented in [22] uses an experimental setup similar to the one of the 3DXRD technique but computes the grain shapes and orientations by forward modeling and comparing with the available data.
Indexing routines can be fast, but the drawback is the vulnerability to noise in the data, such as spot overlap. A technique using forward modeling, such as HEDM , overcomes this problem but is computationally heavy and requires massive computer facilities such as clusters or GPUs.
Generally, the techniques mentioned above split into two categories: imaging and scanning techniques. The imaging techniques 3DXRD, DCT and HEDM all use the principle of diffraction to image the grain shapes on the detector. In order to obtain high enough resolution of the diffracted grain shape it is in all cases necessary to position the detector close to the sample. The techniques are relatively fast and in that sense well-suited for dynamical studies. But on the other hand, as the sample-to-detector distance may be as low as a few millimeters, there is not much room left for the equipment used in a dynamical study. A typical example would be coarsening or grain growth, where a furnace

is needed. Measuring continuously during heating would require the furnace to be very close to the detector and potentially damaging to the detector. Another example would be the use of stress rigs. Furthermore, detectors with a resolution higher than 0.5 micrometers do not exist today, hence the possible reconstruction resolution is limited to 0.5 micrometers.
The scanning techniques DAXM and XRD-CT base their shape reconstruction on the farfield signal and do not require a detector to be very close to the sample. The problem with scanning techniques is that they require a long time to map out big volumes. So even though it is possible to obtain a very high spatial resolution, say down to 100's of nanometers, it comes at the expense of time and thus makes the techniques unsuitable for dynamic studies.

Technique	Advantages	Drawbacks
Tomography, holo-tomography PCT	Fast acquisition	Limited by detector res., $0.5\mu m$ No orientation information
3DXRD	Fast acquisition Fast indexing	Reported resolution of $5\mu m$ Small sample-detector distance Limited by detector res., $0.5\mu m$ Indexing vulnerable to spot-overlap
DCT	Fast acquisition Fast indexing	Limited by detector res., $0.5\mu m$ Small sample-detector distance
HEDM	Fast acquisition Forward modelling not vulnerable to spot-overlap	Limited by detector res., $0.5\mu m$ Small sample-detector distance Reported resolution of $5\mu m$
DAXM	Resolution, $\sim 100nm$ Large sample-detector distance	Slow acquisition.
XRD-CT	High resolution, $\sim 100nm$ Large sample-detector distance Multimodal analysis	Slow acquisition.

Table 1.1: Advantages and drawbacks for grain maps formed by non-destructive techniques.

From the above literature study, it is clear that techniques that can produce high resolution grain maps of larger volumes for use in dynamical studies are still to be developed. The purpose of this PhD-project is to develop and implement a new non-destructive X-ray diffraction technique, the Boxscan technique, for mapping polycrystalline materials. The Boxscan technique positions itself between the imaging and the scanning techniques in the sense that it bases its spatial information on a scanning approach but uses extended linebeams which

are known from the imaging techniques. The orientation information is obtained from a standard farfield detector which makes room for experimental equipment. In short, the Boxscan technique, aims to provide the following features:

- Resolution is only dependent on the resolution of the stepping mechanics, and not limited to the detector resolution.
- The use of a standard farfield detector makes room for experimental equipment.
- The acquisition time is low enough to use the technique for certain types of dynamical studies.
- Large volumes can be mapped out.

The project involves theory and methods from several fields: X-ray physics, crystallography, metallurgy, mathematics and computer science. The intention with this project is not to study each of the fields in detail, but to apply enough knowledge from each of them to be able to develop and implement the Boxscan technique.

In the following chapters the Boxscan technique and it's application are described. In chapter 2 the basic theory of X-ray diffraction and crystals is introduced. Chapter 3 describes the details of the Boxscan technique with respect to theory and implementation issues. The technique is further more verified in this chapter. The possibility for extending the Boxscan technique to produce full volumetric 3D grain maps is studied in chapter 4 and finally in chapter 5 an application of the Boxscan technique to a large volume is reported.

Chapter 2

Diffraction from polycrystals

This chapter aims at giving the reader a fundamental understanding of the interaction between crystals and X-rays. This is needed to fully understand the principles of the Boxscan technique described in the following chapters. First a mathematical description of crystals is given followed by a description of how X-rays interact with crystals.

2.1 Crystals and crystal planes

2.1.1 Crystal lattices and unit cells

As stated before a crystal is a set of nodes, atoms, ions or molecules, arranged in a periodic lattice in three dimensions. Due to the periodicity of the lattice, it is only necessary to describe the subset of nodes which are repeated. This subset is called a unit cell and is mathematically described by three lattice vectors $\mathbf{a_1}, \mathbf{a_2}, \mathbf{a_3}$.

$$\mathbf{R_n} = u\mathbf{a_1} + v\mathbf{a_2} + w\mathbf{a_3} \tag{2.1}$$

where u, v, w are integers. Another way to describe the unit cell is by giving the sidelengths a, b, c and the corner angles α, β, γ, where $a = |\mathbf{a_1}|$, $b = |\mathbf{a_3}|$, $c = |\mathbf{a_3}|$, $\alpha = \angle(\mathbf{b}, \mathbf{c})$, $\beta = \angle(\mathbf{a}, \mathbf{c})$ and $\gamma = \angle(\mathbf{a}, \mathbf{b})$, see figure 2.1.

There exist 14 distinct configurations of the unit cell, called the 14 Bravias lattices, and each of these Bravais lattices belong to one of seven lattice systems. In crystallography, a crystallographic point group is the set of symmetry operations, which moves an infinite crystal into a new position where it looks exactly the same. In three dimensions it can be shown that there are 32 different point groups but not all of the 32 point groups apply to all 14 Bravais lattices. Point groups involve consistent groups of symmetry elements without translations. If translations are allowed, 230 space groups arise[23].

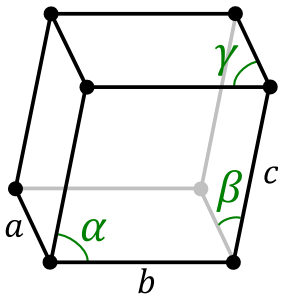

Figure 2.1: Definition of the unit cell by the parameters $(a, b, c, \alpha, \beta, \gamma)$

2.1.2 Crystal planes and Miller indices

Because of the periodicity of the lattice, it is possible to find sets of parallel and equidistant planes coinciding with crystal nodes of the same type. These are called crystal plane families and are described by so-called Miller indices (h, k, l). The commas are left out in the shorter form (hkl). The Miller index for a given plane family is defined as the planes parallel to the plane which intersects the axes $\mathbf{a_1}, \mathbf{a_2}, \mathbf{a_3}$ at $(|\mathbf{a_1}|/h, |\mathbf{a_2}|/k, |\mathbf{a_3}|/l)$. It is clear that two plane families, i.e. (110) and (220), can be parallel but still it is necessary to distinguish them since the interplanar distance d is different for the two plane families. The distance d is an important parameter in crystallography and will be treated further in the next section. For metals, the interplanar distances d are usually in the order of one Ångström. This distance is in the same order as the wavelength of X-rays. In fact, this was one of Laue's arguments when he did the first X-ray diffraction experiments in 1912 [24].

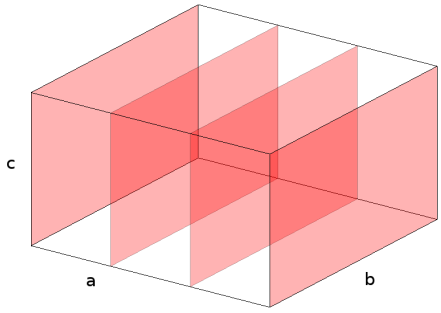

Figure 2.2: Plane family for Miller index $(hkl) = (100)$ for a cubic crystal.

2.1.3 Crystal orientation

As mentioned in the introduction, the orientation of the crystal lattice is what distinguishes one grain from another. Before we proceed it is therefore useful

to define and describe orientations mathematically [25]. As in any other system it is necessary to define a reference coordinate system. In this case, the reference coordinate system $(\epsilon_1, \epsilon_2, \epsilon_3)$ is spanned by the lattice vectors of a crystal fixed with respect to the sample, e.g. for a rolled sample natural choices are rolling, transverse and normal direction (RD, TD, ND). Similarly, the coordinate system $(\mathbf{s}_1, \mathbf{s}_2, \mathbf{s}_3)$ of a grain s is spanned by it's lattice vectors. The crystal orientation of the grain s is then defined as the set of rotations which brings the reference coordinate system $(\epsilon_1, \epsilon_2, \epsilon_3)$ to coincide with the grain coordinate system $(\mathbf{s}_1, \mathbf{s}_2, \mathbf{s}_3)$. In terms of algebra, the orientation can be represented by an orientation matrix g which fulfils:

$$\mathbf{s}_1 = \mathsf{g}\epsilon_1 \tag{2.2}$$

$$\mathbf{s}_2 = \mathsf{g}\epsilon_2 \tag{2.3}$$

$$\mathbf{s}_3 = \mathsf{g}\epsilon_3 \tag{2.4}$$

The orientation matrix g (sometimes the orientation is given by a matrix $\mathsf{U} = \mathsf{g}^{-1}$, see e.g. [8]) is a 3-by-3 rotation matrix with 9 coupled elements. Each crystal orientation is not necessarily uniquely described by the orientation matrix g and the reference coordinate system $(\epsilon_1, \epsilon_2, \epsilon_3)$. Take for example the case of a reference crystal with cubic symmetry, where the reference crystal could be fixed in 24 different ways to the sample. A way to overcome this problem is by choosing the orientation matrix closest to the identity matrix.
To fully describe an orientation in three dimensions only three independent parameters are needed, hence the orientation matrix g contains redundant information. One way to represent the orientation in only three parameters is by the use of Euler angles. The Euler angles $(\varphi_1, \phi, \varphi_2)$ describe the orientation as a sequence of rotations. A coordinate system $(\mathbf{e}_1, \mathbf{e}_2, \mathbf{e}_3)$ is first rotated φ_1 around the $\mathbf{e}_3$ axis , then ϕ around the new $\mathbf{e}_1'$ axis and finally φ_2 around the new $\mathbf{e}_3''$ axis. Since all three angles are 2π-periodic, the angles are usually restricted to the values $0 \leq \varphi_1 < 2\pi, 0 \leq \phi \leq \pi, 0 \leq \varphi_2 < 2\pi$. Yet this restriction does not reduce the Euler orientation space to a fundamental zone where each orientation only occurs once. For this to be fulfilled, it is necessary to limit the Euler orientation space even further but it is out of the scope to discuss this in this thesis. In practice Euler angles are widely used, especially when orientation needs to be represented by color, even though some of the mathematical properties of the Euler angles are less elegant compared to other representations.
Another way to describe orientation in three parameters is the Rodrigues parametrization. The Rodrigues parametrization uses the fact that any rotation can be described by a rotation angle ϕ around an axis $\mathbf{n}$. The Rodrigues vector $\mathbf{r}$ is defined as:

$$\mathbf{r} = \tan(\phi/2)\mathbf{n}, \quad \phi \in [0, \pi] \tag{2.5}$$

The Rodrigues representation has a number of properties making it an elegant way of representing orientation. The most useful property in this context is that rotations around a fixed axis and a free rotation angle maps to a line in Rodrigues space [26]. For two vectors $\mathbf{h}$ and $\mathbf{y} = \mathsf{g}^{-1}\mathbf{h}$ ($\mathbf{y}$ is a rotated version

of **h**), it can be shown that they map to the line:

$$\mathbf{r} = \mathbf{r}^0 + t\frac{\mathbf{h}+\mathbf{y}}{1+\mathbf{h}\cdot\mathbf{y}}, \quad -\infty < t < \infty \tag{2.6}$$

in Rodrigues space, where:

$$\mathbf{r}^0 = \frac{\mathbf{h}\times\mathbf{y}}{1+\mathbf{h}\cdot\mathbf{y}} = \tan(\phi_0/2)\mathbf{n}. \tag{2.7}$$

$\mathbf{r}^0$ is the rotation from **h** into **y**, hence the orientation matrix **g** can be computed from it:

$$\mathsf{g}_{ij} = \frac{1}{1+r_k r_k}((1-r_k r_k)\delta_{ij} + 2r_i r_j - 2\epsilon_{ijk}) \tag{2.8}$$

where ϵ_{ijk} is the permutation tensor.
A useful property of the Rodrigues representation is that it limits the orientation space to a so called fundamental zone[27, 28]. Different crystal systems have different fundamental zones, but they are all convex and can be constructed from a number of planes.
The three ways of representing orientation as described above are only a few. It is e.g. also possible to use quaternions [29] or exponential maps [30]. They all have different advantages and drawbacks for different applications so the choice of orientation representation is highly dependent on the context where it is used.

2.2 X-rays and crystals

2.2.1 X-ray sources

X-rays are electromagnetic waves with a wavelength λ between 0.1Å and 100Å. X-rays are the radiation that is emitted from an electron when it is de-accelerated. Traditionally X-rays are produced in X-ray tubes by accelerating electrons over an electric field and letting them collide with a metal anode, e.g. copper or tungsten. The collision can bring some electrons to a higher energy state causing fluorescent radiation when the electrons fall back into their ground state. Depending on the anode material, the fluorescent radiation can be in the energy range of X-rays. In addition, all electrons de-accelerated in the anode will emit radiation, *bremsstrahlung* radiation, but where the fluorescent radiation only emits at a number of specific energies, the *bremsstrahlung* radiation emits in a broad spectrum of energy.
It is difficult to get a high intensity of X-ray radiation using X-ray tubes, thus for experiments where a high intensity is necessary, one must go to one of the synchrotrons built in the last few decades. A synchrotron is a large storage ring for electrons where the electrons circle around and are kept at near light speed. The X-rays are produced in two ways: by bending magnets and by insertion devices. In fact, a synchrotron is not circular, it is a number of straight sections arranged in a polygon. In each corner of the polygon a powerful magnet bends the electrons into a new direction, causing the electrons to de-accelerate and

emit X-rays. At the straight sections insertion devices in terms of undulators and wigglers are used. Common to both of these are that they consist of sets of magnets which force the electrons to oscillate in the horizontal plane and thus produce X-rays[24]. The use of synchrotrons in experiments is much more convenient compared to X-ray tubes since it is possible to tune the energy of the X-rays and to get a high flux. Especially in experiments involving metals with a high Z, a high energy and flux is necessary to get a sufficient penetrative effect.

2.2.2 X-ray scattering

Before describing the interaction between X-rays and crystals it is necessary to understand how X-rays scatter from a single atom. As stated above, X-rays are electromagnetic waves (or photons), hence they interact with electrons of the atom. When an incoming X-ray wave with direction of propagation $\mathbf{k}$ is scattered from the electron cloud around the atom, the outgoing direction of propagation is $\mathbf{k}'$, see figure 2.3. Assuming elastic scattering such that the angle of incidence is equal to the scattering angle θ, then $|\mathbf{k}| = |\mathbf{k}'| = 2\pi/\lambda$, where λ is the wavelength of the X-ray wave. For two scattering events, one at the origin and one at position $\mathbf{r}$, with the same incoming direction of propagation $\mathbf{k}$, the phase difference will be $\Delta\phi(\mathbf{r}) = (\mathbf{k} - \mathbf{k}') \cdot \mathbf{r} = \mathbf{Q} \cdot \mathbf{r}$, where $\mathbf{Q}$ is called the wavevector transfer. From figure 2.3 it is readily seen that

$$|\mathbf{Q}| = 2|\mathbf{k}| \sin\theta = (4\pi/\lambda) \sin\theta. \tag{2.9}$$

The electron cloud of the atom is described by a distribution $\rho(\mathbf{r})$, hence to

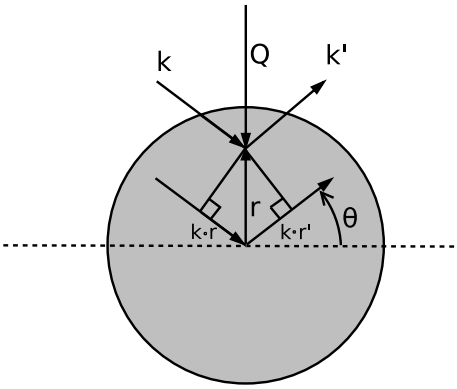

Figure 2.3: X-ray photon elastically scattered from an atom.

calculate the scattering from the whole atom it is necessary to integrate up all the infinitesimal scattering contributions over the electron distribution $\rho(\mathbf{r})$. Since X-rays are electromagnetic waves we must include the phase difference

$\Delta\phi(\mathbf{r})$ which reduces the total scattering to a simple Fourier transform:

$$f(\mathbf{Q}) = \int \rho(\mathbf{r}) e^{i\Delta\phi(\mathbf{r})} d\mathbf{r} = \int \rho(\mathbf{r}) e^{i\mathbf{Q}\cdot\mathbf{r}} d\mathbf{r}. \tag{2.10}$$

The atomic form factor, $f(\mathbf{Q})$, is calculated from the electron distribution of the atom so it is dependent on the atomic number Z. Near an absorption edge, dispersion corrections f' and f'' must be added to the expression for f, but it is out of the scope to introduce them here so we refer to [24] for a thorough description.
With the atomic form factor at hand it is now useful to consider a unit cell containing j atoms positioned at $\mathbf{r}_j$. Where the atomic form factor was an integral due to the continuous nature of the electron distribution, the unit cell structure factor is simply the discrete sum over the j atomic form factors f_j corrected by the phase differences:

$$F^{u.c.}(\mathbf{Q}) = \sum_{\mathbf{r}_j} f_j(\mathbf{Q}) e^{i\mathbf{Q}\cdot\mathbf{r}_j} \tag{2.11}$$

The next natural step is to consider a whole crystal made up of many unit cells. Each atom position in the crystal can be expressed as the center position of the unit cell added to the position of the atom in the unit cell, i.e. $\mathbf{R_n} + \mathbf{r}_j$. Again we sum over the number of atoms and correct by the phase difference. Since the exponential is seperable for additions, we can split the scattering from a crystal into the product of two sums where one is recognized as $F^{u.c.}(\mathbf{Q})$:

$$F^{crystal}(\mathbf{Q}) = \sum_{\mathbf{r}_j} f_j(\mathbf{Q}) e^{i\mathbf{Q}\cdot\mathbf{r}_j} \sum_{\mathbf{R_n}} e^{i\mathbf{Q}\cdot\mathbf{R_n}} = F^{u.c.}(\mathbf{Q}) \sum_{\mathbf{R_n}} e^{i\mathbf{Q}\cdot\mathbf{R_n}} \tag{2.12}$$

2.2.3 Reciprocal space

The latter sum in equation (2.12) is interesting in the sense that the complex sum of the phases will even out to unity except when:

$$\mathbf{Q}\cdot\mathbf{R_n} = 2\pi n, \qquad n \in \mathbb{Z}. \tag{2.13}$$

To find a vector which fulfills the above equation, we introduce the reciprocal lattice basis. Recalling the crystal lattice in equation (2.1), the reciprocal lattice basis $(\mathbf{a_1^*}, \mathbf{a_2^*}, \mathbf{a_3^*})$ is given by:

$$\begin{aligned} \mathbf{a_1^*} &= 2\pi \frac{\mathbf{a_2}\times\mathbf{a_3}}{\mathbf{a_1}\cdot(\mathbf{a_2}\times\mathbf{a_3})} \\ \mathbf{a_2^*} &= 2\pi \frac{\mathbf{a_3}\times\mathbf{a_1}}{\mathbf{a_1}\cdot(\mathbf{a_2}\times\mathbf{a_3})} \\ \mathbf{a_3^*} &= 2\pi \frac{\mathbf{a_1}\times\mathbf{a_2}}{\mathbf{a_1}\cdot(\mathbf{a_2}\times\mathbf{a_3})}. \end{aligned} \tag{2.14}$$

It is worth noticing the relationship between the direct and reciprocal space lattice:

$$\mathbf{a_i}\cdot\mathbf{a_j^*} = \begin{cases} 2\pi & , i = j \\ 0 & , i \neq j \end{cases} \tag{2.15}$$

A vector $\mathbf{G}$ expressed in terms of the reciprocal lattice basis:

$$\mathbf{G} = h\mathbf{a_1^*} + k\mathbf{a_2^*} + l\mathbf{a_3^*}, \qquad h, k, l \in \mathbb{Z}. \tag{2.16}$$

is inserted in to equation (2.13):

$$\mathbf{G} \cdot \mathbf{R_n} = 2\pi(hu + kv + lw) \in \mathbb{Z}. \tag{2.17}$$

The requirement $\mathbf{Q} = \mathbf{G}$ is called the Laue condition. In fact, the triplet (h, k, l) given in equation (2.16) is the Miller index for the plane family (hkl) and the vector $\mathbf{G}$ is perpendicular to the planes. A normal vector to the planes is then $\mathbf{n} = \mathbf{G}/|\mathbf{G}|$. The interplanar distance d is then the scalar product of $\mathbf{n}$ and a vector describing a point in the plane with respect to the origin, e.g. $\mathbf{a}_1/h$:

$$d = \frac{\mathbf{a}_1}{h} \cdot \mathbf{n} = \frac{\mathbf{a}_1}{h} \cdot \frac{\mathbf{G}}{|\mathbf{G}|} = \frac{2\pi}{|\mathbf{G}|} \tag{2.18}$$

Applying the Laue condition and the previously mentioned expression for $|\mathbf{Q}|$ (eq. (2.9)) we see that:

$$d = \frac{2\pi}{|\mathbf{G}|} = \frac{2\pi}{|\mathbf{Q}|} = \frac{2\pi}{(4\pi/\lambda)\sin\theta} = \frac{\lambda}{2\sin\theta} \Leftrightarrow \lambda = 2d\sin\theta \tag{2.19}$$

Equation (2.19) is called Bragg's Law or the Bragg condition and is a scalar version of the vectorized Laue condition. If the wavelength is known, it gives a way to compute the interplanar distance d from a scattering angle θ and vice versa.

2.3 Summary

In this chapter the theoretical background of unit cells, crystal planes and orientation, X-ray scattering, reciprocal space as well as the relation between them were described. The physical systems and the mathematical formulas were described and the chapter eventually stated Bragg's Law which is fundamental within the field of crystallography. The physics and the mathematics presented in this chapter are needed to understand the content of the following chapter and form the basis of the computations which are needed to perform the analysis of a Boxscan experiment.

Chapter 3

Boxscan Technique

As described in the introduction, several techniques already exist today for performing non-destructive characterization of polycrystals using X-rays. In this chapter, the theoretical principles and implementation of the Boxscan technique are presented. The development of the Boxscan technique has been the main focus of this PhD-project.
This chapter covers the principles of the Boxscan technique from both a theoretical and practical perspective. First, sections 3.1 and 3.2 cover the details of the experimental setup and the scanning procedure applied in the Boxscan technique. Next, the theoretical principle of indexing the data from a Boxscan experiment is provided in section 3.3. Finally, the software implementation of the technique is given in section 3.4.

3.1 Experimental setup

The experimental setup of the Boxscan technique is similar to the one of the 3DXRD. The primary goal is to have a setup which rotates and translates a sample during illumination by a well-defined X-ray beam. The setup is typically located inside an experimental hutch to shield the experimentalist from the X-rays. The experimental setup, as it is sketched in figure 3.1, consists of several parts: slits defining the incoming X-ray beam, a rotation stage, translation stages and a detector. Additionally, the setup can also contain other equipment used in the experiment. The properties of the individual parts are listed below.

3.1.1 X-ray beam and slits

The X-rays of the incoming beam have, for the types of experiments studied in this PhD-project, an energy above 50 keV. This class of X-rays are usually denoted as hard X-rays and are generated in synchrotrons as described in section 2.2. Before the X-rays enter the experimental hutch, they have been focused in

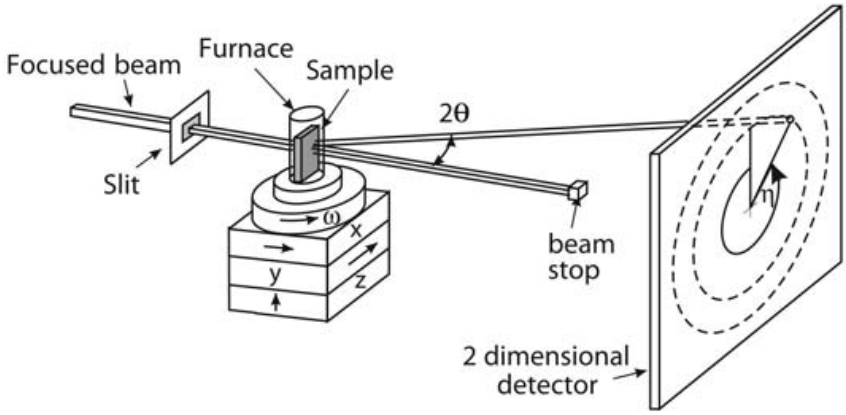

Figure 3.1: Experimental setup of the Boxscan technique.

the vertical direction by a number of optical lenses. The beam is monochromatic and with a flux high enough not to be a bottleneck for the data acquisition. Typical exposure times are 0.25 to 1 second.
The cross-sectional dimensions of the beam is defined by two sets of slits, a vertical set and a horizontal set.

3.1.2 Rotation stage ω

To be able to bring the grains in the sample into a position where the diffraction condition is fulfilled, a rotation stage is needed. The rotation angle is denoted ω so rotation stage and ω-stage are used interchangeably here. The rotation stage is often located as the top stage just below the sample, but any position is of course possible, though it may change the geometry of the setup. The axis of rotation is parallel to the z-axis described below. The angular resolution is as low as 0.01 degrees but such a high resolution is rarely needed.

3.1.3 Translation stages x, y, z

To move the sample to a given position in the beam, a number of translation stages are needed. Each translation stage moves in one direction only, so to be able to move in three directions, three stages are needed, but since movements along the beam direction x is irrelevant for the Boxscan type of experiment, the x-translation is not needed. Typically, a translation stage has a resolution down to 0.5 micrometers but adding e.g. piezo translations to the setup, finer stepping is possible. With today's equipment, resolutions down to 10 nanometers are not rare. The precision of the translations are dependent on the load placed on top of the stages, hence a lower resolution must be expected in experiments where heavy additional equipment are placed on top of the translation stages.

3.1.4 Detector

To measure the diffracted signal a detector is positioned such that the scattering angles 2θ of interest fit inside the detector's area. In a diffraction experiment, the diffracted signal will spread out in cones (Debye-Scherrer cones) and thus show as rings with a unique 2θ on a plane detector. The sample-to-detector distance depends on several parameters such as the material and the beam energy, but for this type of experiment the distance is typically more than 40 centimeters. When an X-ray photon is diffracted from the sample and hits the detector it is converted to visible light by a scintillator. The photon can now be measured by a light sensor such as a CCD. A typical size of the detector is 2048-by-2048 pixels with a pixel size in the order of 50-200 micrometers. Each pixel measures the integrated intensity in a small time interval and outputs it to an array for reading.
The direct X-ray beam has too high intensity for the detector, so to block out the direct beam, a small beam stop is placed between the sample and the detector without interfering with the diffracted signal.
The positions on the detector are described in a polar coordinate system given by the azimuthal angle η and the scattering angle 2θ. The choice of a polar coordinate system is due to the fact that diffraction spots lie on rings. The η-angle is defined to be zero at 12 o'clock and is positive in the clockwise direction, see figure 3.1. The radii of the rings on the detector are dependent on the sample-to-detector distance, hence this distance must be known before hand or computed. If the detector is not perfectly perpendicular to the x-axis (incoming X-ray beam), the detector measurements will be affected by the tilt. The sample-detector distance and the tilt can be computed by measuring the powder diffraction signal from a known sample and eventually be applied to the detector measurements.

3.1.5 Additional equipment

Some experiments require additional equipment such as a stress-rig or a furnace. If they are to be applied in-situ the equipment must be in the experimental setup. This is one of the big advantages of the Boxscan techniques as the sample-to-detector distance is more than 40 centimeters for this setup, which leaves room for including either a furnace or a stress-rig.

3.1.6 Coordinate system of the laboratory

To get a fixed reference coordinate system, a laboratory coordinate system is defined. The x-axis is defined to point in the direction of the X-ray beam, the z-axis is pointing upwards and to get a right-handed system the y-axis is the cross product between z and x, $y = z \times y$. The directions are sketched in figure 3.2. The default rotation direction of the ω-stage is right-hand positive with respect to the laboratory coordinate system.
For further analysis it is useful to introduce a sample coordinate system (x_s, y_s, z_s)

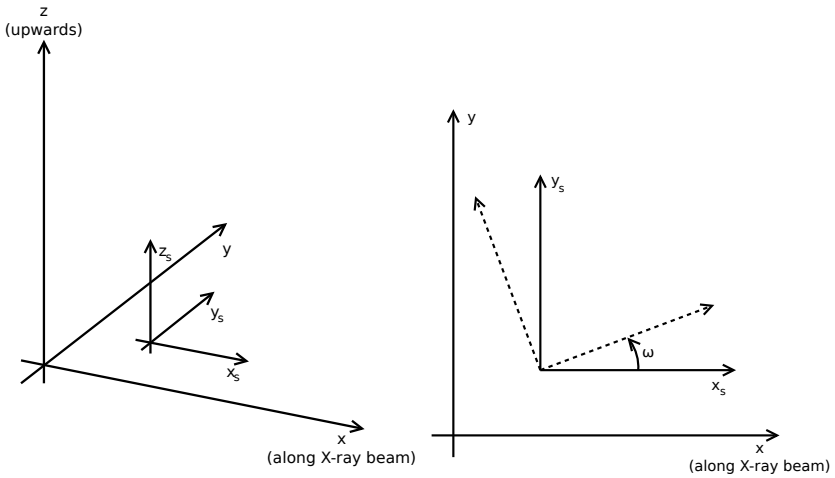

Figure 3.2: Left: Laboratory coordinate system (x, y, z) and sample coordinate system (x_s, y_s, z_s) for $\omega = 0$. Right: (x, y)-plane of the laboratory coordinate system and (x_s, y_s)-plane of the sample coordinate system. The sample coordinate system is shown for a zero ω-rotation (solid) and an arbitrary ω-rotation (dashed).

which is rigidly mounted with respect to the sample, i.e. it rotates with the ω-angle and the z_s-axis coincide with rotation axis of the ω-rotation, i.e the z_s-axis and the z-axis are parallel.
Mathematically, the relation between (x_s, y_s, z_s) and (x, y, z) is:

$$\begin{pmatrix} x \\ y \\ z \end{pmatrix} = \begin{pmatrix} \cos(\omega) & -\sin(\omega) & 0 \\ \sin(\omega) & \cos(\omega) & 0 \\ 0 & 0 & 1 \end{pmatrix} \begin{pmatrix} x_s \\ y_s \\ z_s \end{pmatrix} + \begin{pmatrix} x_0 \\ y_0 \\ z_0 \end{pmatrix} \tag{3.1}$$

where $(x_0, y_0, z_0)^T$ is the position of the origin of the sample coordinate system with respect to the laboratory coordinate system.

3.2 Scanning procedure

As mentioned in the introduction one of the key elements of the Boxscan technique is the scanning procedure which differs significantly from traditional point scanning techniques. Where traditional point scanning uses a small pencil-beam, the Boxscan technique uses a much larger box-shaped beam which speeds up the data acquisition.
The first step in characterizing a polycrystal with the Boxscan technique is to perform the experimental work. After the experimental equipment and the sample is in place, the volume to be characterized in the sample should be specified.

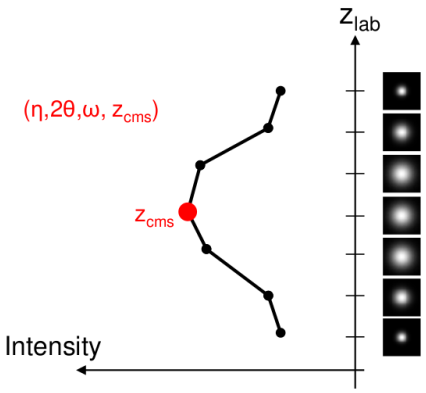

Figure 3.3: Boxscan z-profile: The intensity of the diffraction spot varies with the volume of the illuminated sub-volume of the grain.

From this volume, the vertical and the horizontal limits of the Boxscans two-part scanning procedure are determined. The two scanning parts are denoted the vertical and the horizontal scan and are described in the following.

3.2.1 Vertical scan

For the vertical scan, the beam is box-shaped (hence the name Boxscan) with a high width-height aspect ratio, i.e. the beam is very wide in the horizontal y-direction and limited vertically in the z-direction to a few tens of micrometers or less.
For a given position of the z-translation stage, the sample is rotated in an ω-interval $[\omega_1, \omega_a]$ in steps of $\Delta\omega$. At each ω-position, a detector image is acquired before proceeding to the next ω-position. When the whole ω-interval has been scanned for the given z-position, the sample is translated by Δz to the next z-position where the sample again is rotated in ω during image acquisition. This is repeated for each z-position until the end of the z-interval has been reached. Since the sample is scanned along the z-axis, this scan is also referred to as the z-scan.
When a sub-volume of a grain is illuminated by the X-ray beam and the grain fulfils the diffraction conditions for the given ω-rotation, a diffraction spot can be measured on the detector at $(2\theta, \eta)$. If a specific diffraction spot is traced as the sample is translated though the beam, the intensity of the diffraction spot will vary with the volume of the illuminated grain sub-volume, see figure 3.3. In the Boxscan terminology this is referred to as a profile along the z-direction or a z-profile. From a theoretical point-of-view and for a infinitely small step size Δz and infinitely small beam-height, a profile would be the double integral of the grain volume over the planes perpendicular to the scanning direction. In a

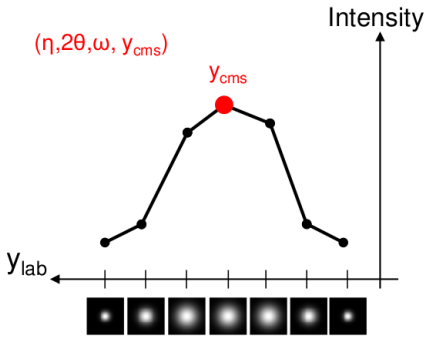

Figure 3.4: Boxscan y-profile: The intensity of the diffraction spot varies with the volume of the illuminated sub-volume of the grain.

situation of measurement, it is not possible to make the beam height or the step size Δz infinitely small, hence the measured profile is convoluted with the beam-profile and sampled in steps of Δz. The beam-profile should not be confused with a Boxscan profile, as it is a measurement of the intensity variations of the beam in a given direction. Ideally, the beam-profile for a boxbeam is a square-profile, but in practice it is more similar to a square-profile convoluted with a Gaussian.

3.2.2 Horizontal scan

For the horizontal scan, the beam is dimensioned such that it is box-shaped with a high height-width aspect ratio. A way to think of it, is to imagine it as the beam from the vertical scan rotated 90 degrees around the x-axis. The data acquisition procedure is similar to the one before: For a given position of the y-translation stage, the sample is rotated in an ω-interval $[\omega_1, \omega_a]$ in steps of $\Delta\omega$. The sample is translated Δy to the next y-position and the acquisition procedure is repeated until the whole y-interval has been scanned.
As with the vertical scan, a diffracting grain in the horizontal scan will generate a profile, i.e. a y-profile. Like a z-profile, a y-profile will contain information about the double integral of the rotated grain volume, but in this case the double integrals are evaluated along the planes perpendicular to the y-axis, see figure 3.4, and the sampling step is Δy.

3.2.3 Boxscan scan versus point scan technique

In many ways, the Boxscan technique is similar to a point scan technique, but one significant difference is the amount of images (hence time) needed to be acquired to cover a given sample volume. Assume that N_z vertical steps and N_y horizontal steps are required to get the wanted resolution, then the amount of images needed to be acquired with the point scan technique would scale with

$N_y N_z$ where the Boxscan would scale with $N_y + N_z$, i.e. a reduction from $N(n^2)$ to $N(n)$.

3.3 Indexing in 6 dimensional space

To be able to understand the indexing routine of the Boxscan technique, it is useful to study the 6 dimensional space in which the center of mass (CMS) and orientation of a grain can be described. As mentioned previously, a grain has an orientation which can be parametrized by a three element Rodrigues vector, see chapter 2, and the CMS of the grain of course exists in real 3 dimensional space. The sample coordinate system (x_s, y_s, z_s) is useful for expressing the position of the CMS of the grain since the sample is fixed in this coordinate system. Thus, a grain exists as a point in the 3 dimensional real space as well as in the 3 dimensional Rodrigues space, enabling a full description of the CMS position and orientation by a 6 dimensional point in $(x_s, y_s, z_s, r_1, r_2, r_3)$.
In the following, it is assumed that the space group of the unit cell is known. Knowing a few properties of the material, this information can usually be looked up in the *International Tables for Crystallography* (`http://it.iucr.org/`). Furthermore, for the indexing to work, it is assumed that the ω-interval is chosen such that it is possible to measure several diffraction spots in the dataset for each grain. The object of the following sections is to explain how to come from y- and z-profiles to indexed grains in 6 dimensions.

3.3.1 Profile information

The profiles described above, no matter if it is y- or z-profiles, contain information of both the orientation and CMS position.

3.3.1.1 Orientation information

Each profile is measured at a position $(2\theta, \eta)$ on the detector for a given ω-rotation. This diffraction spot at $(\omega, 2\theta, \eta)$ corresponds to a specific diffraction event for a (hkl). The relation between the position of the diffraction spot and the (hkl) is via the orientation of the grain. Extending the diffraction theory described in chapter 2 further, it is possible to show that:

$$\Omega \mathsf{g}^{-1} \mathbf{h} = \cos(\theta) \begin{pmatrix} -\tan\theta \\ -\sin\eta \\ \cos\eta \end{pmatrix} \tag{3.2}$$

where g^{-1} is the inverse of the orientation matrix defined previously, Ω is the sample coordinate system's rotation with respect to the laboratory coordinate system in terms of a rotation matrix:

$$\Omega = \begin{pmatrix} \cos(\omega) & -\sin(\omega) & 0 \\ \sin(\omega) & \cos(\omega) & 0 \\ 0 & 0 & 1 \end{pmatrix}, \tag{3.3}$$

and the theoretical scattering direction $\mathbf{h}$ in the coordinate system of the grain is defined as:

$$\mathbf{h} = \begin{pmatrix} h_1 \\ h_2 \\ h_3 \end{pmatrix} = \frac{\lambda}{4\pi \sin(\theta)} \mathsf{B} \begin{pmatrix} h \\ k \\ l \end{pmatrix}. \tag{3.4}$$

The matrix B is a transformation matrix which changes the basis of the calculations from a crystallographic reciprocal coordinate system to an orthogonal Cartesian coordinate system, see [8, 23] for details.
By rearranging the expression in equation (3.2) to:

$$\Omega^{-1} \cos(\theta) \begin{pmatrix} -\tan\theta \\ -\sin\eta \\ \cos\eta \end{pmatrix} = \mathsf{g}^{-1}\mathbf{h}. \tag{3.5}$$

it can be seen that this is just an expression for a rotation around a fixed axis. As it was stated in subsection 2.1.3, this maps to a line in Rodrigues space. In other words, if the (hkl) is known for a $(\omega, 2\theta, \eta)$-measurement, it is possible to confine the possible grain orientation to be on a line in Rodrigues space.

3.3.1.2 Center of mass information

As described previously, the profiles along the scanning axis are double integrals of the rotated grain volume. The integral is a linear operator, so the rotated grain's CMS position projected onto the scanning axis can be found as the intensity weighted average of the profile, see figure 3.5. Or to put it more mathematically, given a profile measured for a given rotation ω_p at n positions, $t_1 \dots t_n$, at a scanning axis t with a measured diffraction spot intensity of $I_1 \dots I_n$, the grain's projected CMS position is computed as:

$$\mu_t(\omega_p) = \frac{\sum_{i=1}^{n} t_i I_i}{\sum_{i=1}^{n} I_i} \tag{3.6}$$

Geometrically this means that it is possible to confine the rotated grain's CMS position to the plane which is perpendicular to the scanning axis and intersects the scanning axis at $\mu_t(\omega_p)$.

3.3.2 Grain indexing in 6 dimensions

With the information available from the y- and z-profiles, the purpose is now to index grains, i.e. to determine grain orientations. The indexing is done in several steps which all are explained below.

3.3.2.1 Profile matching

If the same sample volume was scanned in both the vertical and the horizontal scans, it is expected that a grain with a y-profile for given $(\omega, 2\theta, \eta)$ also has a z-profile for the same $(\omega, 2\theta, \eta)$ and vice versa. Thus, finding y- and z-profiles

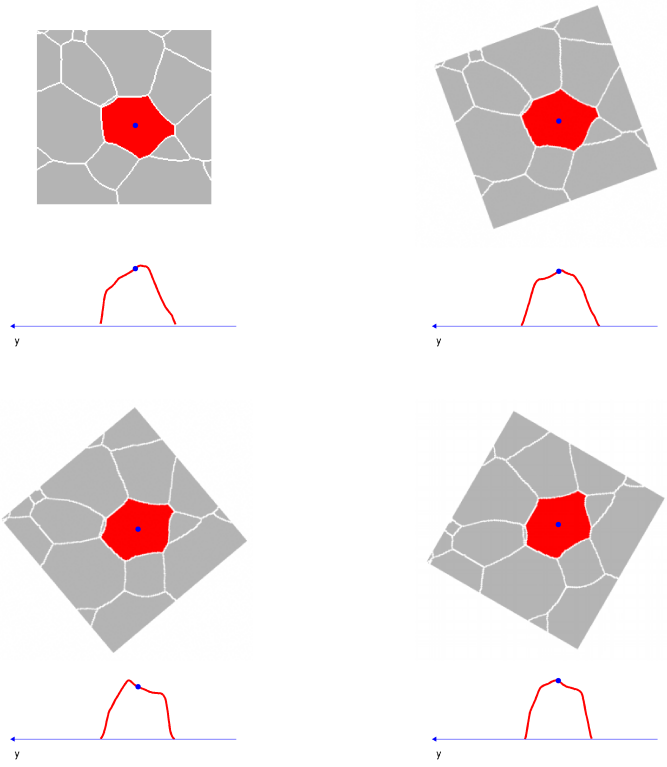

Figure 3.5: Profiles for the same grain at different ω-values.

from the same grain can be done by searching for profiles which have similar $(\omega, 2\theta, \eta)$-values within some tolerances $\delta_\omega, \delta_{2\theta}$ and δ_η. A match found, denoted by M_i, has five values connected to it $(\mu_y(\omega), \mu_z(\omega), \omega, 2\theta, \eta)$.
As stated above, $\mu_y(\omega)$ and $\mu_z(\omega)$ each confine the rotated grain's CMS position to a plane perpendicular to the scanning direction, i.e. an xz-plane and a xy-plane, respectively. Knowing both it is possible to confine the CMS position further as the intersection of a xz-plane and a xy-plane is a line in 3 dimensions parallel to the x-axis of the laboratory coordinate system. As the rotation angle ω is known and the relation between the laboratory and sample coordinate system is established in equation (3.1) the line parallel to the $x_s y_s$-plane in (x_s, y_s, z_s) can be found. Inputting $\mu_y(\omega)$ and $\mu_z(\omega)$ directly into (3.1), it is readily seen that the line must fulfill:

$$\mu_y(\omega) = y_s \cos(\omega) + x_s \sin(\omega) + y_0 \tag{3.7}$$

$$\mu_z(\omega) = z_s + z_0 \tag{3.8}$$

As shown in 2.1.3, the three angles $(\omega, 2\theta, \eta)$ map to a line in Rodrigues space for a known (hkl). The (hkl)-value for a given $(\omega, 2\theta, \eta)$ is not known beforehand, and it is only possible to limit the set of (hkl)-values to the ones belonging to the given 2θ-value. Thus, inputting each possible (hkl)-value into equation (3.5) with the values $(\omega, 2\theta, \eta)$ gives a number of lines in Rodrigues space, where one of them passes through the grains orientation g.

3.3.2.2 Indexing of subinterval

As the rotation axis of ω is parallel to the z-axis, the grain's CMS positions in z are not affected by the rotation. This means that all matches M for a given grain are expected to have the same $\mu_z(\omega)$ within some limits determined by the stability of the experimental equipment. A subset M_S where $\mu_z(\omega)$ is within a small interval $z_S \pm \delta_z$ is taken out. Two matches M_a and M_b with $\mu_z(\omega_a) = \mu_z(\omega_b)$ (e.g. if they are from the same grain, see figure 3.6) can be written into a linear system of equations according to equation (3.7):

$$\begin{bmatrix} \mu_y(\omega_a) - y_0 \\ \mu_y(\omega_b) - y_0 \end{bmatrix} = \begin{bmatrix} \cos(\omega_a) & \sin(\omega_a) \\ \cos(\omega_b) & \sin(\omega_b) \end{bmatrix} \begin{bmatrix} y_{ab} \\ x_{ab} \end{bmatrix} \tag{3.9}$$

Thus, their intersection point will be:

$$\begin{bmatrix} y_{ab} \\ x_{ab} \\ z_{ab} \end{bmatrix} = \begin{bmatrix} \begin{bmatrix} \cos(\omega_a) & \sin(\omega_a) \\ \cos(\omega_b) & \sin(\omega_b) \end{bmatrix}^{-1} \begin{bmatrix} \mu_y(\omega_a) - y_0 \\ \mu_y(\omega_b) - y_0 \end{bmatrix} \\ \mu_z(\omega_b) - z_0 \end{bmatrix} \tag{3.10}$$

This is of course only valid as long as the lines are not parallel, i.e. $\omega_a \neq \omega_b$.
For the diffraction angles $(\omega_a, 2\theta_a, \eta_a)$, the lines in Rodrigues space (equation (2.6)) are computed for the set of (hkl)-values belonging to the $2\theta_a$-value. Similarly, the lines in Rodrigues space are computed for the set of (hkl)-values

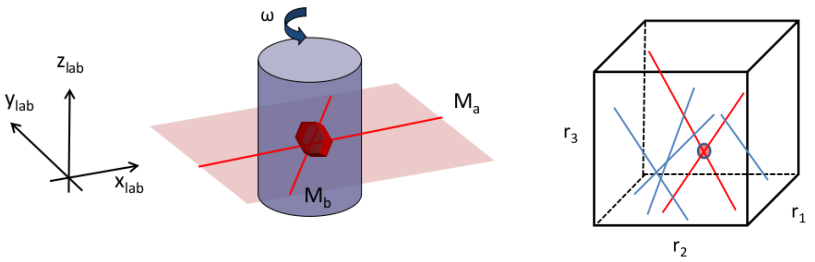

Figure 3.6: Left: Intersection in real space. Right: Intersection in Rodrigues space. Only the two lines computed for the correct hkl's will intersect.

belonging to the $2\theta_b$-value and $(\omega_b, 2\theta_b, \eta_b)$. Two of these lines, one from M_a and one from M_b, will intersect at a position $\mathbf{r}_{ab}$ inside the fundamental zone of the Rodrigues space, see figure 3.6. The other lines will not intersect each other. Hence, two matches that intersect will produce a point in 6D space.
The strategy of the indexing is to compute the 6D intersection point for all possible combinations of matches in M_s. When the intersection point between two matches is to be found, first (x_{ab}, y_{ab}, z_{ab}) is computed. If it is inside the scanned volume, the intersection point $\mathbf{r}_{ab}$ inside the fundamental zone in Rodrigues space is computed. These criteria are applied to filter out intersections between matches from different grains, yet some intersections may not be caught and thus enter as false positives.
All the intersections in 6D fulfilling the criteria are put into a a large dataset P_6 which will contain both the true information on the grains' positions as well as the false positives. The task is now to find the "needle in the haystack", i.e. getting rid of the false positives. To do so, it is noted that if p matches exist for a grain (i.e. the grain diffracts p times in the chosen ω-interval, $p \geq 2$ as it has been assumed), then $\frac{p(p-1)}{2}$ points for this grain will occur in P_6, i.e. the local point density around a true grain will be high. On the other hand, the false positives are assumed to be scattered uniformly in the 6D space and thus less likely to have a neighboring point close by.
To reveal the positions with a high point density, a k-nearest neighbor (knn) technique is applied [31]. The knn works by visiting every point in P_6 and counting how many neighbors this point has inside a small 6D ellipsoid. The semi-principal axes are aligned with the axes in the 6D system and are scaled with the expected noise-level of data along this axis.
Knowing the number of neighbors each point in P_6 has, possible grain candidates can be taken out from P_6 one by one. First, the point in P_6 with the highest number of neighbors is chosen. For this grain candidate, the theoretical matches M_t in the interval $[w_1 \dots w_a]$ are simulated, i.e. the angles $(\omega, 2\theta, \eta)$ and positions $\mu_y(\omega)$ are computed based on the geometry of the experimental setup. The fraction of theoretical matches which agree with a measured

match M is denoted the completeness. If the completeness is higher than some user set limit, the grain candidate is accepted as a grain. To refine the CMS position of the found grain, a Huber fitting routine [32]is used for fitting the measured $\mu_y(\omega)$ to equation (3.7). The matches which support the found grain are removed from P_6 and the point in P_6 which now has the highest number of neighbors is chosen as the next grain candidate. This procedure is repeated until no more grains can be found in P_6.
A new subset M_S is taken out, where the interval of interest is moved by the small amount δ_z compared to the previous one. The two intervals are chosen to overlap such that most matches from a grain at one point will be inside the same interval.

3.4 Implementation

Where the previous section described the principles of the Boxscan technique, this section explains the practical details of the implementation.
The Boxscan implementation was developed in Matlab with the use of a little Java coding. Java interfaces seamlessly with the Matlab environment and Java objects can be loaded directly into the Matlab workspace. Furthermore, a few external open source libraries written in C and Java were used. The advantages of using Matlab as development platform are the quick idea-to-code generation and the high number of toolboxes. The drawback is the execution speed as for most scripted languages.

3.4.1 Data storage and data type definitions

When the Boxscan technique is applied in experiments it produces a huge amount of images, i.e. 1000s or 10000s of images, each containing up to several hundred diffraction spots. To keep track of this huge amount of data a database is used. For smooth integration with Matlab, the Java database H2 was chosen (`www.h2database.com`). H2 is an open source SQL database engine with only a 1 MB footprint.
In the present implementation a set of data type definitions have been used. They are introduced below together with the table-name where they are stored in the database. A full layout of the database is shown in figure 3.7.

3.4.1.1 Rings and hkls

Dependent on the crystallography of the material studied in the experiment, the measured diffraction spots appear on a set of rings for a set of allowed hkls. Each allowed hkl is stored as an entry in the `hkl`-table and reference the ring entry in the `ring`-table which it belongs to. The `ring`-table stores the 2θ-value for the rings and the structure factor.

3.4.1.2 Images

Each image which is acquired has a number of parameters connected to it, e.g image-number, ω, values of the translation stages and the current of the storage ring at the time of acquisition. This information is stored in the `y_image`- and `z_image`-tables corresponding to the images from the horizontal and vertical scans, respectively. The images themselves are not stored in the tables, only the image parameters used in the further analysis.

3.4.1.3 Spots

The parameters of the individual diffraction spots in the images are stored in either `y_spots`- or `z_spots`-tables. The tables contain a reference to the ring and the image on which the spot is found in the `ring`- and `image`-tables as well as the η-value and the integrated intensity of the spot.

3.4.1.4 Reflections

The way the images are acquired by integrating the diffracted signal over a small interval in ω enables the possibility for the diffraction spot to be spread over several neighboring images in ω. A reflection is a collection of spots from neighboring images which are assumed to belong to the same diffraction event, i.e. their ω- and η-values are within some user-set limits. The tables `y_reflections` and `z_reflections` contain the intensity-averaged values of η and ω as well as the total intensity of each reflection, i.e the sum of all the spot intensities normalized by the structure (eq. (2.11)), polarization (eq. (3.18) after [33]) and Lorentz factors (eq. (3.17)).
The ring number and the translation stage position are repeated in `ringid` and `spt` to make the subsequent data processing easier. This is in fact a break of the database normalization rules, but it is done for practical purposes. The relation between the spots which contribute to a certain reflection is given in the tables `y_spot2refl` and `z_spot2refl`.

3.4.1.5 Profiles

A profile is a set of reflections observed at similar values in ω and η, and neighboring values in y or z. A more thorough description of the profile is found earlier in this chapter. As with the reflections, the ringid is repeated in the tables `y_profiles` and `z_profiles`. Again, the intensity-averaged values of η and ω as well as $\mu_y(\omega)$ or $\mu_z(\omega)$ are stored in the `y_profiles` or `z_profiles`. The summed intensity and the reflection of the profile with the highest intensity are also stored. The relation between the reflections which contribute to a certain profile is given in the tables `y_refl2profile` and `z_refl2profile`.

3.4.1.6 Matches

A match is a y-profile and a z-profile which have similar values of $\omega, 2\theta, \eta$. The table `match` contains the links between the y-profiles and the z-profiles which correspond.

3.4.1.7 Grains

The `grains`-table contains the 6D point $x_s, y_s, z_s, r_1, r_2, r_3$ for the grains found and their completeness factors. The matches which contribute to a given grain are given in the table `match2grain`.

3.4.1.8 Graphical layout of database

The tables and the relationships within the database are shown in the schematic layout of the database structure in figure 3.7.

3.4.2 Data processing

The data processing steps involved going from raw detector images to grains are explained below.

3.4.2.1 Initializations

The first step of the analysis is to setup all necessary variables and parameters in Matlab. A script `initboxscan.m` sets up the path and the javapath in Matlab. Furthermore, a Matlab structure variable containing all the parameters necessary for the Boxscan analysis to run, that is, the name of the database, crystal parameters, experimentally-measured parameters, tolerances $\delta_\omega, \delta_{2\theta}, \delta_\eta$, etc. are created. The most practical way to construct this variable is to have a Matlab `m`-file, e.g. `boxscan_prefs.m` in which all the parameters are hard coded into. This way, a human-readable form of all the parameters are also always at hand.

3.4.2.2 From images to spots

After the experimental data has been acquired, it is necessary to extract the information from the images and store it in the database. The first step is to determine the detector tilt and the sample-detector distance, also called the calibration. For this purpose, a powder diffraction image from a well-known sample must be obtained by either using a specific calibration powder or using the sample measurements directly. The powder diffraction image is input into the free software program Fit2D [34] along with the needed unit cell and detector parameters and the values for the tilt and the sample-detector distance are fitted. Next, each detector image is corrected for the detector's spatial distortion, the detector background image is subtracted and finally the image is caked, i.e. the images are re-sampled such that the coordinate system of the image is changed

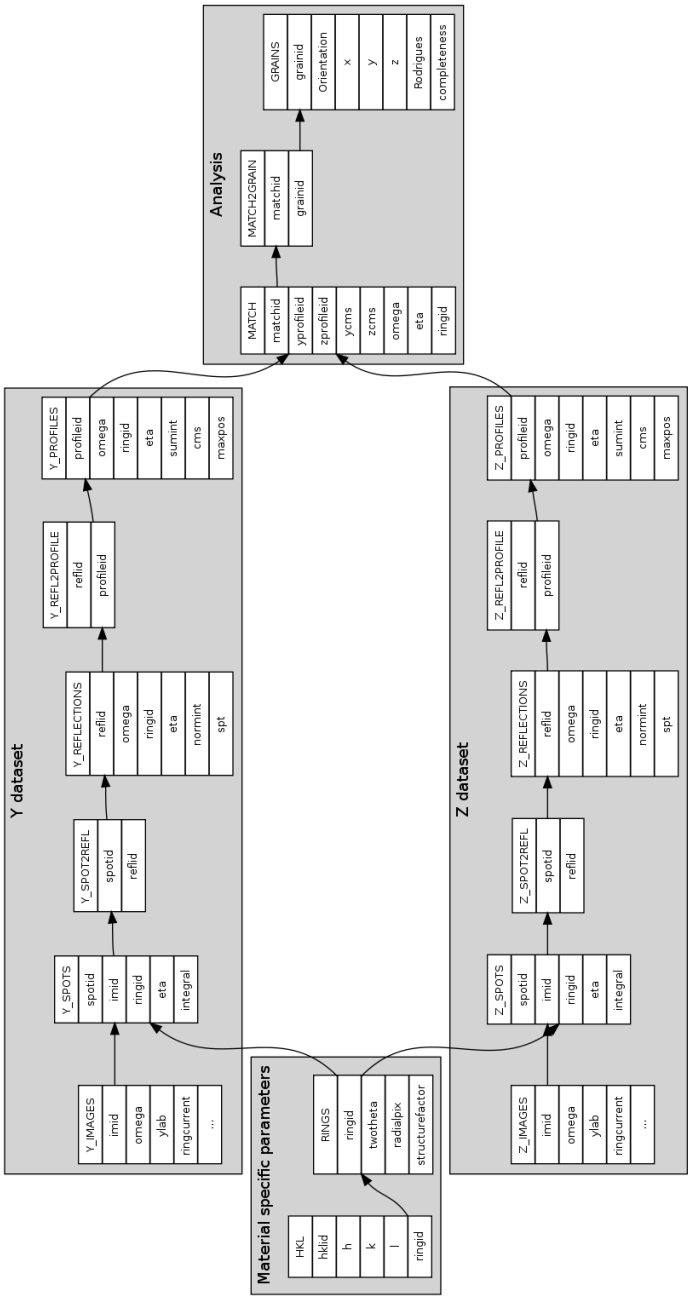

Figure 3.7: Schematic layout of the database structure.

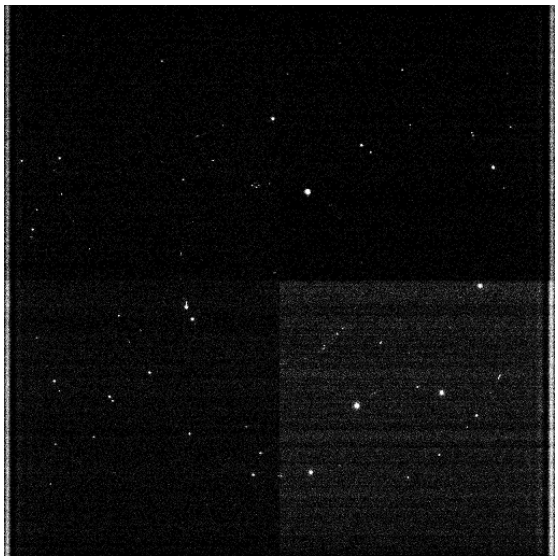

Figure 3.8: Detector image of a diffraction signal containing many diffraction spots.

from Cartesian to polar $(2\theta, \eta)$. This way the diffraction rings on the images (figure 3.8) are stretched into lines (figure 3.9) which are easier to handle in matrix-based computer software. The figures 3.8 and 3.9 also show the effect of the detector's point spreading in the sense that the individual diffraction spots are not restricted to a single pixel but a small neighborhood with radially decreasing intensity.
After caking, the image is loaded into Matlab. The ring corresponding to each 2θ-value is isolated and all pixels in an interval $2\theta \pm \delta_{2\theta}$ are summed along 2θ such that no intensity of the ring is left out. This results in the intensity as a function of the η-value, $I(\eta)$, for the given ring where the diffraction spots have been collapsed into 1D peaks, see figure 3.10. Using an automated fitting procedure the position and intensities of the individual diffraction spots are derived from $I(\eta)$. Each peak is assumed to have an intensity which follows a pseudo-Voigt Π [35]:

$$\Pi(\eta - \eta_i, \sigma_i, w_i) = w_i L(\eta - \eta_i, \sigma_i) + (1 - w_i) G(\eta - \eta_i, \sigma_i) \quad (3.11)$$

$$G(\eta - \eta_i, \sigma_i) = \exp(-\ln(2)(\frac{\eta - \eta_i}{\sigma_i})^2) \quad (3.12)$$

$$L(\eta - \eta_i, \sigma_i) = \frac{1}{1 + (\frac{\eta - \eta_i}{\sigma_i})^2} \quad (3.13)$$

where w_i is a weight in the interval $[0, 1]$, σ_i is a parameter adjusting the width of the pseudo-Voigt and η_i is the peak's midpoint. The Lorentzian L is heavy-tailed and has a relatively sharp peak where the Gaussian G has smaller tails

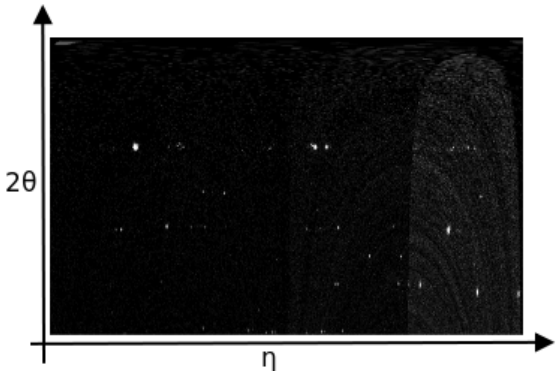

Figure 3.9: The detector image from figure 3.8 caked (polar transformed).

and has a more rounded peak enabling it to model many peak shapes only by varying their individual contributions by w_i. Since there are multiple peaks on a ring, see figure 3.10, multiple pseudo-Voigts are needed to model $I(\eta)$:

$$I_{model}(\eta) = \sum_{i=1}^{n} f_i \Pi(\eta - \eta_i, \sigma_i, w_i). \tag{3.14}$$

The parameter f_i is an intensity scaling parameter. To fit the model $I_{model}(\eta)$ to the measurement data $I(\eta)$, the Levenberg-Marquardt (LMA, [36]) algorithm is used. The LMA is an iterative numerical method often used for least squares curve fitting. In this case, the LMA should minimize the cost S:

$$S = \sum (I(\eta) - I_{model}(\eta))^2 \tag{3.15}$$

for the parameters $\eta_i, \sigma_i, w_i, f_i,\ i = 1 \ldots n$.
For the curve fitting, the *levmar* open source implementation (`http://www.ics.forth.gr/~lourakis/levmar/`) was used. This implementation is written in C/C++ and has an interface for Matlab. It provides the option of using constraints on the parameters, which is useful since some of the parameters only have an interval where they are valid or plausible, see table 3.1.
The LMA needs an initial guess of the parameters of each peak to get started. The parameters w_i and σ_i are all set to 0.5 and 0.25 degrees, respectively, in the initial guess. The absolute values of the derivatives $|\frac{\partial S}{\partial w_i}|$ and $|\frac{\partial S}{\partial \sigma_i}|$ are both small compared to $|\frac{\partial S}{\partial \eta_i}|$ and $|\frac{\partial S}{\partial f_i}|$ so focus is put on getting good estimates of η_i and f_i. In the measured data $I(\eta)$, points with a local maximum higher than some threshold I_{min} are used in the initial guess for η_i. The corresponding intensity scaling is calculated as $f_i = I(\eta_i)/(\Pi(0, \sigma_i, w_i))$.
When the peaks on each ring have been fitted with the LMA, the integrated intensity under each peak is computed as

$$: \int f_i \Pi(\eta - \eta_i, \sigma_i, w_i) d\eta = f_i \sigma_i (\pi w_i + (1 - w_i) \sqrt{\frac{\pi}{\ln 2}}). \tag{3.16}$$

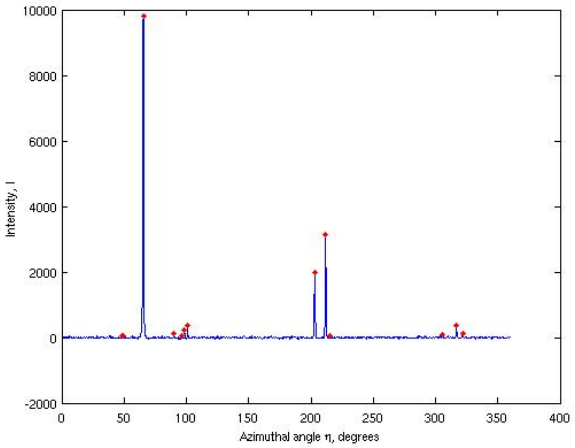

Figure 3.10: Intensity as a function of η, $I(\eta)$, for a single ring. The red dots mark the local maxima.

Parameter	Constraint	Comment
w_i	$[0, 1]$	The weights are by definition between 0 and 1.
f_i	$[0, \infty[$	The intensity cannot be negative.
η_i	$[\eta_{i,min}, \eta_{i,max}]$	The midpoint of the peak η_i is limited to a small user-set interval around the initial guess.
σ_i	$[0, \sigma_{max}]$	The width parameter is limited to a user-set value σ_{max} based on knowledge of the point spread of the detector.

Table 3.1: Parameter constraints for in the Levenberg-Marquardt algorithm.

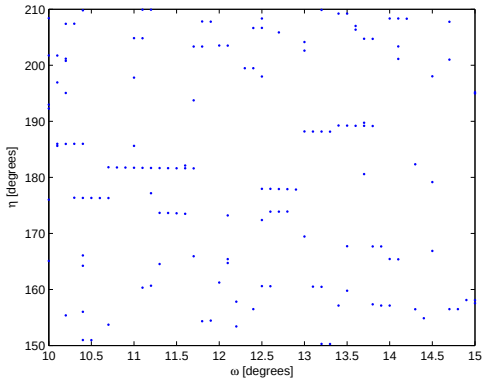

Figure 3.11: (ω, η)-values for spots for a given ring and a given y- or z-position.

The parameters obtained from the model fitting and the integrated intensity are stored in the database.
Alternatively the spots could be harvested from the images using the tools in the Fable software package (`http://sourceforge.net/apps/trac/fable/wiki`). This method does not perform caking but instead extracts the spots directly image by image. This has the advantage that 2θ is measured directly and hence the spots can be used for analysis of strain. Another alternative would be to find the spots as blobs in $(\omega, 2\theta, \eta)$-space. Each method has advantages and disadvantages and the best choice of method depends on the application and the quality of the images.

3.4.2.3 From spots to reflections

Spots in the neighboring ω-images with the same η-value are potentially from the same grain and as explained in 3.4.1.4 they are merged into reflections. This is done by taking out all spots in the database for a given ring in a given position in y or z. The intensities of the spots are normalized with the ring-current in the synchrotron to compensate for the decay in intensity between electron fill-ups.
If the η-value of a spot is within some user-set limit $\pm\delta_\eta$ of a spot in the neighboring ω-position they are connected. In fact, a reflection can spread over a large ω-interval, especially near $\eta = 0$ or $\eta = 180$ where the effect of the Lorentz factor can be seen (eq. (3.17)). Figure 3.11 shows a plot of (ω, η) where the reflections are clearly seen to spread several ω-values. The reflection's η- and ω-value are computed as intensity-weighted averages, i.e. $\sum_i I_i\eta_i / \sum_i I_i$ and $\sum_i I_i\omega_i / \sum_i I_i$. The total intensity of the reflection is the sum of all the spot intensities $\sum_i I_i$ normalized by the structure (eq. (2.11)), polarization (eq. (3.18)

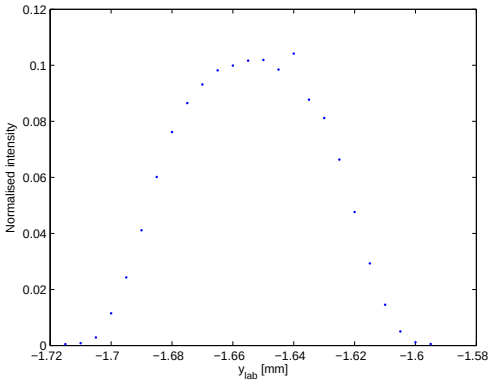

Figure 3.12: Example of a profile from experimental data built up from neighboring reflections. Notice the noisy measurement near the top of the profile.

after [33]) and Lorentz factors (eq. (3.17)):

$$\mathrm{Lor}(2\theta,\eta) = \frac{1}{\sin(2\theta)|\sin(\eta)|} \tag{3.17}$$

$$\mathrm{Pol} = \begin{cases} \frac{1}{2}(1+\cos(2\theta)^2 - \cos(2(\eta+90))\sin(2\theta)^2) & \mathrm{horizontally\ polarized} \\ \frac{1}{2}(1+\cos(2\theta)^2) & \mathrm{non-polarized} \end{cases} \tag{3.18}$$

When all spots have been connected for all rings and all y- or z-positions they are stored in the database together with the relation between the spots which contribute to which reflection.

3.4.2.4 From reflections to profiles

To build up profiles, all reflections for a given ring in either the y- or z-dataset are taken out from the dataset. Reflections from the same grain will be in neighboring positions in y or z and have similar values in ω and η within some user-set limits δ_ω and δ_η. The profiles are built up in a similar fashion as the reflections, i.e. neighboring reflections in y or z are connected if they have similar values in (ω,η), see figure 3.12. The software contains the possibility to add some intelligence to profile-building. A minimum profile width can be set, as the profile has a theoretical minimum width corresponding to the beam size. Furthermore, if a reflection is missing in the profile, the software can be set to "repair" the profile instead of splitting the profile in two or discarding it.
The projected CMS positions $\mu_y(\omega)$ or $\mu_z(\omega)$ are computed and all values are stored in the database as well as the information on which reflection contributes to which profile. This is repeated for all rings in both datasets.
To estimate the size of a grain, a spherical model of the grain can be fitted to

it's z-profiles. Assuming the beam is a perfect box of width d_b, beam position z_b and the grain is a sphere S with radius r_g and centered in z_g, i.e. $S(x,y,z) = x^2 + y^2 + (z - z_g)^2 = r_g^2 \Leftrightarrow x^2 + y^2 = r_g^2 - (z - z_g)^2$. Then a reflection in a z-profile would have an intensity which would scale with the illuminated volume of the sphere:

$$\begin{aligned} I_g &= \int_a^b \pi(x^2 + y^2)dz = \pi \int_a^b (z - z_g)^2 - r_g^2 dz \\ &= \pi[(r_g^2 - z_g^2)z + z_g z^2 - \frac{1}{3}z^3]_a^b \\ &= \pi[(r_g^2 - z_g^2)(b - a) + z_g(b^2 - a^2) - \frac{1}{3}(b^3 - a^3)]_a^b. \end{aligned} \tag{3.19}$$

where $\pi(x^2+y^2)$ is the area of a differential slice, dz, of the sphere and the limits a and b are defined by $a = max(z_b - d_b/2, z_g - r_g)$ and $b = min(z_b + d_b/2, z_g + r_g)$. Furthermore, it's integral is zero for $z_b + d_b/2 < z_g - r_g$ and $z_b - d_b/2 > z_g + r_g$, when the beam is outside the grain. By using the sum of squared differences between computations of I_g and the z-profile as a cost-function in an optimization scheme it is possible to estimate the grain's radius r_g.
The assumptions that the grains are spheres and the beam is a perfect box are of course far from correct. Still the z-profiles do contain enough information to give a reasonable estimate of r_g.

3.4.2.5 Profile matching

All profiles from both the y- and the z-datasets are retrieved from the database. For each y-profile, all z-profiles on the same ring and with similar values in (ω, η) (again user-set limits δ_ω and δ_η) are selected. Each y-profile may match several z-profiles which is accepted since it is not known beforehand which profiles that are supposed to match. In the subsequent analysis, this will be sorted out. All matches are stored in the database.

3.4.2.6 Grain indexing

As described in 3.3.2.2, the indexing is done one z-interval at a time. All 6D intersections are computed for all combinations of matches in the z-interval. Since measurements most likely contain errors, intersection in either real or Rodrigues space cannot be expected. Therefore two lines are considered as an intersection if the pass by each other closer than some small distance.
In real space this distance is typically in the order of magnitude as the step sizes Δy and Δz or less. But since all lines in real space are parallel to the xy-plane, this just corresponds to the lines' distance in z.
In Rodrigues space the distance is found by simulating the diffraction angles $(\omega, 2\theta, \eta)$ from a random orientation and adding random noise with a standard deviation of the expected measurement error to the diffraction angles. Computing the corresponding lines in Rodrigues space and finding the average distance between the lines gives an estimate Δ_{rod} of the expected distance in Rodrigues

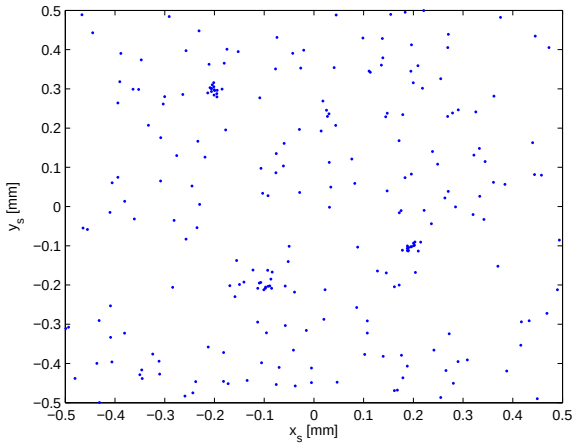

Figure 3.13: $x_s y_s$-plane of 6D space for a set of matches. The places have higher point density.

space. Repeating for multiple random orientations gives an estimate with good statistics. For a standard deviation of $3\sigma = 0.25$ degrees (applicable for most experiments) the distance is $\Delta_{rod} = 0.01$ in Rodrigues space.
When all points in 6D have been computed for this z-interval, the candidate grains are found using a k-nearest neighbor search. The semi-principal axis length of the ellipsoid used for counting neighbors is set to the step size real space and Δ_{rod} for Rodrigues space, i.e. $(\Delta_x, \Delta_y, \Delta_z, \Delta_{rod}, \Delta_{rod}, \Delta_{rod})$.
After the grain candidates have been simulated and the grains which fulfil the completeness criterion are found, the grains and the matches which contribute to them are stored in the database. The matches already contributing to one grain are left out of subsequent computations.

3.5 Verification of the Boxscan technique

The validity of the Boxscan principle is not proven until it has shown to be successfully applied to real experimental data. Hence, two experiments have been conducted on the same sample: one applying the principles of the Boxscan technique and one applying phase contrast tomography [16]. The details of the two experiments are given below.
The sample material used in the two experiments was a metastable β-titanium alloy (Ti-β-21S). The material was fabricated into a cylinder with a diameter of 300 micrometers. The sample was annealed in a vacuum for 2 hours at 830 °C such that the α-phase (hexagonal close-packed phase HCP) normally present at room temperature transformed into the β-phase (body-centered cubic BCC, $d =$ 3.2536 Å). After annealing, the sample was quenched to suppress the formation

	Vertical scan, z	Horizontal scan, y
ω, [degrees]	[0;60]	[-60;-30], [30; 60]
$\Delta\omega$ [degrees]	0.25	0.50
Translation [mm]	$z = [-14.5788; -14.4268]$	$y = [-1.7550; -1.4250]$
Step size [micrometer]	$\Delta z = 4$	$\Delta y = 5$
Beam size [micrometer]	20	30

Table 3.2: Experiment parameters for the D15 Boxscan experiment.

of the α-phase and retain the β-phase. A subsequent heat treatment at 650 °C for 15 minutes formed a thin film of the α-phase on the grain boundaries of the β-grains enabling the use of phase contrast tomography. The result was a sample with well-annealed grains with a grain radius of 25 micrometers. In the following the sample is referred to as the D15 sample.

3.5.1 Boxscan experiment

An experiment applying the principles of the Boxscan technique was conducted on the sample D15. The experiment was done at the Materials Science beamline (ID11) at the European Synchrotron Radiation Facility (ESRF) in Grenoble, France.

3.5.1.1 Experimental

In the Boxscan experiment, a horizontally polarized monochromatic X-ray beam with an energy $E = 80.6$ keV was used. The diffracted signal was recorded on a 2048×2048 far-field detector with a pixel size of $48x49$ micrometers and 16 bit dynamic range. The sample-detector distance was 241 mm allowing the 7 innermost rings to be measured.
The experimental setup used in this experiment differed from the setup described in section 3.1 in the sense that the y-translation was positioned above the ω-stage such that the translation rotates with the sample. The effect of this change is that the line confining a grain's CMS position is not equation (3.7) but instead:

$$\mu_y(\omega) = x_s \tan(\omega) + y_s + y_0. \tag{3.20}$$

Furthermore, the step size Δy is effectively changed with ω in this setup, i.e. $\Delta y_{\text{eff}}(\omega) = \Delta y \cos(\omega)$. For $\omega = 90$, Δy will be 0 since the sample then moves along the x-axis of the laboratory coordinate system. But by avoiding rotations close to $\omega = 90$ the Boxscan principle is the same and the same type of analysis can be used.
The parameters for the experiment are listed in table 3.2. From the ω-interval for the horizontal scan y the effective step size can then be calculated to be between $\Delta y_{\text{eff}}(-30) = \Delta y_{\text{eff}}(30) = 4.33$ micrometers and $\Delta y_{\text{eff}}(-60) = \Delta y_{\text{eff}}(60) = 2.50$ micrometres, i.e. the average effective step size is $\sum_i 5\cos(\omega_i)/30 = 3.55$, $\omega_i = [30 : 0.50 : 60]$.

Ring #	$< hkl >$	2θ [degrees]
1	1 1 0	3.83
2	2 0 0	5.41
3	1 1 2	6.63
4	2 2 0	7.67
5	1 3 0	8.57
6	2 2 2	9.39
7	1 2 3	10.15

Table 3.3: Miller indices and 2θ-values for the Boxscan experiment.

It is worth noticing that the overlap between the two scans is only a 30 degree ω-interval. Due to unforeseen time constraints during the experiment, it was decided to reduce the ω-interval of the vertical scan since the information in the vertical scan is redundant in the sense that $\mu_z(\omega)$ is constant. The scanned volume of the sample was set to be the volume which was illuminated in both ω-intervals $[-60; -30]$ and $[30; 60]$. The shape of this volume was a diamond in the $x_s y_s$-plane extended in the direction of z_s, see figure 3.18 (see later). A larger volume of the sample is of course illuminated but only inside this volume can a completeness of 1.0 be expected.

3.5.1.2 Data analysis

Each image was corrected for tilt and spatial distortion and caked with a resolution of 0.25 degrees in η and 0.01 degrees in 2θ. The seven rings shown in table 3.3 were extracted from each image by summing the pixels $2\theta_i \pm 0.10$ degrees around each rings. The peaks were fitted with an initial guess using a intensity threshold of $I_{min} = 25$ and the LMA was allowed to vary η by ± 0.25 degrees from the initial guess. The search for reflections was done with a threshold of $\delta_\eta = 0.25$ and the profiles were found using $\delta_\eta = 0.25$ and $\delta_\omega = 0.50$ for the horizontal scan y and $\delta_\eta = 0.25$ and $\delta_\omega = 0.25$ for the vertical scan z. Profiles were allowed to be missing one reflection along y or z and only profiles with a minimum length of $5\Delta y$ or $5\Delta z$ were accepted.
During the search for matches values of $\delta_\eta = 0.25$ and $\delta_\omega = 0.25$ were used. In the search for grains, subintervals of $\pm\delta_z = 0.002$ micrometer were used and for each subinterval the z_S was moved by 0.002 micrometer such that there was a 50% overlap between neighboring subintervals. Since only the ω-interval $[30; 60]$ has been probed during both the horizontal and vertical scans, the indexing can only be done for this small interval. Grain candidates are found using an ellipsoid with semi-principal axes $(5\mu m, 5\mu m, 5\mu m, 0.01, 0.01, 0.01)$ in 6D. When only using 30 degrees for finding grain candidates, the CMS position in the $x_s y_s$-plane is determined with a low degree of precision. To refine the position, the y-profiles in the ω-interval $[-60; -30]$ which are not matched with a z-profile are used. That is, when the grain candidate is compared with the experimental data both the matches in M_S and the unmatched y-profiles are

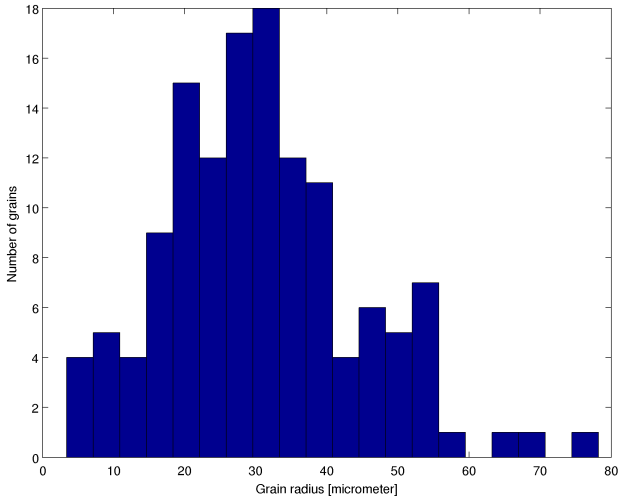

Figure 3.14: Distribution of grain radius found using the Boxscan technique.

used. Since the two ω-intervals for the horizontal scan y are perpendicular, the precision of the CMS position is increased. A completeness cut of 0.7 was used as a criteria for accepting a grain candidate as a grain.
The grain size of each grain was also computed by estimating r_g of the spherical grain model (see section 3.4.2) for each z-profile in the grain and averaging the result.

3.5.1.3 Results

The result of the Boxscan analysis was 133 grains found inside the scanned volume of the sample. The average completeness of the grains was 0.86. The average grain radius was found to be 30.6 micrometers which agrees well with what was stated above (25 micrometres). Figure 3.14 shows a distribution of the grain radii found using the Boxscan technique.

3.5.2 Phase contrast tomography verification experiment

For verification of the Boxscan experiment, a phase contrast tomography (PCT) scan was done on the same D15 sample. The experiment was done at the Imaging Beamline (ID19) at the European Synchrotron Radiation Facility (ESRF) in Grenoble, France.

3.5.2.1 Experimental

The thin film of α-phase on the boundaries of the β grains produced during the second heat treatment of the sample enables the grains to be visualised. The

Figure 3.15: Cross section of the reconstructed D15 sample from the phase contrast tomography scan. The diameter is approximately 300 micrometres.

sample was scanned and reconstructed with a voxel size of 0.56 micrometer. Figure 3.15 shows a cross-section of the sample.

3.5.2.2 Data analysis

To extract the grains from the phase contrast scan a number of steps are necessary. First, the circular structures in figure 3.15 are so-called ring artefacts and must be removed as they have an intensity similar to the one of the grain boundaries. To remove the ring artefacts, a ring correction tool for Matlab was developed based on a Photoshop macro written by Paul Tafforeau at ID19, ESRF. The steps of the ring correction are shown schematically in table 3.4. The rings appear in the reconstructed volume when a pixel on the detector is "dead" or saturated and thus gets "smeared" out in the reconstruction algorithm. They are highly non-linear but are assumed to be additive. Due to the 180 degree scan of the phase contrast tomography scan, the artifacts will actu-

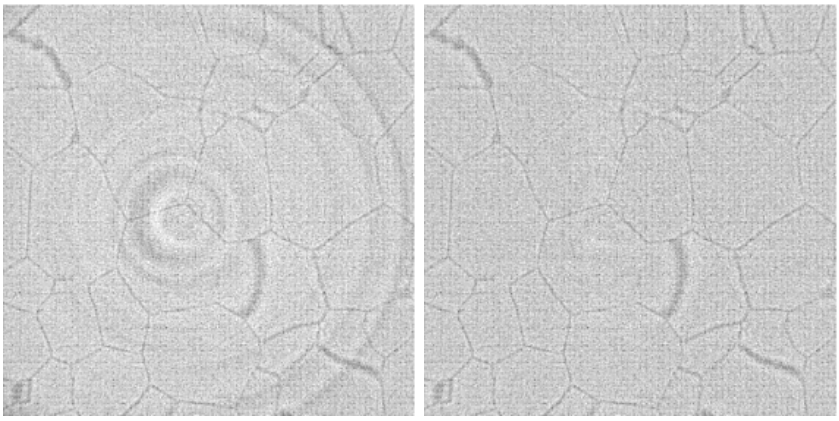

Figure 3.16: Before and after image of the reconstructed grain structure when ring correction has been applied. Each image is approximately 150 by 150 micrometres.

ally be half-rings in the image. A before and after image of the reconstructed grain structure is shown in figure 3.16.
Even though the grain boundaries are clear to the eye, simple image processing steps such as filtering combined with thresholding are not enough to segment out the individual grains. The steps involved in segmentation of the grains are shown in table 3.5. The result of the segmentation process is not perfect but approximately 95% of the grains are segmented out correctly. The last 5% have to be manually corrected.

3.5.2.3 Results

After the images have been corrected for ring artefacts and the segmentation process had been applied, 431 grains could be found, see figure 3.17. The individual CMS position and grain radius of each grain was computed to allow for direct comparison with measurements from the Boxscan experiment.

3.5.3 Comparison

To compare the results from the Boxscan and the verification experiment, it is first necessary to find the rotation matrix and translation vector which brings the two datasets to coincide (or close to). For this, the iterative closest point algorithm (ICP) is used [37]. The ICP finds point correspondence by moving the points towards their nearest neighbor in the other dataset. The ICP is dependent on a good initial guess and hence manual selection of points which correspond is needed. Using information on the grain radius, it is possible to find the largest grains in both datasets and use these to find a good initial guess. When correspondence between the two datasets had been found, the CMS positions from the phase contrast experiment inside the scanned diamond-shaped

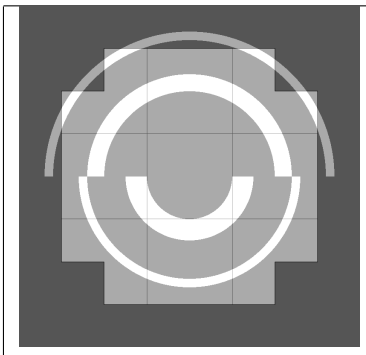 1. The image A containing both the imaged object and the ring artefacts is filtered with a large kernel to give A_f.	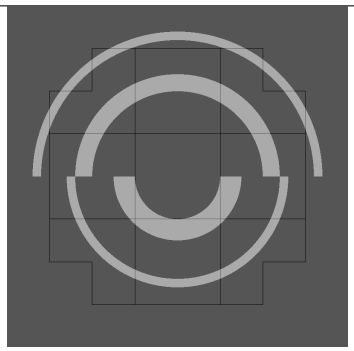 2. The filtered image is subtracted from the original, $A_d = A - A_f$, leaving the rings and the high frequency details.
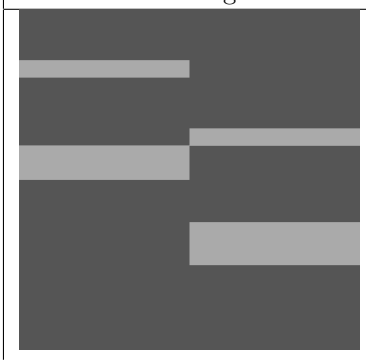 3. A_d is polar transformed so the rings become lines. A median filter is applied in the azimuthal direction to remove details. The image is split in two halves A_1, A_2 where the rings begin and end.	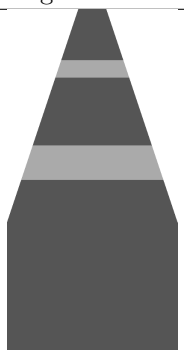 4. The pixels closest to the original image's centre (on both halves) are resized to compensate for the polar transformation and a Gaussian filter is applied.
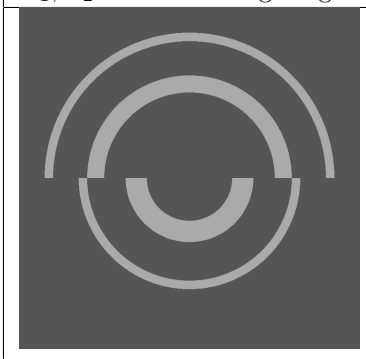 5. A_1, A_2 are assembled again and inverse polar transformed. This image, A_r, contains the estimated ring artefacts.	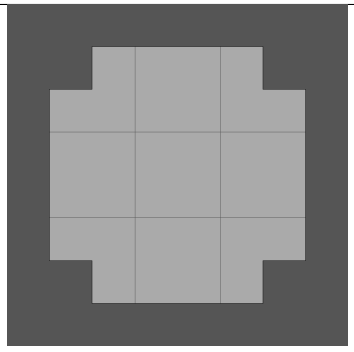 6. The original A is subtracted the estimated rings A_r to give an image with no ring artefacts.

Table 3.4: Steps of the ring correction method.

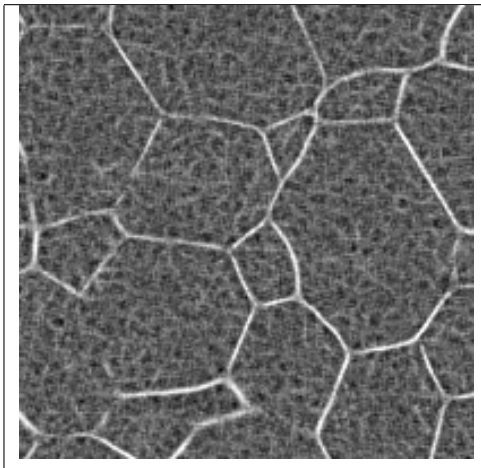 1. First the images are correlated with a model of the grain boundary. This way the edges are enhanced and noisy pixels are suppresed.	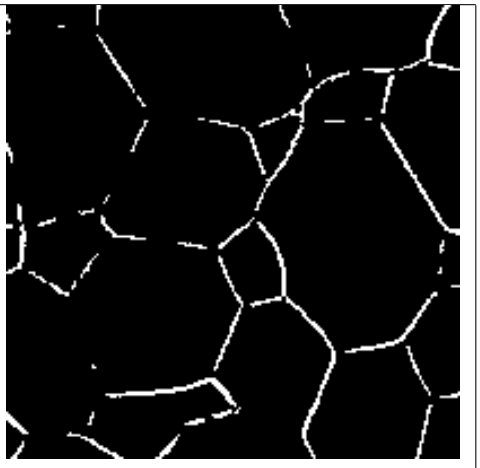 2. Applying a threshold and removing single spurious pixels gives parts of the grain boundaries.
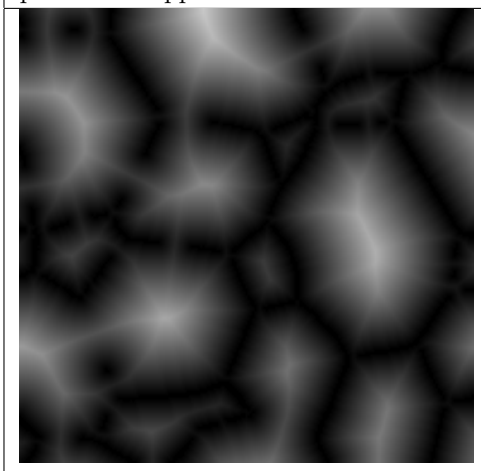 3. The Euclidean distance transform is applied in 3D.	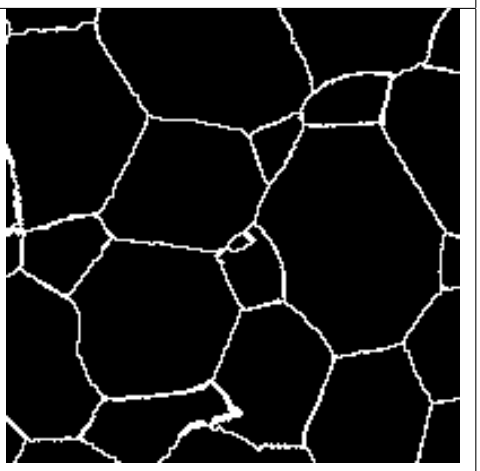 4. Applying the watershed operation in 3D repairs the broken grain boundaries.

Table 3.5: Steps of the ring correction method.

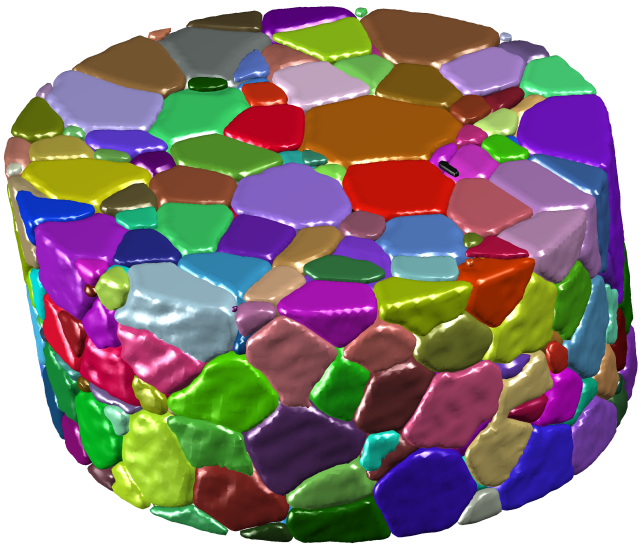

Figure 3.17: Part of the D15 sample segmented from phase contrast tomography. The diameter of the sample is 300 micrometres. Random coloring scheme.

volume form the Boxscan experiment was extracted. In total 159 grains from the PCT experiment had CMS positions in this volume. Out of 159 found in the verification experiment, 129 were found in the Boxscan experiment, i.e. a difference of 30 grains.
Further analysis of the data showed that the difference of 30 grains had several reasons. 17 smaller grains with a grain radius smaller than 8 micrometers were not found. 14 of the 30 grains were on the edge of the scanned volume, meaning their profiles were truncated. 4 grains out of the 30 were classified both as small grains and were on the edge of the scanned volume. 3 grains of the 30 grains not found were medium-sized grains in the center of the scanned volume.
Furthermore, 4 grains from the Boxscan experiment were not found in the verification data, i.e. false positives or fake grains.
The average error of the CMS positions of the 129 grains correctly determined by the Boxscan experiment was found to be 2.6 micrometers. The average error on the orientation was 0.7 degrees compared to the orientation found by applying the GrainSpotter from the Fable software package to the Boxscan data (`http://sourceforge.net/apps/trac/fable/wiki`). The average error in the estimated grain radius was 4.6 micrometers.

3.5.4 Discussion

In the previous section, comparison between a Boxscan and a verification phase contrast tomography experiment on the same sample was performed. The primary reason that the 17 smaller grains were not detected by the Boxscan tech-

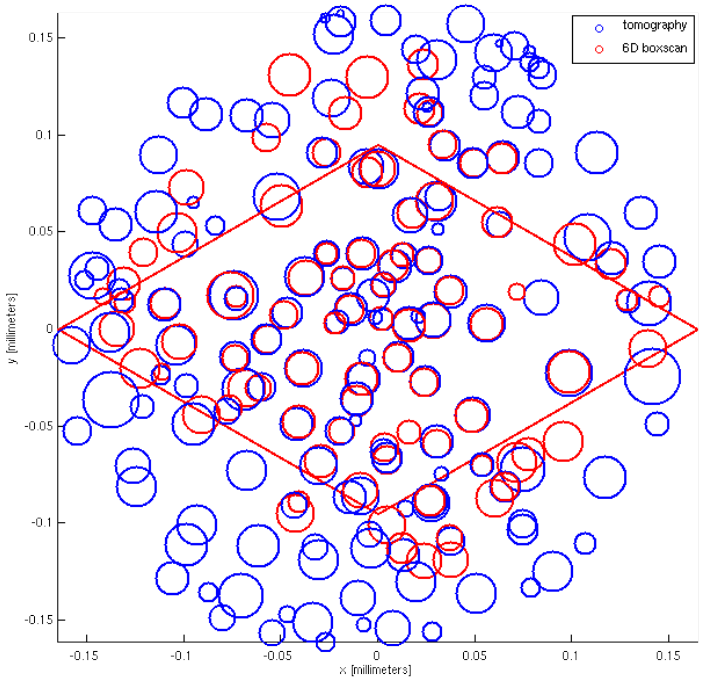

Figure 3.18: Subset of Boxscan and phase contrast tomography results plotted on top of each other. The size of the circle scales with the grain radius. The red diamond is the scanned volume in the Boxscan experiment.

nique was due to their spot intensities. Especially for the higher order Debye-Scherrer rings, small grains can have a spot intensity which is lower than the threshold applied when fitting the spots. One solution could be to decrease the threshold, but the more this threshold is decreased the more noise points are included in the analysis. Another way to attack the problem would be to use a threshold which scale with the structure factor. Finally, computing the completeness per Debye-Scherrer ring instead of per grain would maybe reveal the smaller grains on the low order rings which could then be used for doing another search on the higher order rings.

14 grains were not found because they were on the edge of the scanned volume. When only a sub-volume of the sample is scanned, almost all grains near the edge of the scanned volume will have truncated profiles. This leads to an error in the estimate of $\mu_y(\omega)$ or $\mu_z(\omega)$ meaning that it will not correspond to the predictions of the CMS positions based on the geometry. The truncated profiles are difficult to get rid of if only a sub-volume is scanned. Although it should be possible to make the indexing routine more intelligent by checking if a grain candidate was close to the edge of the scanned volume. In that case, truncated profiles could be expected and higher deviations from the predicted $\mu_y(\omega)$ or $\mu_z(\omega)$ should be accepted.

Errors when fitting the peaks will travel up through the analysis. An error in a peak will be an error in a reflection which will be an error in a profile which may get filtered away based on this. Due to these kind of errors, the three medium sized grains were not found even though they were in the center of the scanned volume. A more intelligent profile-builder could maybe solve this by allowing the corrections to propagate back though the reflections and the spots.

The 4 false grains are due to the fact that the 6D space will contain intersections between matches coming from the same grain as well as different grains. When only a sub-volume of the sample has been scanned, the dataset will contain many profiles from grains which are not in the scanned volume. These profiles will get matched and eventually add points to 6D space. If the sub-volume is small compared to the rest of the sample volume, the ratio between profiles from grains inside the scanned volume and outside is small and hence 6D space will contain many points which are not from real grains.

The 2.6 micrometers error in CMS positions is a rather low error compared to the step sizes. This is of course due to the fitting of the position from knowledge about the geometry of the setup. The 0.7 degree error in the orientation compared to the alternative method could be related to the fact that the grains move when the sample is rotated, hence the diffraction spots on the detector will also move up to a few pixels. For grains in the center of the sample this effect is negligible but for grains more than a few pixel sizes away from the center it will be measurable.

Chapter 4

Reconstruction of 3D grain maps

The basic implementation of the Boxscan technique in the previous chapter gave us a tool to extract centers of mass and orientations for individual grains in a polycrystalline sample. To be able to fully explore and study morphology, topology and other fundamental properties of the grain structure, a volumetric description is desirable. Such a description is often referred to as a three dimensional grain map. In this chapter, a number of methods for reconstruction of 3D grain maps from Boxscan data are studied. First the use of Laguerre tessellations is presented and it's application to Boxscan data is described. Next, the use of the algebraic reconstruction technique (ART) is explored and finally a more theoretical study of the amount of data needed to successfully reconstruct grains in 3D from Boxscan data is presented.

4.1 Laguerre tessellation-based 3D grain maps

4.1.1 Introduction

From many years experience with polycrystalline materials it is well-known that well-annealed samples have a 3D grain structure where the grain shapes are almost convex shapes. This is mainly due to the energy-minimizing nature of the grain boundaries which also can be seen in e.g. foams and soap bubbles [38]. Assuming that grains are convex and space-filling there exists a number of ways to subdivide the sample space into convex polyhedra with planar faces. The probably most well-known method is the Voronoi tessellation [39] which e.g. has been used for studies of plasticity [40, 41] and for statistical descriptions of microstructures [42]. The Voronoi tessellation simply assigns points $\boldsymbol{X}$ in space to the Voronoi cell with the smallest distance between the Voronoi seed point and $\boldsymbol{X}$ using an Euclidean distance measure.
An extension of the Voronoi tessellation by an additive weight is called an addi-

tively weighted Voronoi tessellation or a Laguerre tessellation [39]. The Laguerre tessellation has previously been used in simulation studies of grain growth and coarsening in 2D by extending the model with motion equations [43, 44]. A similar study but in 3D was reported in [45] and in [46] a simulated 3D grain structure based on a Laguerre tessellation was reported to follow a theoretical grain size distribution. In [47] the Laguerre tessellation was used in combination with an optimization scheme to simulate realistic 3D microstructures from 2D experimental input. Common to these results is that they all focus on the overall result in terms of grain size distributions and validate against theoretical results or 2D experimental observations.
The Laguerre tessellation is a representation of the underlying grain structure based on a set of measurements of center of mass and size of the individual grains. The resulting Laguerre tessellation is not expected to give the correct morphology of the grains in the grain structure, for that purpose the model is too simple, but it is expected to give a representation of the grain structure with a more correct topology than for a Voronoi tessellation. If the results show as expected, the Laguerre tessellation could form the basis for applications such as grain-grain interactions under deformation [48] or grain growth studies [49] where, to the first approximation, only information on grain neighborship is needed and not the exact grain morphology.
In the following, 3D Laguerre tessellations are explained, implemented and compared with true 3D experimental validation data to study to what extent the Laguerre tessellation preserves the topology of the grain structure.

4.1.2 Laguerre tessellations

As mentioned above, the Laguerre tessellation is an extension of the Voronoi tessellation by an additive weight. In terms of mathematics, the Laguerre tessellation is a subdivision of space into a set of n cells C_i given by a set of sites $\boldsymbol{p}_i = (\boldsymbol{s}_i, w_i), i = 1 \dots n$, where $s_i \in \mathbb{R}^d$ is a seed point in d-dimensional space and w_i is a scalar weight. Each cell C_i is given by the points fulfilling:

$$C_i = \left\{ \boldsymbol{X} \in \mathbb{R}^d \middle| \quad ||\boldsymbol{X} - \boldsymbol{s}_i||^2 - w_i < ||\boldsymbol{X} - \boldsymbol{s}_j||^2 - w_j, \quad i \neq j \right\} \tag{4.1}$$

Each cell C_i is convex, has planar faces and is non-overlapping with any other cell in the tessellation, see figure 4.1.
There are several ways to interpret the Laguerre tessellation as it is formulated in equation (4.1). One way is to image the Laguerre seed points s_i as nuclei embedded in a deformed matrix where the growth conditions are isotropic. If all nuclei grow into the deformed matrix with the same speed but start growing at different time points according to their weight then they will eventually fill up the entire space. Another way is to see the Laguerre tessellation as an intersection of spheres with different radii defined by $\sqrt{w_i}$.
If all the weights w_i are equal the Laguerre tessellation is equivalent to a Voronoi tessellation. Even though there are many similarities between properties of the Voronoi and the Laguerre tessellation, there are also some differences. The cells

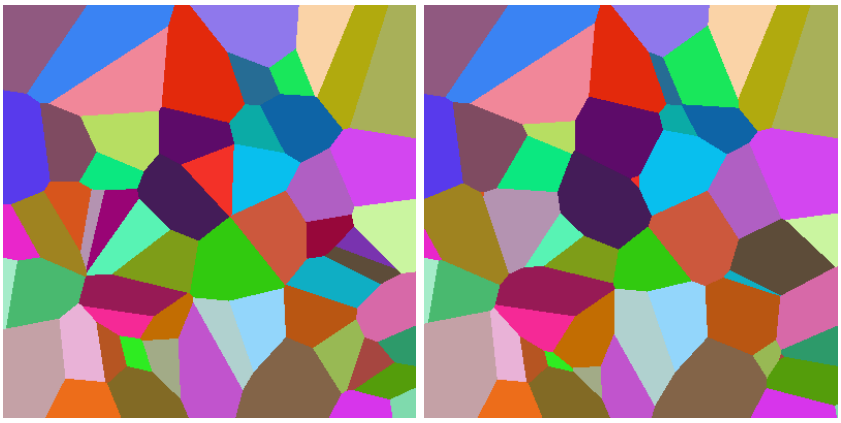

Figure 4.1: A Voronoi tessellation (left) and a Laguerre tessellation (right). The seed points are the same for both tessellations but the Laguerre tessellation is generated with random weights.

of a Voronoi tessellation always have a volume which is greater than zero if no two seed points $\boldsymbol{s}_i$ are the same. This is not the case for the Laguerre cells, where the volume can be zero, i.e. the cell is empty. This can e.g. happen if a cell with a small weight is surrounded by cells with very large weights. Furthermore, where the seed point $\boldsymbol{s}_i$ is always contained inside the corresponding Voronoi cell, this is not always fulfilled for the Laguerre tessellation. Imagine a setup with two seed points close together and one weight is slightly larger than the other. In this case, the cell with the larger weight can push the face between the two cells such that it will contain both seed points.
Taking a glance back at equation (4.1) the comparison with a sphere is evident in the sense that $||\boldsymbol{X} - \boldsymbol{s}_i||^2 - w_i = 0$ describes the surface of a sphere centered in $\boldsymbol{s}_i$ and with radius $r_i = \sqrt{w_i}$. Assuming the Laguerre cells are spherical, this can be used to give an estimate of the weight $\widetilde{w}_i$ if the volume V_i of the cell is known:

$$V_i = \frac{4}{3}\pi\widetilde{r}_i^3 = \frac{4}{3}\pi\widetilde{w}_i^{\frac{3}{2}} \Leftrightarrow \widetilde{w}_i = \left(\frac{3V_i}{4\pi}\right)^{\frac{3}{2}} \tag{4.2}$$

Since the weight $\widetilde{w}_i$ is estimated based on the assumption that the Laguerre cell is spherical, it is generally not true that the volume of the reconstructed cell C_i will be equal to V_i.
From experimental data from e.g. the Boxscan technique it is possible to measure the center of mass of a grain and it's volume. In general, the center of mass $\boldsymbol{\mu}_i$ of the Laguerre cell is not equal to the seed point $\boldsymbol{s}_i$ (this also holds for Voronoi cells). Think of a counter example such as the case where a Laguerre cell does not contain it's own seed point. In this case the seed point is outside the Laguerre cell but the center of mass is inside due to convexity. Yet it is possible to give a rough estimate of the seed point $\boldsymbol{s}_i$ if only the center of mass $\boldsymbol{\mu}_i$ and weight w_i is known. Consider a Laguerre cell C_a described by $(\boldsymbol{s}_a, w_a)$

where only the center of mass $\boldsymbol{\mu}_a$ and the weight w_a is known. Now consider a Laguerre cell C_b described by $(\boldsymbol{s}_b, w_b) = (\boldsymbol{\mu}_a, w_a)$, i.e. the seed point of C_b is the center of mass of C_a and the weight is the same. If the neighboring cells are the same, it is assumed that the shape and size of C_a and C_b are the same, hence the center of mass $\boldsymbol{\mu}_b$ is only spatially shifted slightly compared to $\boldsymbol{\mu}_a$, see figure 4.2. Defining a shift vector $\boldsymbol{h_i} = \boldsymbol{\mu}_i - \boldsymbol{s}_i$ and assuming the spatial

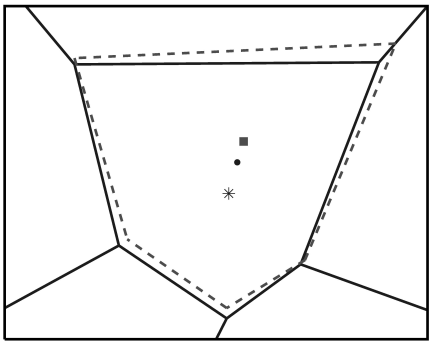

Figure 4.2: Laguerre cell C_a and C_b. The estimated seed point $\boldsymbol{s}_a$ (star *) is calculated from $\boldsymbol{\mu}_a$ (bullet •) and $\boldsymbol{\mu}_b$ (square ■)

shifts are the same due to cell similarity, i.e. $\boldsymbol{h}_a = \boldsymbol{h}_b$, it is possible to estimate $\boldsymbol{s}_a$:

$$\begin{aligned} \boldsymbol{h}_a &= \boldsymbol{h}_b \quad \Leftrightarrow \\ \boldsymbol{\mu}_a - \boldsymbol{s}_a &= \boldsymbol{\mu}_b - \boldsymbol{s}_b \quad \Leftrightarrow \\ \boldsymbol{\mu}_a - \boldsymbol{s}_a &= \boldsymbol{\mu}_b - \boldsymbol{\mu}_a \quad \Leftrightarrow \\ \boldsymbol{s}_a &= 2\boldsymbol{\mu}_a - \boldsymbol{\mu}_b \end{aligned} \tag{4.3}$$

Thus, to generate a grain map based on a Laguerre tessellation only from the center of masses and volumes of the grains, it is necessary to compute the Laguerre tessellation twice: The first tessellation is done to find an estimate of $\boldsymbol{s}_a$ and the second then is the grain map tessellation.

4.1.3 Implementation

The implementation of the method was done in Matlab. A set of centers of masses in 3D and weights was fed to the algorithm and the resulting Laguerre tessellation was output as a voxelized volume. Basically the algorithm probes every voxel $\boldsymbol{X}$ in the volume and finds the grain to which it belongs by computing the distance $||\boldsymbol{X} - \boldsymbol{s}_i||^2 - w_i$ for all i.

4.2 Algebraic reconstruction technique

4.2.1 Introduction

The 3DXRD and the DCT described in the introduction chapter both offer the possibility to produce 3D grain maps of grain structures. In the case of a 3DXRD setup where the sample is scanned vertically with a horizontal line beam and the diffracted signal is recorded on both a near-field and a far-field detector, successful reconstructions of the grain structure using an Algebraic Reconstruction Technique (ART, [50, 51, 52, 53, 54]) has been reported in [55, 56, 57]. Similarly, in the DCT framework where both the diffracted and direct beam signals of the grains are available, ART can also be used in the reconstruction of the grains shapes, see e.g. [15]. In [58] ART has also been applied in reciprocal space to reconstruct the orientation distribution from a single grain.
ART is a general method for solving linear systems $\mathsf{A}\mathbf{x} = \mathbf{b}$ but it has proven well-suited for problems coming from the field of materials science dealing with reconstructions from diffraction as the problems in this field are easily posed as linear systems.
Until now, ART has only been used for reconstructing 3D grain shapes from 2D projections. The goal is to study the use of ART on Boxscan data, which inherently is 1D, for reconstructing the 3D grain shape. A successful reconstruction is the first step towards producing full grain maps of samples scanned with the Boxscan technique.
In the following, the theory of the ART technique is described and the process of constructing linear systems from Boxscan data for a single grain is explained. Furthermore, the details of the ART-implementation is reported.
The results of the ART are presented in 4.4.2.

4.2.2 Algebraic Reconstruction Technique

As mentioned above, ART is a method for solving m linear equations with n unknowns, $\mathsf{A}\mathbf{x} = \mathbf{b}$, where the coefficient matrix A is size $m \times n$, the solution vector $\mathbf{x}$ is $n \times 1$ and the measurement vector $\mathbf{b}$ is a $m \times 1$. Various flavors of ART exist (see [50]), but common to them all are the iterative production of new solutions $\mathbf{x}_{k+1}$ by projecting the current solution $\mathbf{x}_k$ onto a row $\mathbf{a}_i$ of A. The ART used in this study is termed randomized ART, i.e. new solutions are found from:

$$\mathbf{x}_{k+1} = \mathbf{x}_k + \lambda \frac{\mathbf{b}_i - \mathbf{a}_i \mathbf{x}_k}{||\mathbf{a}_i||^2} \mathbf{a}_i \tag{4.4}$$

where $\mathbf{a}_i$ is a random row in A and λ is a relaxation parameter. Randomizing the choice of row, speeds up the convergence as two neighboring rows are more likely to be near-linear dependent. The relaxation parameter λ is introduced to make the method robust towards noise in the measurements $\mathbf{b}_i$ and is given a value between 0 and 1.
Geometrically, a linear system can be seen as m hyperplanes described by A and $\mathbf{b}$ in n-dimensional space. The solution $\mathbf{x}$ to the linear system can be seen

as the place where all the hyperplanes intersect. In this n-dimensional space, ART finds the solution by projecting the current solution $\mathbf{x}_k$ onto a random hyperplane. Figure 4.3 shows graphically how the solution evolves in a simple example with $n = m = 2$. Following the proofs in [52, 53] the solution $\mathbf{x}_k$ will converge to the true solution for $k \to \infty$.

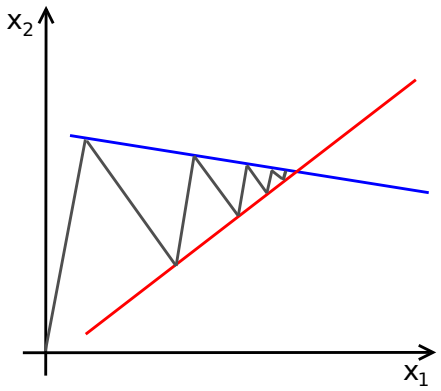

Figure 4.3: Finding solutions with ART in two dimensions: The blue and the red line each represent a row in the A-matrix. The gray line is the evolution of the solution $\mathbf{x}$ as k progresses.

4.2.3 Constructing linear systems from boxscan data

Consider a grain found using the Boxscan technique. The real space information available about the grain is the CMS position, the grain radius (i.e. the grain volume) and a set of y-profiles and z-profiles. For a point (t, I) in a profile, where I is the measured intensity and t is the position in y or z, the intensity I will scale linearly with the integral of the subvolume of the grain which is illuminated by the beam at position t. This is due to the fact that each unit cell in the grain contributes equally to the diffracted intensity.
The sample space is subdivided into n voxels. The voxel size should be chosen such that it is small enough to model the features on the grain which are of interest. The relationship between the sample coordinate system and the laboratory coordinate system is known as well as the beam dimensions, hence the fraction of each voxel which is illuminated at a given position t can be computed. For each (t, I) in a profile belonging to the grain, the voxels are given a weight w_j between 0 and 1 according to the fraction of illumination, i.e. how much they contribute to the measured intensity I. Given that vector $\mathbf{x}$ contains the n unknown voxel intensities, it must then hold that:

$$\sum_{j=1}^{n} w_j x_j = I \tag{4.5}$$

Repeating this procedure for all positions in the profiles of the grain, the problem can be formulated as a linear system:

$$\mathsf{A}\mathbf{x} = \mathbf{b} \tag{4.6}$$

where the weights w_j are placed as rows in the A-matrix and I is placed in $\mathbf{b}$ at the same index.
Under the assumption that each voxel is either completely void or filled by the grain, the values of the vector $\mathbf{x}$ will either be 0 or 1. However, solving the linear system from equation (4.6) using ART, will typically give a solution $\mathbf{x}$ which is real valued and not binary. But by first solving the system using ART and then thresholding this real valued solution, a binary solution can be found. The threshold value is chosen such that the volume of the solution is the same as the measured grain volume.

4.2.4 Implementation

An implementation of the ART framework was made in Matlab. The implementation was limited to only handle perfect boxbeams to simplify the computation of the weights w_j. Instead of the whole sample, only a neighborhood around the grain's CMS position was voxelated. The size of the neighborhood was based on the measurement of the grain radius. Each profile belonging to the grain was normalized to have a summed intensity of 1. For each point (t, I) on the normalized profile, the voxelated neighborhood was rotated according to the profiles ω-value and the fraction of illumination for each voxel was computed. With a definition of the A-matrix as described above, the matrix will be sparsely populated with weights greater than zero. This is simply because the beam only illuminates a small sub-volume of the grain at each position t. To save memory, the A-matrix is stored in a structure where only non-zero elements are kept.
During the iterative computations of equation (4.4), a figure of merit of the solution is monitored. The figure of merit is computed as:

$$\text{fom}_k = \frac{||\mathsf{A}\mathbf{x}_k - \mathbf{b}||}{||\mathbf{b}||} \tag{4.7}$$

The figure of merit will be 1 for $\mathbf{x}_k = 0$ (initial solution) and 0 for the ideal solution. As the calculations are performed on a computer with finite precision, the ideal solution is not expected to be found. Furthermore, the input to the linear system may be corrupted with measurement noise that evidently will affect the solution.
To check if the solution has converged to an acceptable solution, a number of stopping criteria based on this figure of merit has been defined. First, if the figure of merit is less than some value, $\text{fom} < f_a$, the computations are terminated. Second, if the change in figure of merit is less $\text{fom}_{k+1} - \text{fom}_k < f_b$, the computations are terminated, as this is an indicator that the solution is close to the ideal solution. Furthermore, if the maximum number of iterations exceeds f_c, the computations are also terminated.

4.3 Linear programming

During the work with ART (sections 4.2.2 and 4.4.2), the question about how much Boxscan data is needed to reconstruct the 3D shape of a grain appeared. If a sample is scanned with the Boxscan technique with the purpose of reconstructing the 3D shape of all the grains in the volume of interest then the minimum required number of profiles needed to reconstruct a single grain is a highly useful number. With such a number at hand, the experimental parameters can be tuned such that there is information enough to reconstruct all grains correctly or at least within some error limit.

4.3.1 Introduction

Within the field of conventional tomography and discrete tomography, linear systems play an important role. In both cases, the object is to find a solution to the linear system $\mathsf{A}\mathbf{x} = \mathbf{b}$ given some assumptions and constraints.
In conventional tomography [50], $\mathbf{x}$ is a real-valued vector of length n, hence to find a unique solution, the matrix A must hold information from at least n linear independent equations. If there are less than n linear independent equations, then the solution found will not be unique. The number of linear independent equations is determined by the number of projection directions, thus in a practical application, the number of projections is just increased until there are enough linear independent equations.
In discrete tomography [59, 60], $\mathbf{x}$ is not a real-valued but a binary 0/1-vector of length n. This constraint decreases the required number of linear independent equations to find a solution to the system. It is possible to solve the system with n equations but some of the information is redundant. It is therefore interesting to find the minimum number of linear independent equations needed to find the unique solution to the system.
As was described in 4.2.2, the 3D shape of a grain is represented as a binary 0/1-vector, hence the number of linear independent equations should be less than n. When the grain has been scanned using the Boxscan technique, the number of linear independent equations is determined by the number of profiles, hence it would be interesting to know how many Boxscan profiles are needed to perfectly reconstruct the 3D shape of the scanned grain.
This kind of problem is similar to the problems within the field of geometric tomography [61]. Geometric tomography is a mathematical discipline which deals with retrieving information about geometric shapes from projections. Knowledge from this field of science is valuable when dealing with shape reconstructions as it sets the theoretical limits of what type of results can be expected from experimental data. In [62] it was shown that a 2D convex shape always can be retrieved using any 7 projections. As the shape reconstruction in the Boxscan case is 3D and the dimension of the projections are the same as in the 2D case, then from intuition at least 7 projections should be the required. Still, it should be kept in mind that grains are not perfect convex structures and such

a theoretical result may not be directly applied to practical applications, but it will still give an idea of the number of projections needed to get a reasonable result.
Interestingly enough, the shape reconstruction of grains from Boxscan data is a special case of an open problem within the field of geometric tomography, hence little knowledge exists on this specific problem. The open problem is stated in [61, p. 82, Problem 2.5].
In the following, the minimum required number of profiles needed to reconstruct a 3D shape will be studied. The study is not a theoretical study such as [62], but a practical one, which aims at quantifying the reconstruction error of a voxelized 3D shape as a function of the number of Boxscan profiles.

4.3.2 Linear Programming

In this study the aim is first of all to find a solution to a linear system and second to test if this solution is unique. This cannot be done with ART in a trivial way, so instead linear programming is used. The advantage of linear programming over ART is that it is possible to test if the solution found is unique.
Linear programming was developed as a mathematical technique around the time of World war II. The development of the technique is assigned to Kantorovich [63], Danzig [64] and Von Neumann [65].
Linear programming is a method for optimizing the use of limited resources. A typical example could be to maximize the linear objective function $f = c_1x_1 + c_2x_2$ subject to the constraints:

$$\begin{aligned} 0 \leq x_1 \leq b_1 \\ 0 \leq x_2 \leq b_2 \\ x_1 + x_2 \leq b_3 \end{aligned}$$

Figure 4.4 shows a sketch of the constraints superimposed on the expression f. The region inside the constraints is called the *feasible region*. As f is a linear expression and the constraints are linear, the maximum of f must be on one of the edges or on one of the vertices of the constraint polytope. In this 2D example, it is easy to manually find a solution by probing for the value of f at each vertex or edge, but already for a 3D polytope it gets more complicated. Figure 4.5 shows a relatively simple feasible region in 3D, yet the number of vertices and edges has already grown significantly. Thus, when the number of constraints gets very high, a systematic method is needed to find the solution.
One of the first techniques to solve linear programming problems was Danzig's simplex method [64]. From an initial vertex, the simplex method goes from vertex to vertex via the edges of the feasible region in such a way that the objective function is non-decreasing. As long as the method does not get stuck in the same circular path where the increase of the objective function f is zero (maybe due to finite representation of numbers), the optimal solution will be found.
Many other techniques for solving linear programming problems have been de-

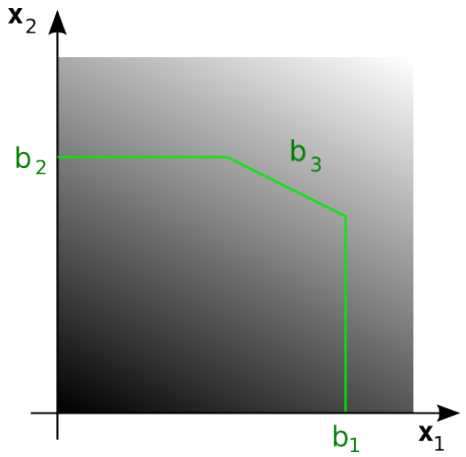

Figure 4.4: Constraints superimposed on the linear expression f to show the feasible region. The lighter the color, the higher value of the objective function f.

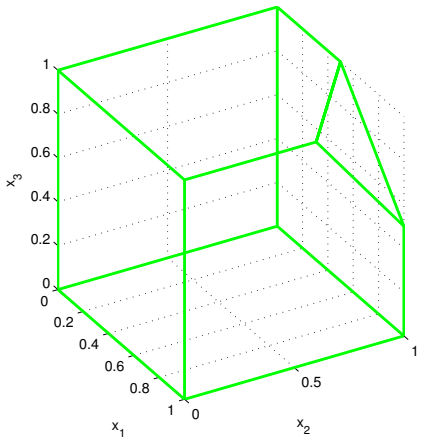

Figure 4.5: Example of a 3D feasible region.

veloped along the years and it is out of the scope to describe them here. Instead, thorough descriptions can be found in [66, 67]. Each method is suitable for certain types of problems, e.g. problems with many constraints, and today many linear programming software packages contain implementations of several solvers.

4.3.3 Shape Reconstruction

4.3.3.1 Data

The linear systems used in this study are constructed in a way similar to the ones used in the ART study (section 4.2.3), where each row in A contains numbers between 0 and 1 according to how much each voxel is illuminated and the vector $\mathbf{x}$ will hold the values 0 or 1. The most significant difference in how data is constructed is that the profiles are not restricted to y- and z-profiles but can be constructed from any scanning direction, i.e. corresponding to the ω-axis which can point in any direction instead of only being parallel to the z-axis.

4.3.3.2 Applying linear programming to shape reconstruction data

When solving this kind of linear system, the aim is to find a solution $\mathbf{x}_k$ to the system $\mathsf{A}\mathbf{x} = \mathbf{b}$. Where normal linear programming problems consist of a system of inequalities, the problem to be solved here is a linear system of equations. Nonetheless, a solution can still be found using the methods mentioned above. But instead of a feasibility region, it would be more correct to use the term feasibility surface, as the solution needs to exist on the surface of the polytope spanned by the constraints.
Furthermore, when finding a solution $\mathbf{x}_k$ to this kind of linear system, the objective function is set to zero. An objective function different from zero is only needed, if it is necessary to favor one kind of solution over another. This is useful when searching for several solutions to the same linear system and is done by solving the exact same linear system again, but now by minimizing the objective function $f = \mathbf{x}^T\mathbf{x}_k$, i.e. the voxels equal to 1 in the original solution should be minimized. By defining the objective function this way, the linear programming method will favour solutions which are far away from $\mathbf{x}_k$.
The drawback of using linear programming is that the solution is not binary 0/1 but can only be limited to real values in the interval $[0, 1]$. Nonetheless, if the solution to the linear system exist, it can still be found by linear programming as the only difference is that the solution space is expanded.

4.3.3.3 Finding solutions using CPLEX

To solve the linear system $\mathsf{A}\mathbf{x} = \mathbf{b}$, the CPLEX optimization software package is used. CPLEX is a commercial product from ILOG so few details on how the software works inside the engine exist, yet the CPLEX documentation [68] lists the set of different optimizers that can be used for solving a given problem. CPLEX also has a built-in presolver that can be applied to speed up computations and save memory. During the initial experiments with CPLEX it was clear that the presolver caused problems in the sense that certain feasible problems were turned into an infeasible problem after presolving. This problem had been reported on CPLEX internet forums but no solution or work-around had been suggested. To avoid this problem, the presolver was disabled.

To input A and $\mathbf{b}$ from the linear system to CPLEX, the LP file format described in [69] was used. A Matlab script was written which easily converted Matlab matrices to textfiles with the correct LP-format. To find the solution $\mathbf{x}_k$, CPLEX was set to minimize the objective function $f = 0$. After feeding the LP-file to CPLEX, CPLEX was run with no choice of optimizer leaving it up to CLPEX to find the most suitable one for this specific problem. The solution found was written to an XML-file [69] which could be read by Matlab.
As it is possible to search for alternative solutions to the same linear system, the same linear system was feed to CPLEX but now with the objective function $f = \mathbf{x}^T\mathbf{x}_k$. If the initially found solution was equal to the solution found with the alternative objective function, then this would show that the initial solution was not unique.

4.4 Verification

4.4.1 Laguerre tessellations

To verify that the Laguerre tessellation is better at modeling a measured grain structure than the Voronoi tessellation an experiment was done. The following reports and explains the results of the experiment.

4.4.1.1 Experimental

A meta-stable beta-titanium alloy sample (Timet β21S) was scanned in a microtomography setup at ID19 beamline at the European Synchrotron Radiation Facility, Grenoble, France. The sample was from the same production batch as the sample used for verifying the Boxscan technique and with similar properties except the time of the second heat-treatment was 2 hours instead of 15 minutes (see section 3.5). The sample was in the shape of a cylinder with a diamter of $300\mu m$. It was scanned at a resolution of $0.7\mu m$ and a box-shaped subvolume of $240\mu m \times 240\mu m \times 420\mu m$ was extracted for the verification. The subvolume had 590 grains where 211 of these were interior grains. The average equivalent sphere grain radius was $17.8\mu m$ for the whole subvolume or $19.0\mu m$ for the interior grains.
The preprocessing steps for segmentation of the grains was the same as in section 3.5.

4.4.1.2 Results

Verification of seed point estimate The seed point estimate deduced in equation (4.3) was tested for it's validity. The test was simply done by comparing the Laguerre tessellation where the centers of mass were used and the Laguerre tessellation where the estimated seed point was used with the experimental grain structure. This showed that the Laguerre tessellation where the estimated seed point was used reproduced the experimental grain struc-

ture better in terms of the number of voxels assigned correctly. The Laguerre tessellations in the following are all produced using the estimated seed point.

Figures of merit To quantify how well the Laguerre tessellation describes the experimentally-measured grain structure compared to the Voronoi tessellation, a number of figures of merit was used. The figures of merit were divided in two groups: global descriptors and local descriptors. The global descriptors were:

- distribution of 3D grain size
- distribution of number of grain faces
- fraction of correctly assigned voxels

The 3D grain size distribution is a well known measure of similarity when studying grain structures as it can be inferred from 2D measurements and stereology. The distribution of the number of grain faces indicates how well the topology of the grain structure is reconstructed on a global scale. The fraction of correctly assigned voxels gives some information of how well the position of the Laguerre cells match the grains.
If studying the dynamics of a system (e.g. [49]), the neighborship of the grains on a more local scale is of interest. To quantify this, the following local descriptors were used:

- fraction of grains with all neighbors correct
- number of erroneously extra neighbors per grain
- number of erroneously missing neighbors per grain
- total number of wrong neighbors per grain

Error-free input The centers of mass and the grain volumes were computed from the experimentally-measured grain structure and used to compute the Laguerre tessellation. Figure 4.6 shows a comparison of a 2D slice of the experimentally-measured grain structure and the Laguerre tessellation. This first result shows that even though the Laguerre tessellation is simple, it still produces a grain map which by visual inspection is acceptable. Of course the non-planar faces cannot be reconstructed, but in general the grain size and position seems to be reconstructed well.
For the purpose of comparison, the centers of mass were also used to compute the regular Voronoi tessellation. 3D renderings of the experimental grain structure, the Laguerre tessellation and the Voronoi tessellation are shown in figure 4.7. Again it is clear that the non-planar faces cannot be reconstructed by the Laguerre or the Voronoi tessellations. Yet the 3D rendering indicates that the Laguerre tessellation is better at reconstructing the grain with the correct size compared to the Voronoi, which could be expected since this information is provided to the Laguerre and not the Voronoi. To do a more systematic comparison

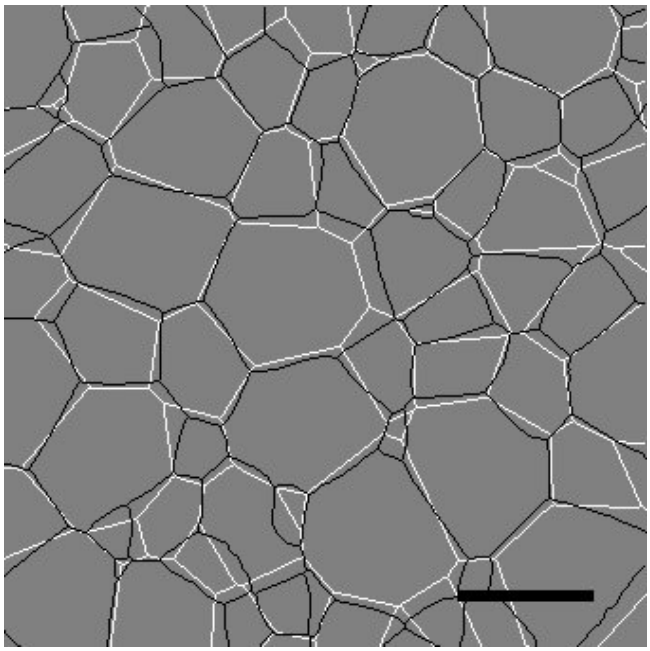

Figure 4.6: Comparison of a 2D slice of the experimentally-measured grain structure (black) and the Laguerre tessellation (white). The scale bar in the bottom-right corner correspond to 50 micrometers.

of the Laguerre and the Voronoi tessellations with the experimentally-measured grain structure, the figures of merit described above are used. Figure 4.8 shows the distribution of the normalized equivalent sphere radius, i.e. the equivalent sphere radius for each grain divided by the average equivalent sphere radius. The three distributions show that the Voronoi distribution is more peaked and more symmetric than the measured distribution, meaning the Voronoi had problems reconstructing the smaller and the larger grains in the data. The Laguerre distribution, on the other hand, is more similar to the measured one, indicating that it actually can reproduce the grain size distribution of the provided grain structure.

Table 4.1 shows that figures of merit for the Laguerre and Voronoi tessellations. From this it is clear that the Laguerre tessellation performs better than the Voronoi based on the figures of merit used here. In all figures of merit the Laguerre tessellation perform significantly better. The number of correctly assigned voxels goes from 59.72% for the Voronoi to 86.30% for Laguerre, which is expected since figure 4.8 showed that the Voronoi does have problems reconstructing small and large grains with the correct size. With respect to the local descriptors, where the neighborship is considered, the Laguerre tessellation is also superior to the Voronoi. Still, only 31.75% of the grains in the Laguerre tessellation have all the correct neighbors.

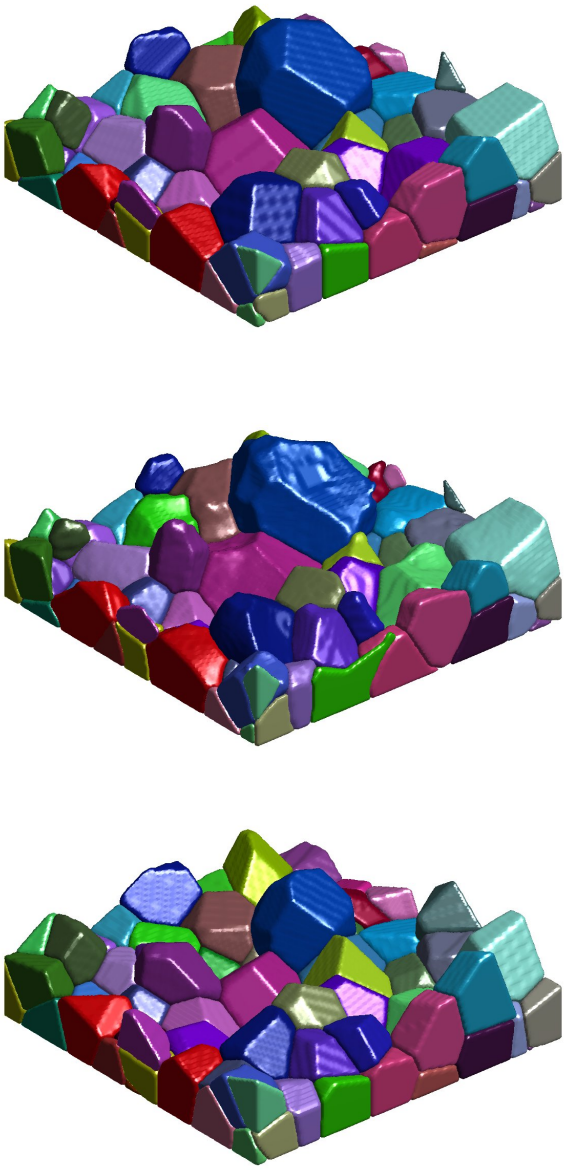

Figure 4.7: 3D rendering of the 3D Laguerre tessellation (top), the experimental 3D grain structure (middle) and the 3D Voronoi tessellation(bottom).

Figure 4.9 shows a histogram of how the number of wrong neighbors distribute

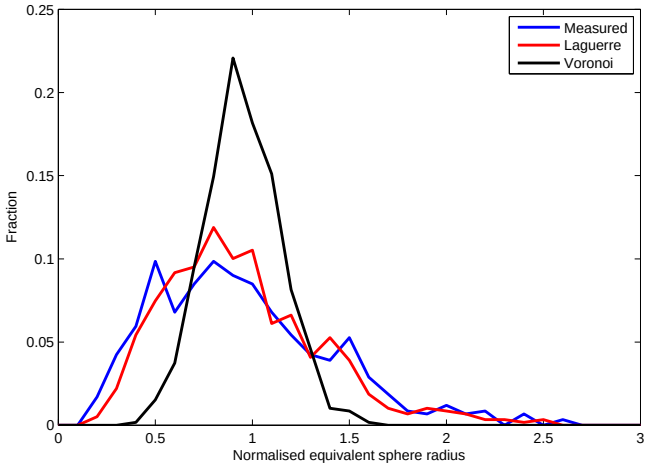

Figure 4.8: 3D grain size distribution in terms of the normalized equivalent sphere radius for the experimentally-measured grain structure (blue curve), the Laguerre tessellation (red curve) and the Voronoi tessellation (black curve).

	Voronoi	Laguerre
% correct voxels	59.72	86.30
% grains with all neighbors correct	7.82	31.75
# erroneously extra neighbors/grain	1.87	0.58
# erroneously missing neighbors/grain	1.29	0.64
# total number of wrong neighbors/grain	3.16	1.22

Table 4.1: Figures of merit for Laguerre and Voronoi tessellations.

for the Laguerre tessellation. Interestingly enough, grains with one wrong neighbor are the most frequent. This shows us that more than 65% of the grains have one or less wrong neighbors and more than 87% of the grains have two or less wrong neighbors. This number should of course be compared with the average number of grain faces per grain, see table 4.2. This table together with figure 4.10 also shows that the Laguerre tessellation again performs better than the Voronoi tessellation with respect to reconstructing the number of faces of the grains on a global scale. Looking further into this revealed that it is mainly small grains which have a high number of wrong neighbors. This fact also explains why it is possible to have an overall labeling which is good (86.30%) yet only 31.75% grains with all the correct neighbors.

Input with simulated errors To study the Laguerre tessellations robustness against measurement errors, a set of grain maps where the input was added with a simulated error term was made. Two types of errors are studied: Errors in the volume and errors in the center of mass. For the study of error in the volume

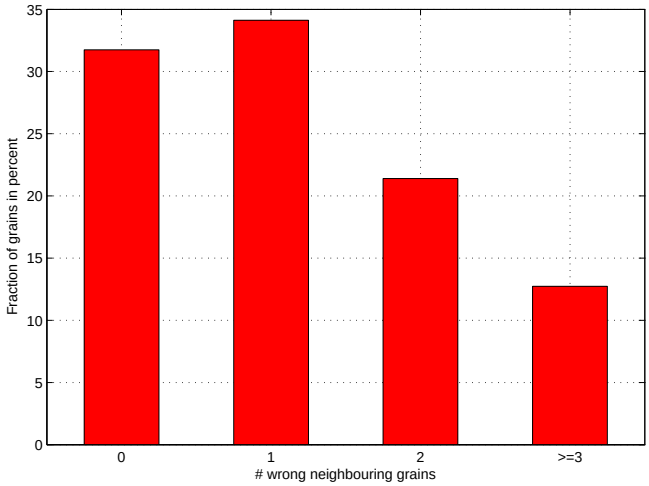

Figure 4.9: Distribution of # of wrong neighbors for the Laguerre tessellation.

	Average # of grain faces
Measured	10.98
Laguerre	10.93
Voronoi	11.56

Table 4.2: Average number of grain faces for the experimentally-measured, the Laguerre and the Voronoi tessellation.

$N = 17$ reconstructions were made with centers of mass without errors and deviations in the volume following a Gaussian distribution with a mean value $\mu = 1$ and standard deviation of $3\sigma = 0.1$, i.e. 99.7% of the simulated volume errors are within $\pm 10\%$. For the study of the errors in the center of mass $N = 17$ reconstructions were made with volumes without errors and errors in the center of mass in random directions but with a magnitude following a Gaussian distribution with a mean value $\mu = 0$ and standard deviation of $3\sigma = 2\mu m, 4\mu m, 7\mu m, 10\mu m$. As shown in table 4.3 the figures of merit decrease as the simulated errors are introduced. First, consider the simulations with errors in the volume. The average figures of merit are only slightly affected by adding an error in the volume. This is not a surprise as what matters to the size of the reconstructed Laguerre cell is not the volume directly but the cubic root of the volume.
For the errors added to the center of mass, the decrease in the average figure of merit is slightly higher. As the error increases, the percentage of voxels labeled correctly goes from 85.88% for $2\mu m$ to 78.25% for $10\mu m$. For the percentage of grains with all neighbors correct, the result is worse. Going from 28.80% $2\mu m$ to 10.15% for $10\mu m$, it is clear that the grain neighborship is no longer robust towards errors in the center of mass as it gets close to $10\mu m$. The same pattern

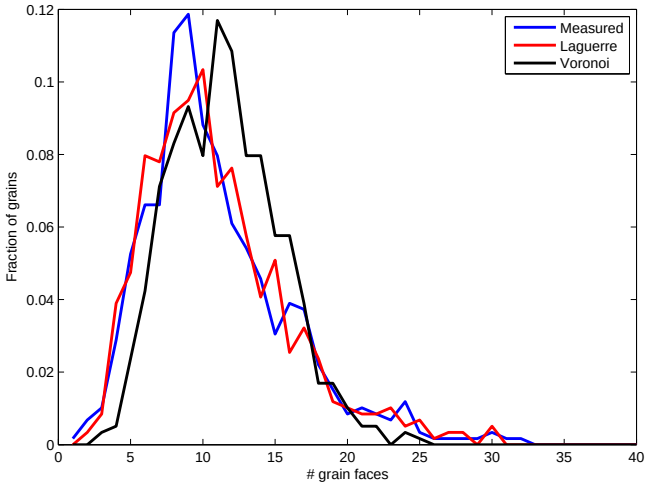

Figure 4.10: Grain face distribution for the experimentally-measured grain structure (blue curve), the Laguerre tessellation (red curve) and the Voronoi tessellation (black curve).

	Voronoi	Laguerre					
Error type	None	None	Volume	Center of mass			
St.dev. of error, 3σ	-	-	10%	2 μm	4 μm	7 μm	10 μm
% correct voxels	59.72	86.30	86.26	85.88	84.72	81.85	78.25
% grains with all neighbors correct	7.82	31.75	30.90	28.80	23.82	16.99	10.15
# erroneously extra neighbors/grain	1.87	0.58	0.59	0.62	0.73	0.93	1.23
# erroneously missing neighbors/grain	1.29	0.64	0.65	0.69	0.76	0.96	1.24
# total number of wrong neighbors/grain	3.16	1.22	1.24	1.31	1.49	1.89	2.47

Table 4.3: Average figures of merit for the Laguerre tessellation with simulated errors. All error simulations are repeated $N = 17$ times. The Voronoi and Laguerre tessellations without errors are repeated for comparison.

is seen if the number of erroneously assigned neighbors is considered. Here, the average figure of merit is almost doubled going from $2\mu m$ to $10\mu m$. Note that none of the average figures of merit is worse than the one for the grain map

based on the Voronoi tessellation.

4.4.1.3 Discussion

The results stated above clearly show that the Laguerre tessellation is a better choice compared to a Voronoi tessellation when looking for a simple model to represent a well-annealed grain structure. One reason for the better performance is of course the fact that the Laguerre tessellation is given more information than the Voronoi through the weight parameter which scales with the measured grain volume. But most of today's experimental techniques are capable of producing some kind of estimate of the grain volume, hence this information is already at hand.
The voxelized implementation of the Laguerre tessellation gives some limitations with respect to precision. The precision is determined by the chosen voxel size, the smaller the better precision. But with a small voxel size comes a higher number of computations, meaning the software gets slower. One way to overcome this problem would have been to compute the Laguerre cells using a geometry library such as CGAL(`http://www.cgal.org/`) and use this for the voxelization. This way volume and center of mass could be computed with high precision from the analytical solution without increasing the computation time and a voxelization of this could still be used for comparison to experimentally-measured grain structures. The use of CGAL was, however, skipped in this study due to time constraints.
As the Laguerre tessellation only can reconstruct 31.75% of the grains with all the correct neighbors in the case where the input is error-free, it is not an appropriate tool for studies where a precise knowledge of the topology is of high interest. With the additional information that the Boxscan technique provides in terms of profiles it may be possible to improve the figures of merit for the local topology. Information of the profiles could give access to the moments of the individual grains, which could be put into Laguerre formulation by letting the axes of the moments define a new coordinate system for each cell such that the underlying grid of the tessellation no longer would be isotropic.
A way to do this could be to use the Laguerre model in context with a Monte Carlo optimization scheme using the centers of mass and the volumes as the targets of the optimization. For this to be useful in practice, a fast method for computing Laguerre tessellations would be needed. Such a method could also be extended to also use the moments or the profiles as targets for potentially better reconstructions.

4.4.1.4 Summary

In the above, a comparison was made between using the Laguerre tessellation and the Voronoi tessellation for reconstructing grain maps of an experimentally-measured grain structure. The effect of measurement errors was studied for errors in the order of magnitude of today's state-of-the-art synchrotron-based measurement techniques. All these results talk in favor of using the Laguerre

tessellation for generating grain maps rather than using the Voronoi tessellation. Even in the presence of measurement errors, the Laguerre tessellation preserves both the local and the global characteristics more accurately than the Voronoi tessellation.

4.4.2 Algebraic reconstruction technique

To verify that it is possible to reconstruct the 3D shape of a grain from Boxscan data using ART, the implementation was used on real experimental data.
The study of the reconstruction of the 3D shape of a single grain, opened up a number of questions regarding which parameters influence the quality of the reconstruction. These parameters are further explored in a small simulation study.

4.4.2.1 Application to single grain

For the verification, a grain with a high completeness in the D15 sample (the sample used to verify the Boxscan technique as described in 3.5) was chosen. A neighborhood of 25^3 voxels with a size of 2 micrometers was setup around the grain's CMS position. The grain radius was 17.3 micrometers so it was expected to be fully contained within the neighborhood. The profiles belonging to the grain were extracted from the database and filled into $\mathbf{b}$ and A as described in 4.2.2. The resulting linear system had $n = 25^3 = 15625$ and $m = 931$, i.e. an under-determined system. The result of applying the ART implementation is shown below.
For verification, the same grain was taken out of the phase contrast tomography verification dataset. The verification grain was translated and rotated according to the values found from the ICP in 3.5.3 and resampled to a voxel size of 2 micrometers such that it could be compared directly with the ART solution.

4.4.2.2 Results from single grain

The ART implementation was run with a relaxation of $\lambda = 10^{-5}$ and terminated when the change in the figure of merit was less than $f_b = 10^{-4}$. Figure 4.11 shows the evolution of the figure of merit for the ART computations as the iteration number k progresses. Note that the value of the figure of merit is more than 0.60. This is due to the fact that it is experimental data containing noise in the linear system. In real experimental data, noise will inevitably be present, which is why a relaxation parameter λ is included in equation (4.4).
In figure 4.12 the solution from ART is compared to the verification grain. The detail level of the ART solution is much less than the verification grain and it looks much more rounded and smooth. Yet the overall shape of the ART solution seems acceptable. The same conclusions can be drawn from figure 4.13 where the same layer of the two grains have been overlayed. Comparing voxel to voxel, the ART solution overlaps 87% with the verification grain in the whole volume.

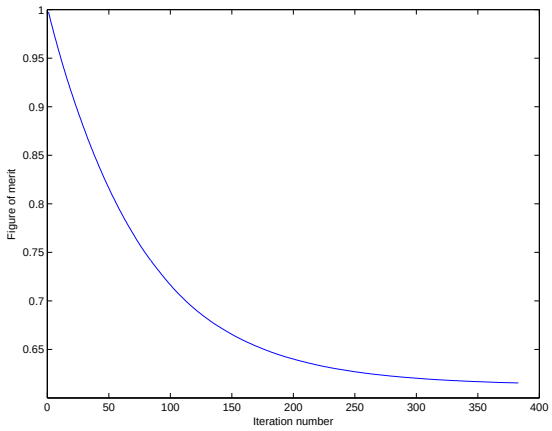

Figure 4.11: Evolution of the figure of merit for the ART computations as the iteration number k progresses.

Another way to quantify the difference between the two grains is to measure the distance from the grain boundaries of the verification grain to the ART solution. In figure 4.14, this distance have been computed and mapped onto the surface of the verification grain. From this it is again clear that the ART solution has been smoothed out and does not manage to reconstruct the corners of the grain correctly. The distance between the two boundaries varies between 0 and 5.8 micrometers with and average of 2.7 micrometers.

4.4.2.3 Discussion on reconstruction of a single grain

In the previous, it has just been seen that it is possible to reconstruct the 3D shape of a grain from Boxscan data with a precision on the position of the grain boundary less than the step sizes in the Boxscan experiment. Yet keep in mind that the Laguerre tessellation is capable of reconstructing 86% of the voxels correctly which is similar to the ART result of 87%. The difference between the Laguerre tessellation and the ART approach is that the Laguerre incorporates information on the neighborship but no information from the profiles where as the ART approach directly uses the profiles but neglects the neighborship. Thus, extending the ART implementation to simultaneously solve for all grains within a neighborhood may improve the result even further. Another way would be to apply a Monte Carlo optimization scheme [70, 71] where the solution to the whole voxelized sample is found by random walk.
Using a compound system as presented in [57] in combination with a method similar to DART [72] may be a faster alternative to the normally slower Monte Carlo method. The key point is that grains are discrete near-convex objects, hence the voxels in the center of the grain are less likely to change compared to those on the edge of the grain. So focusing the computations to the edge of the grains as it is done with DART may lead to faster results.

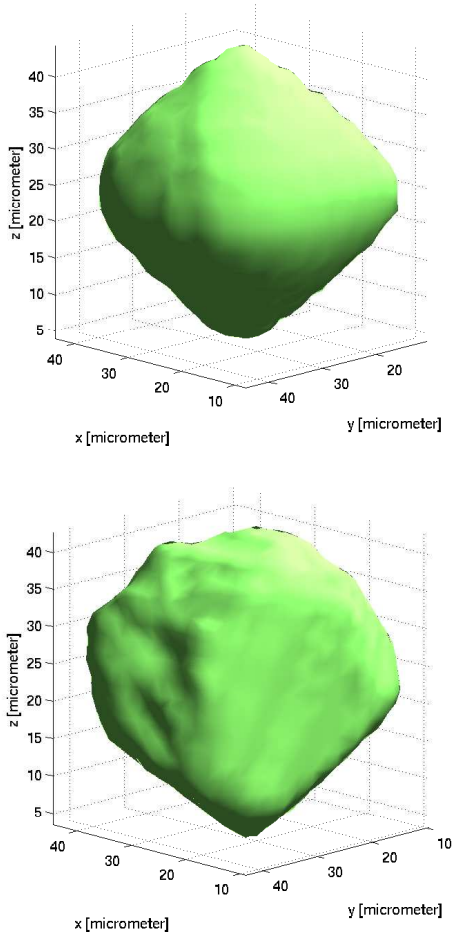

Figure 4.12: Top: Grain as reconstructed by ART using the Boxscan data. Bottom: The phase contrast tomography verification grain.

On the experimental side, decreasing the step sizes δ_y and δ_z or extending the ω-interval to add more profiles may be an easier way to improve the result. To identify how the reconstruction result is influenced by these parameters, the following summarizes the main results of such a small study.

4.4.2.4 Parameter study

Various parameters affect the quality of the reconstruction in different ways. To get an idea of what way they affect the reconstruction, a small study with simulated data was conducted.
To generate the Boxscan data, a grain extracted from the D15 dataset was used

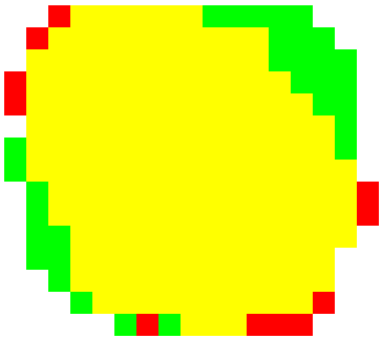

Figure 4.13: The same layer from the ART solution (green), verification grain (red) and their overlap (yellow). The voxel size is 2 micrometers.

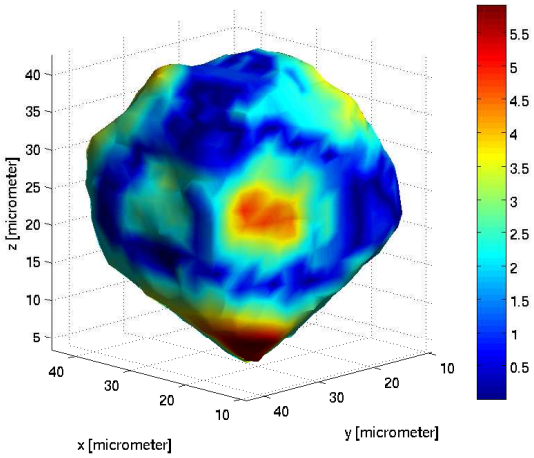

Figure 4.14: The distance between the grain boundaries of the ART reconstruction and the verification grain mapped onto the surface of the verification grain. The color scale is in units of micrometers.

and resampled to $43 \times 38 \times 33$ voxels. A piece of simulator software was developed to compute the Boxscan profile based on the input parameters: number of beams and their internal angle, beam width, ω-interval and step sizes δ_y and δ_z. The experimental geometry of the simulation was the standard one used for Boxscan,

i.e. a rotation-stage placed on top of the translation-stages, except that beams could be rotated at any angle with respect to the xy-plane and not just 0 and 90. The extra freedom on the beam angle was introduced to be able to simulate the presence of an Euler cradle. An Euler cradle can rotate the sample to have any orientation in 4π, i.e. it is a generalization of the rotation of the ω-stage.
No noise was introduced in the system as this was not a test of the ability of ART to reconstruct shapes, but more a study of the influence of parameters. It should be mentioned that the results will not be treated quantitatively, but rather from a more qualitative point-of-view.
All reconstructions in ART were done with $\lambda = 0.5$, $f_a = 10^{-6}$ and $f_c = 200$. Since no noise was introduced into the system, repetitions of the reconstructions were not done as preliminary results showed that the reconstruction did not change significantly when reconstructed with the same set of parameters. The only randomness in the reconstructions was the choice of rows in the A-matrix. But as each row was visited multiple times for each reconstruction, the effect of this randomness is minimized.
To quantify the reconstruction error, a figure of merit $\text{fom}_2 = \sum |x^* - (x_{ART} > 1/2)| / \sum |x^*|$ was used, where x^* is the true solution (which is known) and x_{ART} is the solution found using ART. The threshold of $1/2$ was fixed, as the system was normalized such that all voxels would have have values in the range 0 to 1.

4.4.2.5 Results of the parameter study

Effect of beam angle with 3 beams In the original principle of the Boxscan only two beam configurations or scans were conducted. With today's equipment it is possible to mount the ω-stage in an Euler cradle so the ω-axis can be tilted to point in any direction. For now, consider the case where the sample is rotated around the x-axis in the Euler cradle. Fixing the beam to be horizontal, it is possible to obtain the beam configurations (vertical and horizontal) of the original principle by rotating the sample 0 and -90 degrees in the Euler cradle. With this setup, it is easy to scan the sample with another beam configuration with a rotation between -90 and 0 degrees. The idea behind having an extra beam between the two others is that this will combine information from both the vertical and the horizontal directions. The goal is to see if there is an optimal angle to which the the third beam should be tilted to give the best reconstructions.
The Boxscan data was simulated with a step size of 5 voxels, a beam width of 5 voxels (ie.e no overlap from step to step) and an ω-interval $= [-90, 90]$ with a $\Delta\omega = 5$ for a beam tilt from -85 to -5 in steps of 5 degrees.
In figure 4.15 the results of the reconstructions are shown. Surprisingly there are two minima in the plot, one around -70 and one around -35. One would think the minimum would be around 45 degrees as this would be the position which would combine the most information from both the vertical and horizontal directions. But still, the plot shows that the closer the third beam is to one of the other beams, the higher the reconstruction error. As only one grain was tested, it is possible that the geometric properties of the grain have an influence.

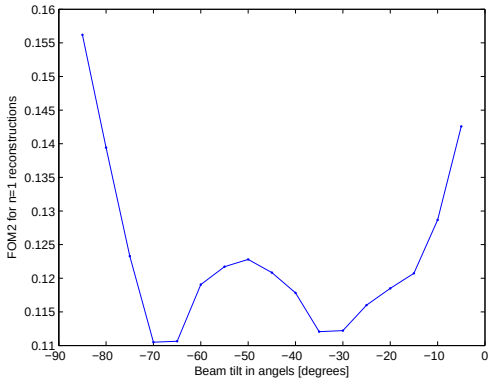

Figure 4.15: Reconstruction error fom_2 as a function of the beam angle of the third beam.

Effect of the number of beams As seen above, the reconstruction error decreased when more information was available from a different direction than the two in the original Boxscan principle. Naturally, the next question would be how much could be gained by adding more beams to the reconstruction. The experimental setup is the similar to the one above with 3 beams, but instead of fixing two of the beams at -90 and 0, they are spread out over a 180 degrees interval. The number of beams k is varied from 2 to 8 and the reconstruction error is measured. The angles of the k beams are $-90 + i\frac{180}{k+1} \quad i = 1 \ldots k$. Figure 4.16 shows the reconstruction error fom_2 as a function of the number of beams k. As expected, the reconstruction error decreases as k increases. Furthermore, the highest decrease is for lower k, especially from 2 to 3 where the error is halved.

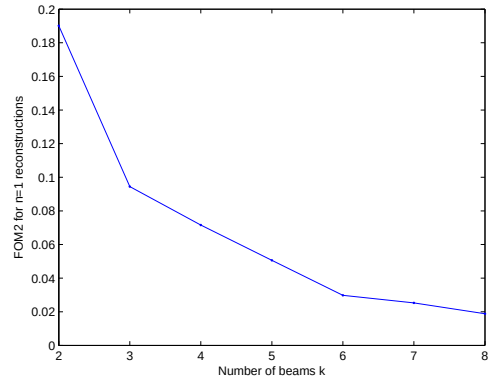

Figure 4.16: Reconstruction error fom_2 as a function of the number of beams.

Effect of the width of ω-interval The above simulations have been done with rather large ω-interval of 180 degrees. Normally, a smaller interval would be scanned, but still with perpendicular directions. The following study is of the dependence on the width of the ω-interval. The parameters are the same as before except the number of beams is set to $k = 5$ with their angles chosen as in the previous study. The ω-interval is split into two perpendicular ones, each with 15 points: $\pm 45 + [-5i, 5i] \quad i = 1 \ldots 6.$, i.e. $\pm 45 + [-5, 5]$ for $i = 1$ (in total 20 degrees) and $\pm 45 + [-30, 30]$ for $i = 6$ (in total 120 degrees). Since the number of points in each interval is the same, the amount of data is constant.
Figure 4.17 shows the reconstruction error as the ω-interval is increased. A decrease in error is seen as the width increases. This is what could be expected as the amount of information from different directions increases with the width of the ω-interval. This can be compared to the situation with the angle of the third beam as studied above. When only information from a few directions exists, the error is higher.

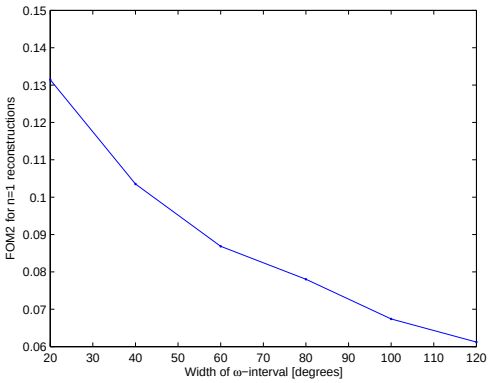

Figure 4.17: Reconstruction error fom_2 as a function of the width of the ω-interval.

Effect of the step size δ One of the parameters which is rather easy to change in a Boxscan experiment compared to some of the above is the step size δ. To test if it is possible to gain significantly better ART reconstructions by changing the step size, a simulation is conducted where the step size is changed from 4 to 20 in steps of 2 voxel size lengths. The beam width is adjusted correspondingly such that there is no gap or overlap between the illuminated volumes. What are used is 5 beams spread out equally over a -90 to 90 degrees interval and a ω-interval [-90:5:90].
Figure 4.18 shows no significant change in the reconstruction error as a function of the step size. From a mathematical point-of-view, this is no surprise as the information content for each of the step sizes should be the same. The only difference is that the information is kept in a more and more integrated form

the as the step size increases.

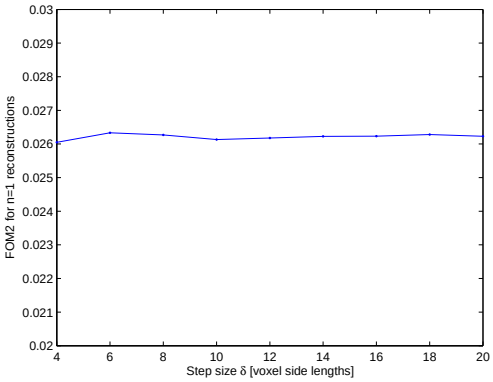

Figure 4.18: Reconstruction error fom_2 as a function of the step size δ.

Effect of the beam width Following the simulation of the step size effect, it is interesting to study how the width of the beam influences the reconstructions. It does not make sense to introduce gaps between the illuminated volumes but the effect of overlap between successive illuminated volumes can be studied.
Again, 5 beams equally spread out over the -90 to 90 interval are used and the ω-interval is set to [-90:5:90]. A fixed step size of $\delta = 5$ is used while the beam width is varied from 5 to 30 in steps of 5 voxel side lengths.
Figure 4.19 shows a similar result as before. The reconstruction error does not significantly change as a function of the overlap. The explanation for seeing this must be similar to the one above, namely that the information content is the same but it just gets more and more redundant as the overlap between gets bigger with the beam width.

4.4.2.6 Parameter study discussion and conclusion

Based on the above results, it is possible to give some guidelines where to tune which parameter to get better 3D ART reconstructions from Boxscan data. Even though the above results are not perfect in the sense that they do not go into deep details of the results, they should still be seen as valid guidelines.
The conclusions seem to be that it is more important to get as much data as possible from as many directions as possible, than to get finely sampled data from just a few directions. In other words, use as many beams as possible and the larger ω-interval as possible rather than a small step size. From an experimental points-of-view this is bad news, as it is more difficult to use many directions than to make the step size small.
A more in depth parameter study would use more than one 3D object to study the parameters. Furthermore, it could be argued that the large ω-interval used

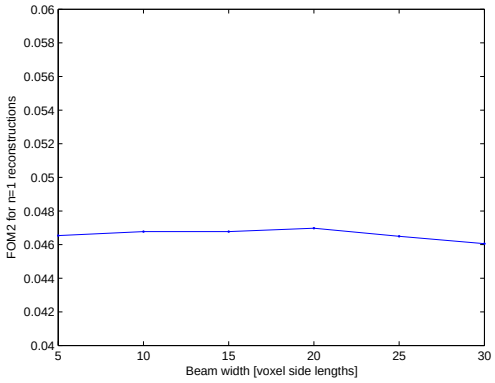

Figure 4.19: Reconstruction error fom_2 as a function of the beam width.

in the study of the step size and the beam width has an influence on the effect of the reconstructions. The point here is that the if the system is already highly overdetermined because of the large ω-interval, changes in the step size and the beam width may not be measured.

4.4.3 Linear programming

To verify that the linear programming technique described in section 4.3 works on real data it was applied to a set of six 3D shapes. Furthermore, the six shapes were also used in the study of the minimum number of required projections needed to reconstruct a 3D shape.

4.4.3.1 Data

The data used in this study were simulated data on six 3D shapes: three convex shapes and three grains from a real dataset (almost convex shapes), see e.g. figure 4.20. The three convex shapes were all of a size $19 \times 19 \times 19$ and the three grains were subsampled to have a size $26 \times 20 \times 22$, $22 \times 24 \times 21$ and $21 \times 20 \times 20$, respectively.
The step size used in the projection of the data was $\delta_t = 0.5$ of voxel side length. The step size used is a trade off between the size of the A-matrix on the one hand and on the other hand how finely sampled the double integral of the shape is. The smaller the step size δ_t, the more points a projection will contain and the more it will resemble the double integral of the shape. If the step size is very small, then the A-matrix will become very large and it will be time consuming to solve the linear system. A good value of the step size is found to be $\delta_t = 0.5$ as it is both smaller than the voxel side length such that each voxel is subsampled and it keeps the size of the A-matrices on a scale where they can be solved in a reasonable time.

The precision of numbers fed into CPLEX was set to 8 decimal points and no noise was added to the system as the goal is to find the minimum number of projections needed under noiseless conditions.

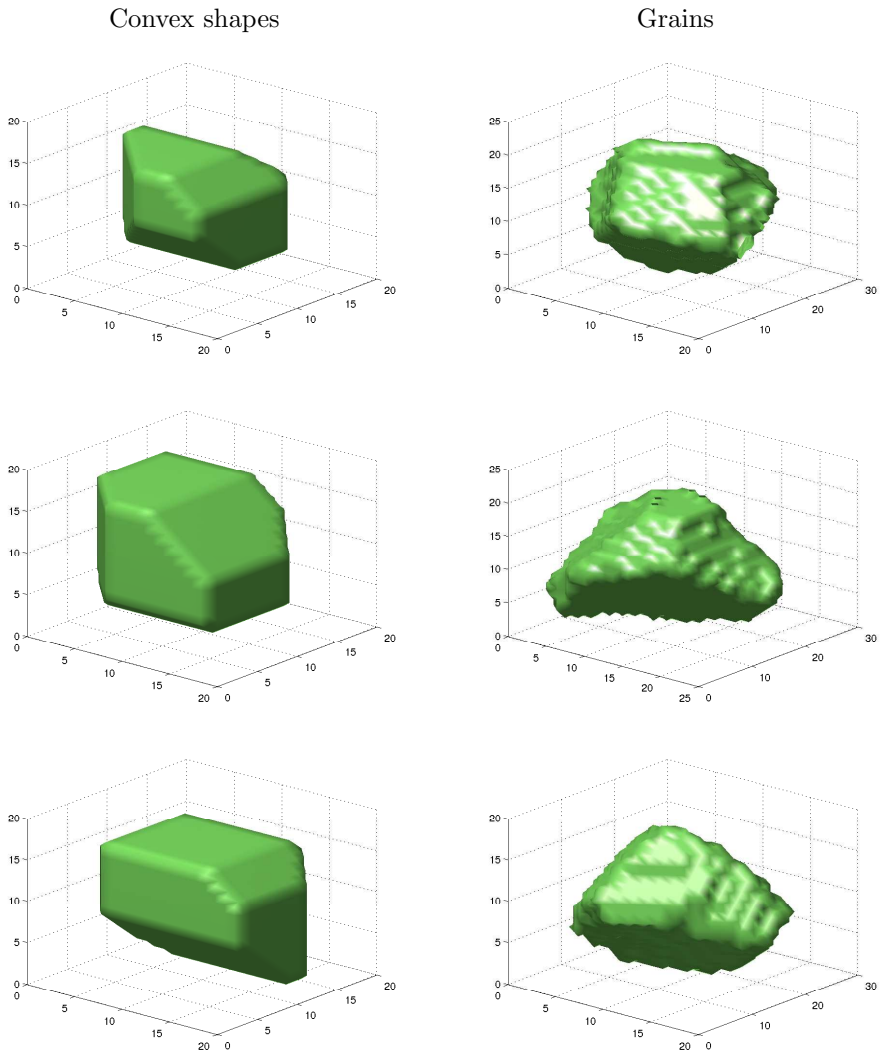

Figure 4.20: Left column, top to bottom: Convex shapes 1 to 3. Right column, top to bottom: Subsampled grain shapes 1 to 3.

4.4.3.2 Application of CPLEX to data

For each of the six shapes, a number of projections, p, were computed from random directions in 4π to construct A and $\mathbf{b}$. To get sufficient statistics, 100

sets of random projections were computed for each number of projections p for each of the six shapes.
A solution to the linear systems was found using CPLEX and furthermore a search for an alternative solution $\mathbf{x}_a$ was also done by using the objective function $f = \mathbf{x}_a^T \mathbf{x}_k$.

4.4.3.3 Results

The results of performing reconstructions using linear programming are presented in three parts: average reconstruction error, number of perfect reconstructions and number of alternative reconstructions.

Average reconstruction error The average norm of the reconstruction errors for the six shapes are plotted in figures 4.21. As expected the error drops towards zero as more projections are used for the reconstruction. The error is not equal to zero, but is in the order of 10^{-6} which is what can be expected from the software when finite precision numbers are used as input.
The number of projections which is needed before the error drops is between 10 and 14. The convex shapes need less projections than the grains before the error drops. This is not a surprise as the grains are not perfectly convex and should therefore be more difficult to reconstruct.
The standard deviation of the error with respect to p seems to be constant for all six shapes until the error drops towards zero. Interestingly enough all six plots show a kink in the plot around $p = 6$ and $p = 7$. As mentioned above, 7 random projections are the minimum number needed in the case of a 2D shape. Whether there is a link between this observation and the theoretical work mentioned above is not possible to tell and more theoretical mathematical work would be needed to prove this.

Number of perfect reconstructions The number of perfect reconstructions for the six shapes are plotted in figure 4.22. A reconstruction is defined as perfect when it is thresholded at 0.5 and then matches perfectly with the true binary solution. The information contained in them is basically the same as figure 4.21 except that the thresholding is introduced.
In the figure, it is seen that between 10 and 13 projections are needed for all 100 reconstructions to be perfect. The reason why it is 13 and not 14 as above could be an effect of the thresholding. A few errors in the reconstruction may cause a larger average error but the values may still be closer to their correct values such that the thresholding restores the reconstruction errors.
Again a kink on the plots around $p = 6$ and $p = 7$ is observed.

Number of alternative reconstructions CPLEX reported that an optimal solution was found for each of the searches of an alternative solution $\mathbf{x}_a$. But it also turned out that there was a difference between $\mathsf{A}\mathsf{x}_a$ and $\mathbf{b}$. Ideally, this situation should not be able to happen, as a solution found by CPLEX should

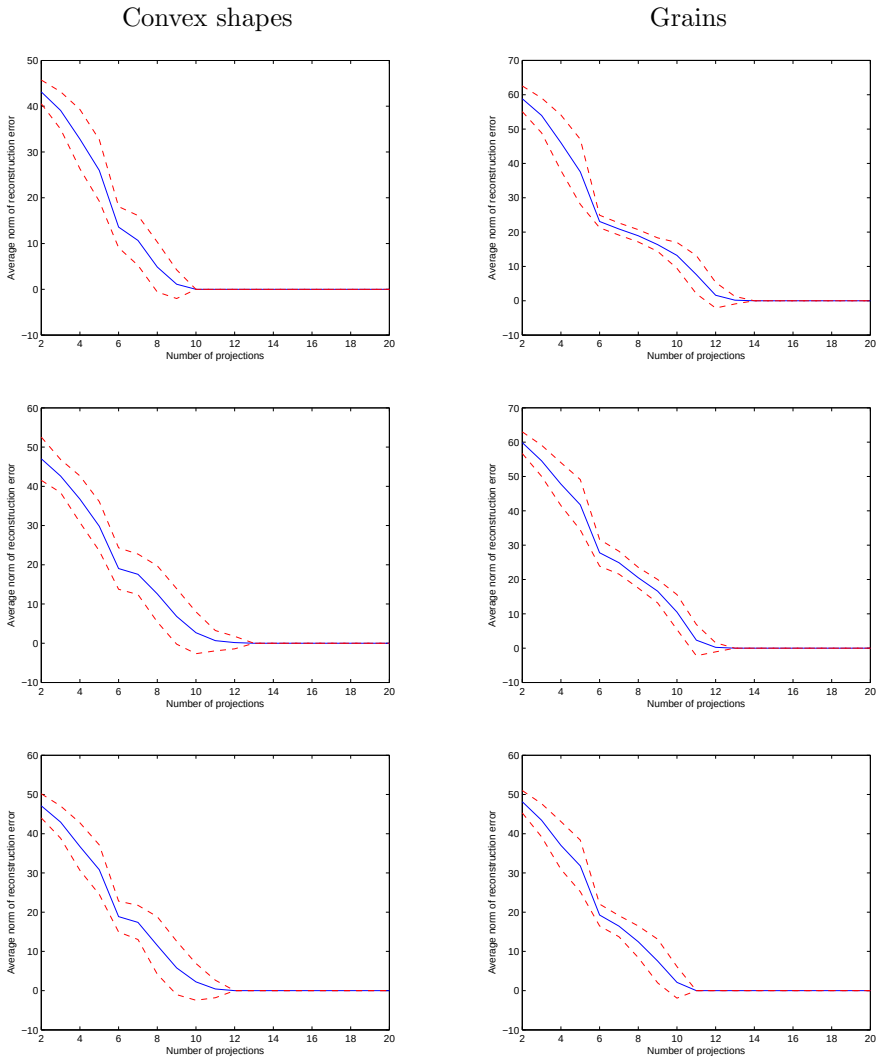

Figure 4.21: Left column, top to bottom: Average of the norm of the reconstruction error for convex shapes 1 to 3. Right column, top to bottom: Average of the norm of the reconstruction error for grain shapes 1 to 3. Red dashed lines are standard deviation.

solve the linear system $\mathsf{A}\mathsf{x}_a = \mathsf{b}$.
A possible explanation to this, is the finite numerical precision of the input data. The input to CPLEX is several hundred, maybe even more than one thousand, constraints which are dependent. Furthermore, to search for an alternative solution, an objective function is added which forces CPLEX to search for a solution far away from the original solution to the linear system. The combination of the

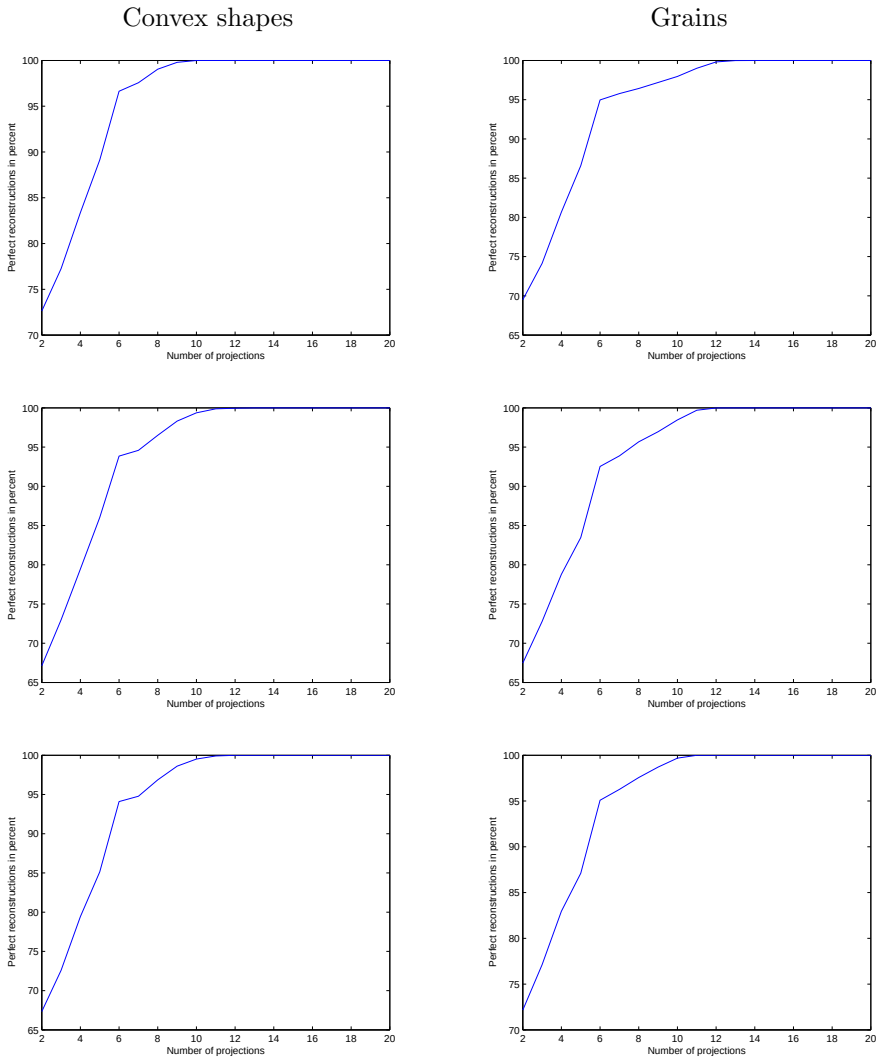

Figure 4.22: Left column, top to bottom: Percent perfect reconstructions for convex shapes 1 to 3. Right column, top to bottom: Percent perfect reconstructions for grain shapes 1 to 3. Note that the range on the y-axis is not the same for all plots.

objective function and the finite numerical precision on the constraints could be the reason why CPLEX cannot find any real alternative solutions.
This does not show that alternative solutions do not exists but only that a higher precision may be needed and that linear programming may not be the best way to search for alternative solutions in this type of linear systems.

Discussion and conclusion In this section it has been shown on a set of six 3D shapes that it is possible to reconstruct 3D shapes from Boxscan data and linear programming. The results show that between 10 and 14 noiseless projections are needed to perfectly reconstruct the 3D shape of convex and nearly convex shapes.
Furthermore, a search for alternative solutions to the linear systems was done, but did not succeed due to software problems.

The problems with the software suggests that instead of using linear programming to search for a solution to the binary systems, an alternative such as binary integer programming should be used. The advantage of using binary integer programming is that it produces a solution which is binary and not only limited to the interval $[0; 1]$. The disadvantage is that binary integer problems are hard to solve and it may be necessary to do an exhaustive search[73].

The way that the linear systems are constructed, actually conflicts with the concept of inverse crime. The problem is that the data and the model are constructed using the same algorithms. A way to have avoided this would be to use different voxel size when constructiong the model and the data[74].

Chapter 5

Application of the Boxscan technique

5.1 Full volume scan of a β-titanium alloy

5.1.1 Introduction

Until now, the Boxscan principle has only been demonstrated on a subvolume of a sample. To study bulk properties of materials large samples with large numbers of grains in the cross-section, i.e. large number of grains not influenced by the surface of the samples, are needed, e.g. when grain rotations during plastic deformation are studied. When a sample is plastically deformed, the individual grains deform by changing their shape and rotating their lattice[75, 76]. Various models for how the grains rotate have been developed through the years[77, 78], but none of them have been able to predict how a specific grain will actually rotate under given conditions. The development and verification of models have also suffered under the lack of true 3 dimensional experimental data. The combination of orientation information and spatial information of individual grains in the bulk enables the possibility to study how the grains rotate during plastic deformation with respect to the local conditions.

In a collaboration with Professor Matthew Miller from Sibley School of Mechanical and Aerospace Engineering at Cornell University, Ithaca, USA and Ulrich Lienert at the Advanced Photon Source at Argonne National Laboratory, Chicago, USA, the goal has been to apply the Boxscan technique to large samples in order to study grain rotations during plastic deformation. The study consists of two parts. In the first part, the grain structure of a sample is determined in the undeformed state. From this, the local conditions for each grain in the volume of interest can be found. In this case, the local conditions will be the neighboring grain sizes, positions and orientations. In the second part, the sample is deformed plastically and the rotations of the individual grains in the

volume of interest is measured.
Based on the knowledge of the grains' local conditions and how they rotated during deformation, it may be possible to develop new models for prediction of grain rotations. To get enough data and to minimize the effect of the sample surface, it is necessary to use a large sample with many grains. In the following, the first part of the study, is carried out by applying the Boxscan technique.

5.1.2 Experimental

5.1.2.1 Sample

The sample used for this experiment was shaped as "dog bone" with a region in the middle with a rectangular cross section of 700×700 micrometers. The material was the same type as the verification sample for the Boxscan technique was made of, i.e. meta-stable β-titanium alloy (Ti-β-21S), see section 3.5. The sample was well-annealed giving grains that were almost perfect crystals. The average grain size was said to be approximately 50 micrometers which approximately corresponds to 200 grains in the cross-section of the sample.

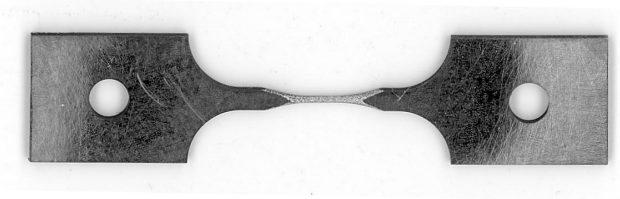

Figure 5.1: Sample shaped as "dog bone" similar to the one used in this experiment except this one has a circular cross section. Total length of the "dog bone" is approximately 5 cm.

5.1.2.2 Boxscan experiment

The experiment was conducted at the Advanced Photon Source (APS) at Argonne National Laboratory, Chicago, USA. The sample was mounted in an experimental setup similar to the one described in section 3.1. The X-ray beam had an energy of E=80.76 keV allowing for three rings to be imaged on the 2048×2048 pixel GE-detector. The size of the beam was 20 micrometers in both the vertical and horizontal cases and the step size was also the same in both cases $\delta_y = \delta_z = 5$ micrometers. The ω-interval was set to $[-60; 60]$ degrees in steps if 0.25 degrees.

5.1.2.3 Measured data

The image data was measured in stacks of 241 images, i.e. an image for each position in the ω-interval. The full dataset consisted of 111 image stacks (i.e.

550 micrometers) for the vertical z-scan and 230 image stacks (i.e. 1145 micrometers) for the horizontal y-scan. As the sample geometry was box-shaped with a square cross-section and not cylindrical, it was necessary to scan more than $700\sqrt{(}2)$ micrometers in the horizontal y-scan to ensure that the whole sample was illuminated for all ω-rotations. Each image stack took around 2 minutes to measure, meaning that the total acquisition time for the full volume was around 12 hours. Limiting the ω-interval would of course have reduced the acquisition time.

5.1.2.4 Data analysis

The analysis of the measured Boxscan data was performed as described in 3.4.2. The most important parameters used for the data analysis are given in table 5.1.

Parameter	Value
δ_η, spots to reflections	0.25 degrees
δ_η, reflections to profiles	0.25 degrees
δ_ω, reflections to profiles	0.25 degrees
Min. profile width	25 μm
δ_η, profile matching	0.25 degrees
δ_ω, profile matching	0.25 degrees
δ_z, profile matching	1 μm
$(\Delta_x, \Delta_y, \Delta_z, \Delta_{rod}, \Delta_{rod}, \Delta_{rod})$, 6D search	$(5\mu m, 5\mu m, 5\mu m, 0.01, 0.01, 0.01)$
Min. completeness	0.60

Table 5.1: Parameters for the data analysis.

As the ω-interval is rather large, the number of intersections in 6D rapidly grows large. Therefore, the height of the subset of matches M_S used for indexing was limited to $\delta_z = 1$ micrometer. Indexing with a larger δ_z had shown that the standard deviation of the position in z was less than 1 micrometer for the grains found meaning that grains would not be lost by setting $\delta_z = 1$ micrometer.

5.1.3 Results

5.1.3.1 Grain centers and grain sizes

In the full volume 1588 grains were found. To avoid the effect of truncated grains in the end of the vertical scanning interval, grains closer than 1.5 grain diameters (75 micrometers) to the edge of the interval were removed. This gave 1265 grains inside a volume of size $700 \times 700 \times 400$ micrometers. The grains were uniformly distributed in the cross section of the volume, see figure 5.2, which supported the idea that the whole cross-section of the sample had been illuminated during the experiment.
The measured grain size distribution can be seen in figure 5.3. This shows a peak around 50 micrometer as was expected from what was given about the

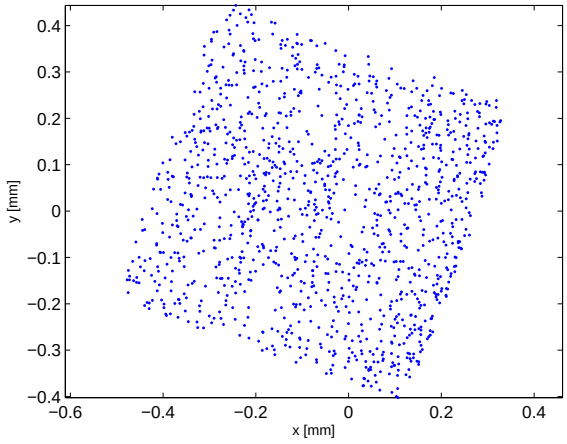

Figure 5.2: Cross-sectional view of the sample. All grain centers found in the volume projected onto the xy-plane clearly shows the rectangular cross section of the sample.

average grain size. The shape of the measured grain size distribution is very similar to a log-normal distribution. Estimating the log-normal distribution and superimposing it on the measured distribution, shows that the similarity between the theoretical and the measured distribution of the grain size is high.

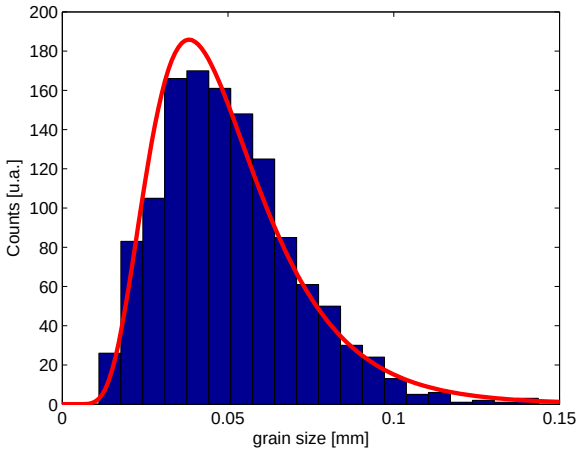

Figure 5.3: Grain size distribution in the sample.

5.1.3.2 Grain map from Laguerre tessellation

The measured grain centers and the grain sizes were used as input to a Laguerre tesselation, see section 4.1. This produced a grain map of the sample (figure 5.4) which could be used in further analysis of the sample. The Laguerre tessellation has it's limitations, but it is still a rather good representation of the true underlying grain structure and it enables the possibility to find the grain neighborship which is not possible by only looking at the grain centers and grain size. Even

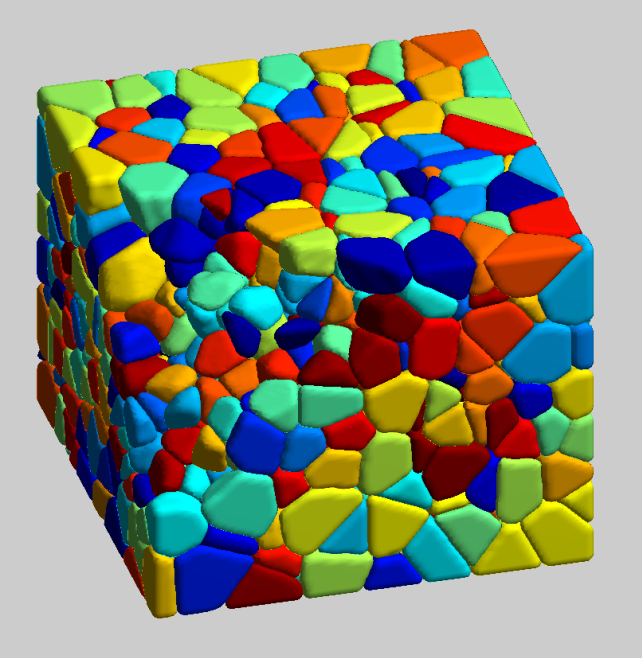

Figure 5.4: Grain map produced by a Laguerre tesselation. Some of the grains have been removed to reveal subsurface grains of the sample.

though it is not possible to verify the computed Laguerre tessellation with the true grain structure of the sample, it is still possible to verify the Laguerre tessellation against the measured values. Figure 5.5 shows the measured grain size distribution plotted against the grain size distribution of the Laguerre tessellation. Note that the bin size used for computing the distributions is not equal to the bin size of figure 5.3 and hence the number of counts for the measured grain size distribution is not the same in the two plots. As figure 5.5 shows, the grain size distribution of the measurements and the Laguerre tessellation are very similar supporting the idea that the Laguerre tessellation is a good representation of the underlying grain structure. The higher peak around 0.05 millimeter for the Laguerre grain size distribution indicates that the Laguerre tessellation slightly favors medium sized grains over larger grains.

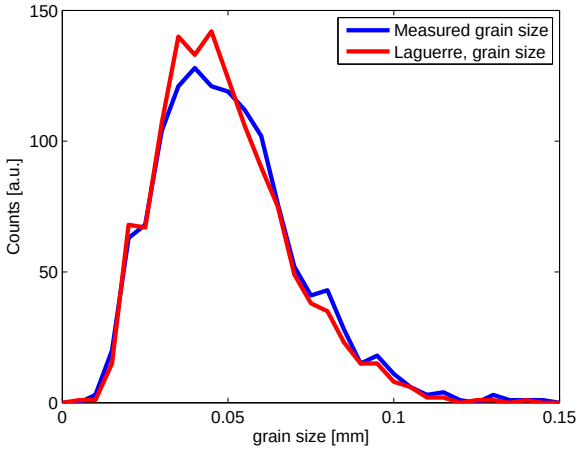

Figure 5.5: Comparison of grain size distribution between the measured grain size and the grain size produced by the Laguerre tesselation.

5.2 Discussion and conclusion

The above results show that it was possible to successfully apply the Boxscan technique to large volumes. The measured grain size distribution follows a log-normal distribution which suggests that the result was correct for this well-annealed sample. Based on the measured grain centers and grain sizes, the Laguerre tessellation was computed. How well the Laguerre tessellation represented the underlying grain structure was tested by comparing grain size distributions of the measurements and the Laguerre tessellation. This showed a high similarity between the two distributions, meaning that the Laguerre tessellation provides a reasonable representation of the grain structure.
The grain neighborship could easily be computed from the Laguerre tessellation which is needed in connection with building models of the grain rotation during plastic deformation as described in the introduction. Even though the Laguerre tessellation is not guaranteed to reproduce the grain neighborship 100 % correctly, the verification of the Laguerre tessellation in 4.4 showed that the number of wrong neighbors per grains is limited to a only a few. This small systematic error may not cause significant changes to the overall result on the individual grain's rotation during plastic deformation as the sample contains many hundreds of grains. Due to the large sample-to-detector distance it would have been possible to use the Boxscan in the second part of the experiment where a stress rig was needed.
Changing some of the experimental parameters could have reduced the acquisition time. When the purpose is to produce grain maps using the Laguerre tessellation and not ART, an ω-interval of 120 degrees is more than enough. Reducing the ω-interval to two perpendicular 20 degree intervals and including

more than three Debye-Scherrer rings would probably be enough to give good estimates of the grain centers and grain sizes. This could theoretically cut the acquisition time down to 4 hours for the same step size and the same large volume.

Chapter 6

Summary and outlook

Within the last decade a number of techniques for non-destructive 3-dimensional X-ray characterisation of polycrystalline materials have been developed. The different techniques have different strengths and weaknesses, but for most of the techniques, the limiting factor have been the resolution of the detector. To overcome this, a scanning technique must be employed, which until now have been slow for mapping out large volumes.
In this PhD-thesis, a technique using standard resolution detectors in combination with fine-stepping mechanics was studied. The aim was to develop and verify the concept and show that it was applicable to real samples. Furthermore, the possibility to reconstruct the grain shape using the Boxscan technique was studied.

The Boxscan technique

The Boxscan technique is founded on three pillars: X-rays crystallography, a special scanning procedure and an indexing routine in 6 dimensional space.
X-ray crystallography is the physical principle that the technique relies on. The scattering of the X-rays in the individual crystallites enabled the measurement of hundreds of grains simultaneously using only a farfield detector. The use of a farfield detector makes it possible to employ spacious equipment which is needed for in-situ experiments. A special scanning procedure, which probed the sample from two perpendicular directions in combination with sample rotation, produced a huge amount of data containing both 3 dimensional spatial information as well as orientation information about the grains. The scanning procedure utilised boxbeams, which are extended line-beams, and scanning the sample twice in two perpendicular directions with boxbeams, gave similar information as a traditional point scan, but reduced the number of measurement positions significantly, i.e. larger volumes could be mapped out faster than the traditional point scan. A novel 6 dimensional indexing routine was developed to carry out the rather complex task of isolating the information coming from the individual grains in the huge amount of data.

To verify that the Boxscan technique is not only applicable in theory, the technique was applied to a titanium alloy sample and the grains in a subvolume of the sample was indexed. For verification, the same titanium sample was scanned with phase contrast tomography and it was demonstrated that the Boxscan technique is capable of indexing grains and determining the grain centres with a precision that is better than the step size in the scanning procedure. The orientation information of the grains was verified by applying another well-tested method to the same data and comparing the two outcomes. The result showed that there was an average difference of 0.7 degrees in misorientation between the two results. Out of 159 grains, the Boxscan found 129. 27 of the missed grains were small grains or on the edge of the scanning volume. 3 of the missing grains were in the centre of the sample. Furthermore, 4 false grains were found. Even though the Boxscan technique did not find all grains and detected a few false grains, it still showed that the concept is applicable to real experimental data. The fact that the grain centres can be found with a precision that is better than the step size is encouraging, as this means that it is possible to measure grain centres in 3 dimensions with sub-micron precision even with today's standard laboratory equipment.
Interesting about the Boxscan as a method, is that it is could be utilised in experiments with other types of measured signals where 3 dimensional information is required. Especially the use of two boxbeams as a replacement for a point beam is intersting. In the work by P.Bleuet [21] multiple signals, including the diffraction and fluorescence signal, are measured from a sample using a point beam. An obvious experiment would be to apply the scanning technique of the Boxscan to this setup.
The Boxscan technique is not strictly dependent on a synchrotron source. The technique could be used in combination with a regular laboratory X-ray source. The lower flux would of course mean that the exposure time would increase and thus making it less suitable for dynamic experiments, but still useful for small scale experiments, test experiments or static experiments.

Reconstruction of volumetric 3D grain maps

The part of the PhD-project dealing with the reconstruction of volumetric 3D grain maps from the Boxscan technique consisted of three smaller studies. First, a study of representation of 3D grain maps by the Laguerre tessellation was conducted. This was followed by a reconstruction of individual grains by Algebraic Reconstruction Technique and a more theoretical study of the minimum number of projections needed to reconstruct grains.
The study of the Laguerre tessellation showed that even though the model was only fed with the grain centres and the grain size, it would still produce representations of the underlying grain structure which were significantly better than the corresponding representation using a Voronoi tessellation. The Laguerre tessellation could reproduce the true neighborship between grains with less than two errors on average.
Stepping up one level and using the generated profiles from a grain to reconstruct

it's full 3D shape using Algebraic Reconstruction Technique (ART), showed very promising results. Applied to one grain with a grain radius of $17.3\mu m$, the distance between the reconstructed shape boundary and the verification data was on average 2.7 micrometres with a maximum of 5.8 micrometres.
A study of the parameters influence on the ART-reconstruction indicated that it is more necessary to have information from several directions, than to have finely sampled information. Incorporating an Euler circle into the experimental setup would enable the possibility go get information from any direction. Furthermore, this could speed up the data acquisition as no de-focusing of the beam would be needed when scanning horizontally. The drawback of introducing the Euler circle would be wobble (typically around a few micrometres) which would lower the precision of the measurements. Higher flux due to not de-focussing the beam and the introduction of wobble point towards using this setup for mapping out very large samples with a coarse grain structure, e.g. $50\mu m$. The high flux is needed to penetrate the large sample volume and even with a wobble of a few micrometres the measurement error would still be low compared to the grain size.
A smoothing effect on the reconstructed shape was observed which potentially could be reduced by reconstructing multiple grains at the same time. One way to reconstruct multiple grains at the same time would be to apply a Monte Carlo Optimization scheme. The Monte Carlo approach would significantly increase the size and the complexity of the system but would at the same time ensure that the found grain structure was space-filling and non-overlapping.
The third small study of part two in this PhD-thesis was about finding the required minimum number of projections needed to reconstruct a grain correctly. For more precise results, linear programming was used to find the solution instead of ART. Applied to six different voxelized shapes, three convex shapes and three grains, the results indicated that more than 14 projections would reconstruct all the given shapes correctly. From an experimental point of view, such a number is very useful, as it sets the limits for how much data is needed to be able to reconstruct the shapes of the grains. This study is quite simple but still shows that a lower limit may exist as in the 2 dimensional case. A much larger and more theoretical study must be conducted to verify that this number actually exist. Using the linear programming approach, the uniqueness of the reconstructions was also attempted to be tested, but it was not a success due to the numerical issues with the software.

Application to large volume

As a part of a collaboration with Cornell University and the Advances Photon Source, the Boxscan technique was applied to a β-titanium alloy, β21s. The sample was rectangular with a cross section of $700 \times 700\mu$. A vertical range of 400μ was studied and 1265 grain were found in the volume. The measured grain size distribution was found to be very similar the expected log-normal distribution for well-annealed samples.

A grain map of the sample was produced by a Laguerre tessellation and a comparison between the grain size distributions of the measurements and the Laguerre tessellation concluded that it represented the underlying grain structure. From the Laguerre tessellation it would be possible to compute the grain neighborship for finding the relation between individual grains' rotation during plastic deformation.
The experiment showed the strength of the Boxscan technique. Using only a standard farfield detector, it was possible to compute a grain map containing many hundred grains which represented the measured grain structure well. Due to the large sample to detector distance it would have been possible to use the Boxscan in the second part of the experiment where a stress rig was needed.
Changing some of the experimental parameters could potentially have reduce the acquisition to 4 hours for the same sample volume making it possible to conduct several stress-strain measurements on the same sample in one beam time.

Overall conclusions

Overall, it has been shown that the Boxscan technique can measure grain centres with a precision that is better than the step size, which potentially allows for determination of grain centres positions in 3D with a precision as high as $100nm$ with today's equipment. Laguerre tessellations based on Boxscan measurements were in good agreement with the true measured grain structure and made it possible to find grain neighborship. Further incorporation of profile information from grains showed that the 3D grain shape of a single grain could be reconstructed using the algebraic reconstruction technique (ART). The reconstruction error was seen to be dependent on how many directions that were included in the ART reconstruction and from linear programming it was learned that there potentially exist a minimum number of projections needed to reconstruct a 3D shape correctly. Applying the Boxscan technique to a large volume made it clear that it is possible to map hundreds of grains in a sample using only a standard farfield detector and still leaving room for equipment. In conclusion, it has been showed that the Boxscan technique is a fully functional technique that fills the gap between today's imaging and scanning techniques.

Appendix A

Publications

A.1 On the Use of Laguerre Tessellations for Represention of 3D grain structures

ADVANCED ENGINEERING MATERIALS

DOI: 10.1002/adem.201000258

On the Use of Laguerre Tessellations for Representations of 3D Grain Structures**

By *Allan Lyckegaard*, Erik Mejdal Lauridsen, Wolfgang Ludwig, Richard Warren Fonda* and *Henning Friis Poulsen*

Accurate descriptions of 3D grain structures in polycrystalline materials are of key interest as the grain structure is closely correlated to the macroscopic properties of the material. In the present study, we investigate the accuracy of using Laguerre tessellations to represent 3D grain structures from only the spatial center of mass location and the volume of the grains. The ability of Laguerre tessellations to describe accurate grain shapes and topologies of real 3D grain structures are revealed by direct comparison to 3D reconstructions of an un-deformed meta-stable β -titanium alloy obtained by phase-contrast micro-tomography. This study reveals that (volume weighted) Laguerre tessellations are superior to classical Voronoi tessellations when it comes to providing accurate representations of real 3D grain structures. Furthermore, although the Laguerre tessellations were only able to correctly describe the local arrangements of grains (i.e., the grain neighbors and number of grain facets) for 31.8% of the investigated grains, the Laguerre tessellations were able to accurately describe statistical grain characteristics such as grain size distributions and grain neighbor distributions.

Generation of realistic artificial 3D grain structures for use in modeling has gained increasing attention during the last two decades due to significant enhancements in the capabilities of large-scale 3D computer simulations. One commonly chosen model is the Laguerre tessellation (also known as weighted Voronoi tessellations or power diagrams).[1] As in the case of the classical Voronoi tessellation, Laguerre tessellations also partition space into convex polyhedra with planar faces. The advantage of the Laguerre tessellations, compared to the classical Voronoi tessellation, is that it allows for a wider range of grain structures by means of weighting factors.

The simplicity of Laguerre tessellations has made them attractive candidates for use in modeling of grain structure dynamics. A 2D Laguerre model combined with motion equations for simulating coarsening of grains has found good agreement with the theoretically predicted grain size distributions.[2,3] A further extension of this model into 3D also yielded a good correspondence with the experimentally determined grain size distributions.[4] Similarly, it has been demonstrated that a grain growth simulation using 3D Laguerre diagrams follows the predicted Hillert distribution.[5] Recently, Laguerre diagrams have been coupled with an optimization scheme to generate representative artificial 3D grain structures based on 2D experimental input.[6] All of these studies have in common a validation of the generated Laguerre structures against either theoretical predictions or measurements from 2D experimental observations. As previously commented, this is first and foremost due to lack of experimentally determined 3D grain structures.[4] Thus, it still remains to be proven to what extent Laguerre tessellations

[*] *Dr. A. Lyckegaard, Dr. E. M. Lauridsen, Dr. H. F. Poulsen*
Center for Fundamental Research: Metal Structures in 4D, Risø-DTU Frederiksborgvej 399, DK-4000 Roskilde, (Denmark)
E-mail: ally@risoe.dtu.dk
Dr. W. Ludwig
European Synchrotron Radiation Facility, 6 Rue Jules Horowitz 38043 Grenoble Cedex 9, (France)
Dr. R. W. Fonda
Naval Research Laboratory, 4555 Overlook Avenue SW Washington, DC 20375, (USA)

[**] *The authors thank Stefan Othmar Poulsen for assistance with the image analysis and doing the manual segmentation of the grain boundaries and the European Synchrotron Radiation Facility for provision of beam time. A.L., E.M.L., W.L., and H.F.P. acknowledge the Danish National Research Foundation and the Danish Natural Science Research Council (via DANSCATT) for supporting the Center for Fundamental Research: Metal Structures in 4D, within which part of this work was performed and E.M.L. and R.W.F. furthermore acknowledge the support jointly sponsored by the Office of Naval Research and DARPA as part of the Dynamic 3-D Digital Structure Program (Grant numbers N00015-05-1-0510 08-WX20726).*

 © 2010 WILEY-VCH Verlag GmbH & Co. KGaA, Weinheim

COMMUNICATION

resemble real 3D grain structures, both in terms of statistical measures such as grain size distributions, and in terms of local topology measures such as the number of neighboring grains.

Measurements of 3D grain structures are becoming increasingly important for both the input and validation of 3D computer simulations.[7] The recent progress in automated serial sectioning techniques (based on optical microscopy[8] or electron microscopy[9]), and synchrotron based non-destructive 3D grain mapping techniques such as 3D X-ray Diffraction (3DXRD) microscopy[10] and diffraction contrast tomography (DCT)[11] has facilitated the acquisition of 3D grain structure data. Full reconstructions of 3D grain structures are thus becoming more common and can to some extent replace the need for artificially generated grain structures.

For some applications (e.g., grain–grain interactions during deformation[12] or studies of grain growth[13] it may be sufficient to know the topology of the grain structure (i.e., which grains are neighbors), without needing to know the exact morphology of the grains. For such cases, simplified versions of 3DXRD microscopy and DCT have been developed which are capable of determining center of mass (CMS), volume, and crystallography information for 1 000–2 000 grains (in preparation). For situations where large sample environments prevent the use of high resolution near-field detectors, an alternative technique has been developed based on beam scanning using a conventional far-field detector that also provides additional information on the aspect ratios of the grains.[14,15] Hence, it is of interest to investigate how accurately Laguerre tessellations generated from knowledge of the CMS locations and grain volumes can describe the topological state of the system.

Laguerre tessellations can also be used to construct artificial grain structure representations for very large simulations (>2 000 grains), or to generate multiple grain structure representations fulfilling specific macroscopic properties (i.e., size distribution and texture). It is particularly important in this context to verify the accuracy to which Laguerre tessellations represent real 3D grain structures.

The aim of the paper is therefore twofold: a) to investigate how well Laguerre tessellations can accurately represent actual 3D grain structures and b) to what extent can Laguerre tessellations be used in combination with experimentally determined CMS and volume information to extract the underlying unknown topology characteristics.

Laguerre Tessellations

Laguerre tessellations are a weighted version of the well-known Voronoi tessellation.[1] Given a set of n sites $p_i = (s_i, w_i)$, $i = 1....n$, where $s_i \in R^d$ is a seed point and $w_i \in R$ is a weight. A Laguerre tessellation is then a convex subdivision of d-dimensional space into cells C_i fulfilling

$$C_i = \left\{ X \in R^d \middle| \|X - s_i\|^2 - w_i < \|X - s_j\|^2 - w_j, i \neq j \right\} \quad (1)$$

For the case $w_1 = w_2 = .. . = w_n$, this expression reduces to a normal Voronoi tessellation. However, whereas a normal Voronoi tessellation always results in n cells with the seed points s_i located inside their respective cells, this is not necessarily the case for the Laguerre tessellation. In the case of a site p_i with a very small weight w_i compared to its neighboring sites, that site may be located outside its own cell C_i or may even have an empty cell assigned to it.

One possible visualization of the Laguerre tessellation is as an intersection of spheres with different radii. Taking the left side of the ''<'' in Eq. (1), we can interpret w_i as the squared radius r_i^2 of a sphere. In fact, knowing an estimate $\hat{V}_i$ of the volume for a cell C_i we can compute w_i if we assume spherical cells.

$$\hat{V}_i = \frac{4}{3}\pi r_i^3 = \frac{4}{3}\pi w_i^{\frac{3}{2}} \Leftrightarrow w_i = \left(\frac{3\hat{V}_i}{4\pi}\right)^{\frac{2}{3}} \quad (2)$$

It is worth mentioning that the actual volume V_i of a cell C_i in the Laguerre tessellation is not necessarily the same as the estimate of the volume $\hat{V}_i$. Likewise, the CMS for a Laguerre cell C_i, denoted by μ_i, is not necessarily at the same location as the seed point s_i. However, if the CMS μ_i is known but the seed point s_i for some reason is unknown (as in the case for a measured grain structure), it is still possible to estimate the location of the seed point.

To reconstruct a Laguerre cell C_a, both the seed point s_a and the weight w_a must be known. However, the experimental techniques considered in this paper only provide the CMS μ_a and the weight w_a, and do not specify the seed point s_a. Fortunately, knowledge of the CMS and weight can be used to provide an estimate of the seed point s_a. Generating a new Laguerre cell using μ_a as the seed point (i.e., $s_b = \mu_a$) and the weight w_a would yield cell C_b with CMS μ_b, which is spatially shifted but, to a first approximation, similar to C_a in shape and size under the assumption that μ_a is not far away from the seed point s_a (see Fig. 1). For both cells we can compute the vector h between the seed point and CMS, i.e., $h_a = \mu_a - s_a$ and $h_b = \mu_b - s_b = \mu_b - \mu_a$. Assuming the cells are similar we can give an estimate of s_a by setting $h_a = h_b$

$$h_a = h_b \Leftrightarrow \mu_a - s_a = \mu_b - \mu_a \Leftrightarrow s_a = 2\mu_a - \mu_b \quad (3)$$

In practice, this means that if only the CMS is known, it is necessary to perform the Laguerre tessellation twice: first to get an estimate of s_a and a second time to get the final tessellation. For cells with a very small weight in a neighborhood of much larger cells, the previously mentioned assumptions may break down since much of the topology of such small cells are mostly determined by the larger neighbors. Simulation results showing the justification of this heuristic can be found in the result section.

Software for computing a voxelized version of the Laguerre tessellation was developed in Matlab and is included as part of the FABLE software package (http://fable.wiki.sourceforge.net/).

 © 2010 WILEY-VCH Verlag GmbH & Co. KGaA, Weinheim

ADVANCED ENGINEERING MATERIALS

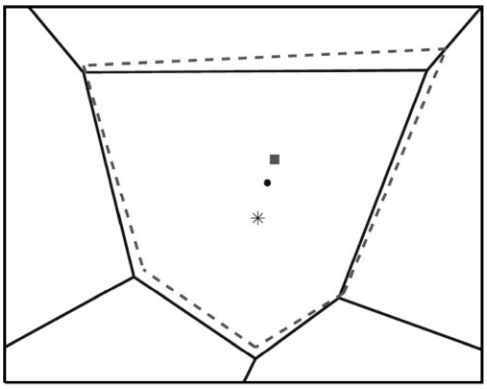

Fig. 1. An estimate of s_a (star) can be found from μ_a (bullet) and μ_b (square). The Laguerre cell C_a is illustrated by the solid line and the dashed line illustrates the Laguerre C_b .

Experimental

With the aim of comparing Laguerre tessellation against a real 3D grain structure, a synchrotron micro-tomography experiment was conducted on a meta-stable beta titanium alloy (Timet β21S) at the microtomography beamline ID19 at the European Synchrotron Radiation Facility, Grenoble, France. The β21S alloy used in this study has the advantage that upon annealing for 2 h at 725 °C a secondary (alpha) phase precipitates and decorates the grain boundaries of the initial beta-grain structure. The decorated grain boundaries were visualized by X-ray phase contrast tomography to reveal the underlying 3D grain structure of the beta grains (see Fig. 2). A 300 μm cylinder-shaped sample was scanned with a resolution resulting in a voxel size of 0.7 μm in the final 3D reconstruction. A subvolume of size $240 \times 240 \times 420\ \mu m^3$ was extracted from the reconstruction for analysis. The subvolume had 590 grains with 211 interior grains. The average equivalent sphere radius was 17.8 μm based on all grains, or 19.0 μm if only interior grains are considered.

In order to segment out the individual grains from the raw synchrotron data several pre-processing steps were required. First, artifacts were removed using ring correction software [16]. Second, the signal-to-noise ratio was enhanced using a normalized cross correlation with a grain boundary template. Third, the remaining noise was removed through a manual cleaning. Then a 3D Euclidian distance transform was applied to a thresholded version of the cleaned images followed by a 3D watershed to define the grains and fill in the gaps in the grain boundary network. The image analysis and manual cleaning were done using Matlab (www.mathworks.com), the dipimage toolbox (www.diplib.org), and ImageJ [17]. The final result of this grain boundary segmentation is shown in Fig. 2. The CMS and volume for each 3D grain was easily extracted from the segmentation result and used as input into, and validation of, the generated Laguerre tessellations presented in the remaining part of the paper.

Simulations

A series of simulations were performed to test the applicability of Laguerre tessellations for restoring topological information about 3D grain structures based solely on measurements of CMS and volume of individual grains (using e.g., 3DXRD, DCT, or beam scanning techniques). Of particular interest is the robustness of the Laguerre tessellations toward uncertainties in experimentally determined CMS and volumes. In typical state of the art 3DXRD or DCT experiments the uncertainty on the CMS μ_i is of the order of 2 μm and the relative uncertainty on the volume V_i approximately 10%. Hence, to investigate the influence of experimental uncertainties two types of data sets were simulated using the 3D grain structure determined by microtomography coupled with the typical measurement noise from 3DXRD and DCT on CMS and volume, respectively. For the CMS simulations, the volumes were preserved, i.e., $V_{\mathrm{sim},i} = V_i$, and $\mu_{\mathrm{sim},i} = \mu_i + \varepsilon_i$ where $\|\varepsilon_i\|$ has a normal distribution with zero mean and $3\sigma = 2\,\mu m$, 4 μm, 7 μm, and 10 μm. Similarly, for the volume simulations, the centers of mass were preserved, i.e., $\mu_{\mathrm{sim},i} = \mu_i$ and $V_{\mathrm{sim},i} = V_i + u_i$ where u_i has a normal distribution with zero mean and $3\sigma = 10\%$. All of the simulations were repeated $N_{\mathrm{sim}} = 17$ times to provide sufficient statistics.

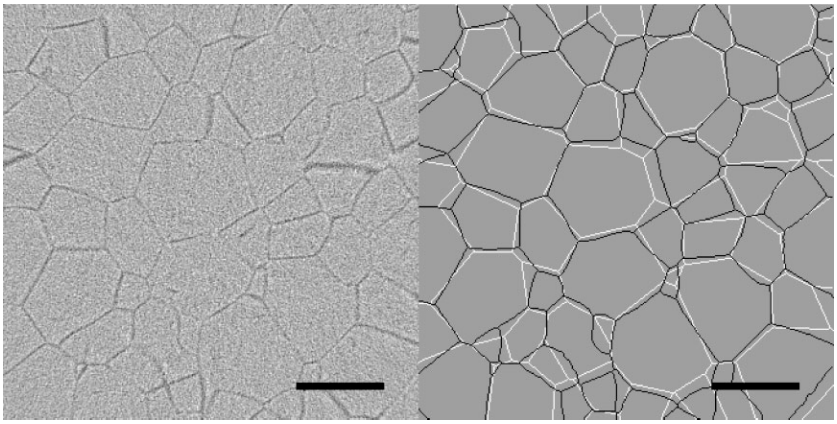

Fig. 2. Left: Slice from the extracted subvolume of the raw reconstructed data from the tomography experiment. The alpha phase result in dark contrast at the beta grain boundaries. Right: Same layer as the left showing segmentation result (black lines) and corresponding Laguerre tessellation (white lines). Scale bar is 50 μm.

Studies of grain structures often use the grain size distribution as a measure of similarity, as this can be inferred from 2D inspections using stereology (under given assumptions about 3D grain shapes). However, in some applications, the local topology of the grains can play a significant role in the dynamics of the system [13]. Thus, a number of figures of merit were chosen in this study to evaluate the similarity between the generated Laguerre tessellations and the real measured 3D grain structure both in terms of global descriptors and local descriptors. The two global descriptors used are (1) 3D grain size distribution and (2) fraction of correctly assigned voxels. The local descriptors used are (1) fraction of grains with all neighbors

 © 2010 WILEY-VCH Verlag GmbH & Co. KGaA, Weinheim

COMMUNICATION

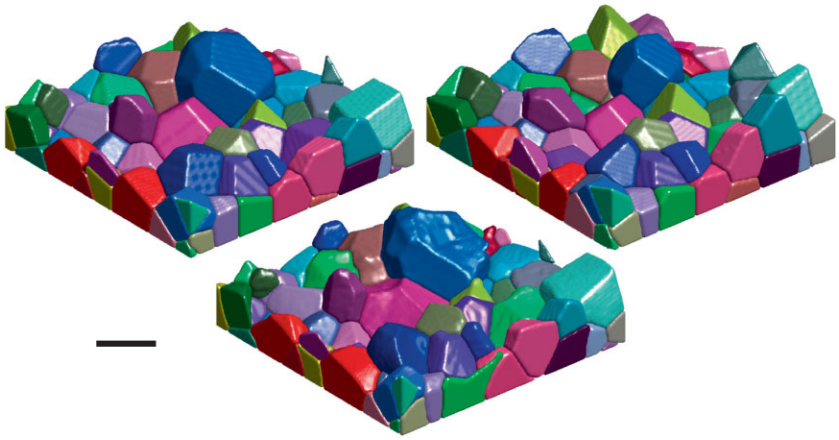

Fig. 3. Top-left: 3D Laguerre tessellation based on the centers of mass and volumes from the 3D grain structure. Bottom: Segmented 3D grain structure. Top-right: 3D Voronoi tessellation based on the CMS from the 3D grain structure. Scale bar corresponds to 50 μm.

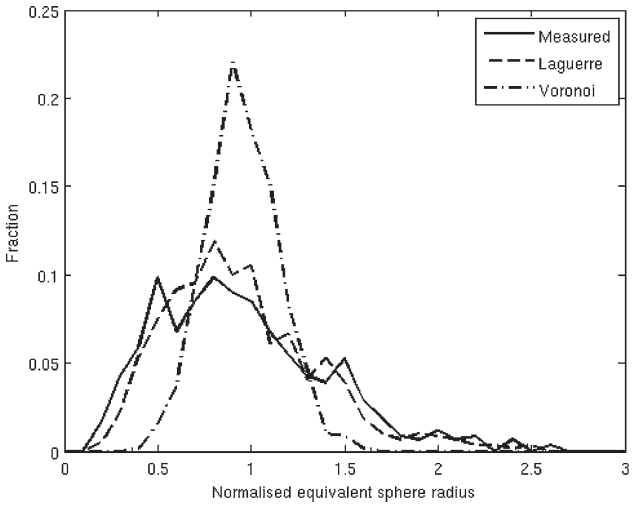

Fig. 4. Distribution of normalized equivalent sphere radius for the experimentally measured grains (solid line), and the grains simulated by Laguerre tessellation (dashed line) and Voronoi tessellation (dashed dotted line).

correct, (2) number of erroneously extra neighbors per grain, (3) number of erroneously missing neighbors per grain, and (4) total number of wrong neighbors per grain. Hence, the 3D grain size distribution and the fraction of correctly labeled voxels are used as global indicators of how well the grain structure is simulated, while the four other descriptors serve as measures of how well the simulation preserves the local topology.

Results

As mentioned in the simulation section, the Laguerre tessellations were run twice in order to account for the fact that the CMS and not the seed points were used to initialize the tessellation. Tests showed that applying a single correction (Eq. 3) increased the simulation results significantly, whereas repeating this correction more than once does not lead to further improvements. Hence, all the results of the Laguerre tessellation presented in this section result from applying a single correction. Fig.3 shows a 3D rendering of a subset of the segmented grain structure (Figure 3 bottom) and the corresponding Voronoi tessellation (Figure 3 top-right) and Laguerre tessellation (Figure 3 top-left). It is clear that some of the non-planar grain boundaries of the real grain structure are not modeled well by either of the tessellations.

However, it is also clear by visual inspection that the Laguerre tessellation generally reflects the real grain structure more accurately when compared to the ordinary un-weighted Voronoi tessellation. The apparent superiority of the Laguerre tessellation is confirmed by analysis of the resulting 3D grain size distributions. Fig. 4 shows the distribution of the normalized equivalent sphere radius, i.e., the equivalent sphere radius for each grain divided by the average equivalent sphere radius. The Laguerre tessellation provides a much better match to the original data than the ordinary Voronoi tessellation. The distribution for the Voronoi tessellation is much more localized and symmetric around the mean grain size than the distribution for the measured titanium data. The distribution for the Laguerre tessellation, on the other hand, follows the distribution of the measured titanium grains quite closely, indicating that the Laguerre tessellation – on a global scale – is able to preserve the size distribution contained in the provided weight factors.

Using the similarity measures mentioned in the previous section, we can quantify how well the Voronoi and Laguerre tessellations model the measured 3D titanium grain structure, see Table 1.

Table 1. Average similarity measures for the tessellations: Voronoi (N = 1), Laguerre without errors (N = 1), Laguerre with 10% volume errors (N = 17) and Laguerre with 2, 4, 7, and 10 μm CMS errors (N = 17).

	Voronoi	Laguerre					
Error type	None	None	Volume	CMS			
Std. of error, 3 sigma	-	-	10%	2 μm	4 μm	7 μm	10 μm
% Correct labelled voxels	59.72	86.30	86.26	85.88	84.72	81.85	78.25
% Grains with all neighbors correct	7.82	31.75	30.90	28.80	23.82	16.99	10.15
# Erroneously extra neighbors/grain	1.87	0.58	0.59	0.62	0.73	0.93	1.23
# Erroneously missing neighbors/grain	1.29	0.64	0.65	0.69	0.76	0.96	1.24
# Total of wrong neighbors/grain	3.16	1.22	1.24	1.31	1.49	1.89	2.47

 © 2010 WILEY-VCH Verlag GmbH & Co. KGaA, Weinheim

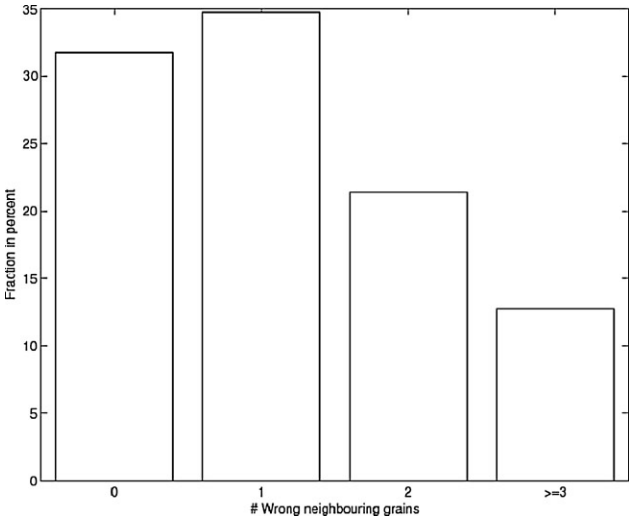

Fig. 5. Histogram of erroneously assigned neighbors for the Laguerre tessellation without noise.

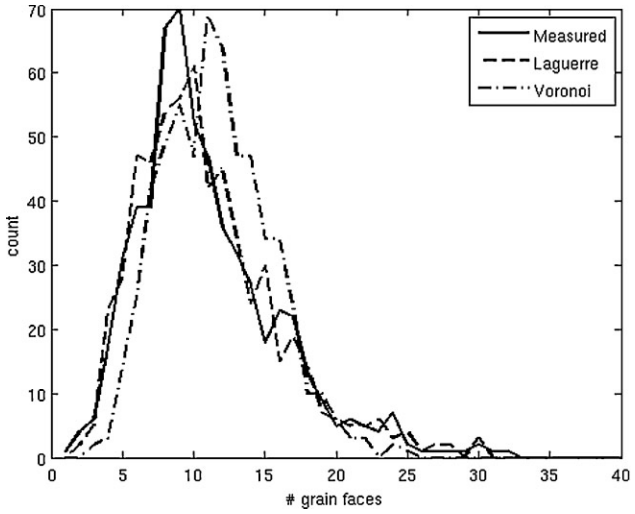

Fig. 6. Distribution of number of grain faces for the measured grain structure (solid line), Laguerre simulations (dashed line), and Voronoi simulation (dashed dotted line).

Comparing the Voronoi tessellation with the Laguerre tessellation we see a significant change in performance: where the Laguerre tessellation labels 86.30% of the voxels correctly, the Voronoi only labels 59.72% correct. This is consistent with the observed grain size distributions shown in Fig. 4.

On the local scale, we see from the histogram of the number of wrongly assigned neighbors per grain shown in Fig. 5, that despite the fact that 87.27% of the grains have less than three wrongly assigned neighbors, only 31.75% of the grains have all the neighbors correctly assigned (for the case of no errors).

Further analysis of the data shows that it is mainly the small grains that have many wrong neighbors compared to their number of faces. This explains why the overall labeling can be good despite having only 31.75% of the grains with correctly assigned neighbors. Errors on a small grain will only affect the overall labeling in a very limited way but will have a larger affect on the number of neighboring grains.

If only the global statistics are of importance, then the distributions of grain faces shown in Fig. 6 demonstrate that the grain structure produced by the Laguerre tessellation accurately preserves the overall topological characteristics of the measured grain structure.

Table 1 also lists the simulation results in the presence of experimental noise. These results demonstrate that the Laguerre tessellations are robust against typical errors in volume, but not as robust against errors in CMS. However, CMS errors on the order of 2 μm, typical of state of the art synchrotron measurements, exhibit only very little decrease in the accuracy of this technique. The fraction of correct labeled voxels only drops to 85.88% and the average number of wrong neighbors per grain rises slightly to 1.31. As would be expected, however, these numbers worsen with increasing noise in the CMS measurements, until only 10% of the grains have the correct neighbors with CMS errors of 10 μm.

Discussion

In the motivation of the current studies two questions were raised; (1) how well do Laguerre tessellations resemble actual, well-annealed 3D grain structures, and (2) to what extent can one use Laguerre tessellations in combination with experimentally determined CMS and volume information to extract the underlying unknown topology characteristics.

The results presented in this paper clearly demonstrate that Laguerre tessellations perform quite well in approximating well-annealed polycrystalline 3D grain structures for statistical studies, i.e., for use in large-scale computer simulations, provided that the weights used in the tessellation are based on representative grain size distributions.

The use of Laguerre tessellations as a tool for extracting the true topological relationships between grains characterized by their experimentally determined CMS and volume information, however, is not as accurate. In cases where an exact topological description is not required, the volume-weighted Laguerre tessellation in its current implementation may be sufficient as only 12.73% of the grains had more than 2 wrongly assigned neighbors. However, for topology-based studies which aim to directly compare simulation results to experimental data, the current implementation of volume-based Laguerre tessellation is not appropriate. The current implementation only makes use of the volume and the CMS information to produce the tessellation. Incorporating additional information such as moments (obtainable by scanning methods[14,15]), into the Laguerre formulation will most likely result in an improved accuracy of the simulated topology of the system.

Another way to improve performance of the method would be to apply an optimization scheme (e.g., Monte Carlo) on top of the Laguerre tessellation. The problem could be posed as a minimization of the difference in volume and CMS as a function of (s_i,w_i). The problem is highly

 © 2010 WILEY-VCH Verlag GmbH & Co. KGaA, Weinheim

dimensioned and all the parameters are coupled, hence traditional minimization methods such as those applying a Newton step, may not be the best choice of minimizer. A Monte Carlo method may be more suitable for this type of problem. In such a Monte Carlo setup, small changes (Δs_i,Δw_i) are added to the current solution to the problem. If the change leads to an improvement of the solution the change is accepted. If the change does not lead to an improved solution, it is only accepted with a certain probability p. For any choice of method, a natural choice of start guess for (s_i,w_i) would be the measured values of the volumes and CMS. This solution may also improve the prediction of grain neighbors for the smaller grains.

Conclusions

A method for modeling 3D grain structures using Laguerre tessellations has been implemented and compared to both a Voronoi tessellation and an experimentally determined 3D grain structure of a meta-stable beta titanium alloy. A set of similarity measures were formulated which demonstrated that the Laguerre tessellation produced a significantly better simulation of the real 3D grain structure, as compared to an ordinary Voronoi tessellation. In terms of grain size distributions and grain neighbor distributions, the generated Laguerre tessellations were very similar to the measured 3D grain structure, but only partially preserved the local topology. Furthermore, simulations of typical measurement errors showed that the Laguerre tessellation is more robust towarderrors in the volume than errors in the CMS.

Received: August 16, 2010
Accepted 28 September 2010

[1] A. Okabe, B. Boots, K. Sugihara, *Spatial Tessellations: Concepts and Applications of Voronoi Diagrams*, Wiley, **1992**.
[2] H. Telley, T. M. Liebling, *Philos. Mag. B.* **1996**, *73*, 395.
[3] H. Telley, T. M. Liebling, *Philos. Mag. B.* **1996**, *73*, 409.
[4] X. Xue, F. Righetti, H. Telley, T. M. Liebling, *Philos. Mag. B.* **1997**, *75*, 567.
[5] E. Schüle, *Comput. Mater. Sci.* **1996**, *5*, 277.
[6] M. Kühn, M. O. Steinhauser, *Appl. Phys. Lett.* **2008**, *93*, 034102.
[7] K. Thornton, H. F. Poulsen, *MRS Bull.* **2008**, *33*, 587.
[8] J. E. Spowart, *Scr. Mater.* **2006**, *55*, 5.
[9] M. D. Uchic, M. A. Groeber, D. M. Dimiduk, J. P. Simmons, *Scr. Mater.* **2006**, *55*, 23.
[10] S. Schmidt, U. L. Olsen, H. F. Poulsen, H. O. Sørensen, E. M. Lauridsen, L. Margulies, C. Maurice, D. Juul Jensen, *Scr. Mater.* **2008**, *59*, 491.
[11] A. King, G. Johnson, D. Engelberg, W. Ludwig, J. Marrow, *Science.* **2008**, *85*, 321.
[12] D. P. Mika, P. R. Dawson, *Mater. Sci. Eng.* **1998**, *A257*, 62.
[13] P. R. Rios, M. E. Glicksman, *Acta Mater.* **2007**, *55*, 1565.
[14] E. M. Lauridsen, S. Schmidt, S. F. Nielsen, L. Margulies, H. F. Poulsen, D. Juul Jensen, *Scr. Mater.* **2006**, *55*, 51.
[15] A. Lyckegaard, A. Alpers, W. Ludwig, R. W. Fonda, L. Margulies, A. Götz, H. O. Sørensen, S. R. Dey, H. F. Poulsen, E. M. Lauridsen, *Proceedings of the 31st Risø Intl. Symp. on Materials Science: Challenges in 3D and 4D characterization techniques* **2010**, 329.
[16] A. Lyckegaard, G. Johnson, P. Tafforeau, http://www.esrf.eu/UsersAndScience/Experiments/Imaging/ID19/Software/ringcorrection, **2007**.
[17] M. D. Abramoff, P. J. Magelhaes, S. J. Ram, *Biophotonics Int.* **2004**, *7*, 36.

 © 2010 WILEY-VCH Verlag GmbH & Co. KGaA, Weinheim

A.2 Recrystallization Kinetics of 50% Cold-Rolled Aluminium

RECRYSTALLIZATION KINETICS OF 50% COLD-ROLLED ALUMINIUM

S. O. Poulsen*, A. Lyckegaard*, J. Oddershede*, E. M. Lauridsen*, C. Gundlach†, C. Curfs‡ and D. Juul Jensen*

* Center for Fundamental Research: Metal Structures in Four Dimensions, Risø DTU, Frederiksborgvej 399, 4000 Roskilde, Denmark
† MAX-lab, Lund University, P.O. Box 118, SE-221 00 Lund, Sweden
‡ European Synchrotron Radiation Facility, 6 Rue Jules Horowitz, 38043 Grenoble, France

ABSTRACT

A three-dimensional X-ray diffraction microscopy (3DXRD) experiment has been performed on 50% cold-rolled aluminium AA1050 to investigate *in situ* the growth rate of individual recrystallizing grains at 310°C and 325°C. Growth rates and apparent activation energies are determined for seven individual grains. It is found that the recrystallization kinetics of the individual grains show large deviations, in good agreement with earlier 3DXRD experiments. It is also found that the recrystallization kinetics at 50% deformation vary less in time than what has been found in similar studies of 90% deformed aluminium.

1. INTRODUCTION

Recrystallization is the process by which largely strain free grains nucleate and grow in a deformed matrix, thus reducing the stored energy of the sample. Experimental examinations of recrystallizing bulk structures have until recently relied on destructive microscopical characterization techniques, where microstructures at different stages of recrystallization are characterized and compared. These experiments can give precise insight into the average recrystallization kinetics, see e.g. (Vandermeer 1995).

The 3D kinetics of individual recrystallizing grains has been accessible by the development of 3DXRD microscopy (Poulsen 2004). Using this technique, it has been found that the kinetics vary substantially between grains in the same recrystallizing sample. Thus, the kinetics of individual grains are poorly described by average models (Lauridsen, Poulsen, Nielsen, and Juul Jensen 2003; Lauridsen, Juul Jensen, Poulsen, and Lienert 2000; Vandermeer,

Lauridsen and Juul Jensen 2004).

This paper describes a 3DXRD investigation of the recrystallization kinetics of 50% cold-rolled aluminium AA1050, which is the same material as previously examined with 3DXRD after 90% deformation (Lauridsen, *et al.* 2000; Lauridsen, *et al.* 2003). A number of grains are examined to qualitatively investigate the effect of the lower degree of deformation.

Following e.g. (Vandermeer, *et al.* 2004), the radial (equivalent spherical) growth rate is assumed to follow an Arrhenius equation:

$$v = v_0 \exp\left(-\frac{Q}{RT}\right) \tag{1}$$

Here v is the radial growth rate ($\partial r/\partial t$), v_0 is a constant with dimension of length per time, Q is the apparent activation energy, R is the universal gas constant and T is the absolute temperature. Thus, equation (1) predicts a constant radial growth rate, hence radial growth that is linear in time.

By determining the radial growth rate of individual grains during isothermal annealing at two different temperatures, the apparent activation energy can be estimated for the individual grains as:

$$Q = R\left(\frac{1}{T_1} - \frac{1}{T_2}\right)^{-1} \ln\frac{v_2}{v_1} \tag{2}$$

where v_1 and v_2 are the radial growth rates determined at temperatures T_1 and T_2, respectively.

2. EXPERIMENTAL DETAILS

Commercial purity aluminium AA1050 was cold-rolled 50%, and a rectangular box-shaped sample was cut from the center. This sample was electropolished to remove preferred nucleation sites along the sample surface caused by cutting. After polishing, the sample measured approximately (3x0.75x0.75) mm in the (RD,TD,ND) directions. The sample was then mounted in a hot finger furnace, enclosed in an argon-filled glass chamber, and the furnace was mounted on the sample stage at the ID11 beamline at the European Synchrotron Radiation Facility (ESRF) in Grenoble, France. A (1800x400) μm rectangular beam profile was defined in the (z,y) directions by two pairs of slits, and the sample was illuminated with 65 keV (high energy) X-rays. The experimental setup was identical to the one used by (Lauridsen, *et al.* 2003), which can be seen on figure 1, where the coordinate system is indicated. The sample was oriented so (RD,TD,ND) are directed along (z,y,x) for a sample rotation of $\omega = 0$.

The experiment was performed by isothermally annealing at 310°C while rotating the sample from $\omega = -15°$ to $\omega = 15°$ in steps of $\Delta\omega = 0.5°$. Images of the diffracted beam were recorded with a 14-bit FReLoN camera during the individual rotations, to provide an ω-integrated intensity. This was repeated several times to provide a time series. The restriction of ω to a 30° window was to increase the temporal resolution.

After annealing for 120 minutes, the temperature was swiftly ramped up to 325°C. When the temperature was stabilized after about 1 minute, image acquisition proceeded for 90 minutes in the same manner as described above.

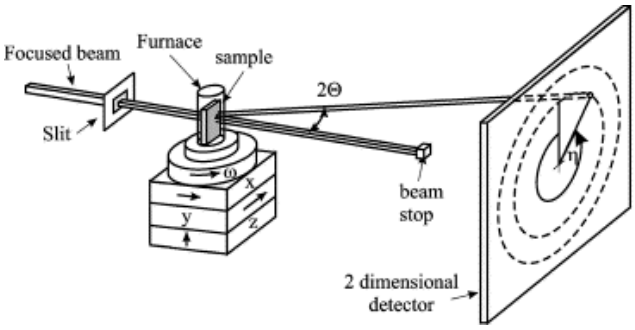

Fig. 1: Experimental setup. Reproduced after (Lauridsen, *et.al.* 2003).

The slits defining the beam profile were periodically widened for an entire ω-cycle during the whole experiment. Grains not fully contained in the smaller gauge volume are then revealed by a discontinuous spike of the intensity of their diffraction spots (Lauridsen 2001). Such grains are left out of further analysis.

3. DATA ANALYSIS

The images obtained are corrected for dark current, spatial (camera) distortion, time dependent synchrotron current, and the Debye-Scherrer rings of interest are integrated over their 2θ spread to produce time series intensity profiles, $I_{2\theta}(\omega, \eta, t)$. At early times, before the visible onset of recrystallization, $I_{2\theta}$ consists of a slowly varying background given by the relatively weak texture of the deformed matrix. As recrystallization progresses, the background is gradually replaced by sharp diffraction spots as the deformed matrix is consumed by the recrystallizing grains.

All diffraction spots in $I_{2\theta}$ are initially identified by their (ω, η) position. As η is given by the orientation of the diffracting plane, and ω relates this orientation to the sample frame of reference, these values are time invariant during this experiment. A specific diffraction spot characterized by $(\omega, \eta) = (\omega_0, \eta_0)$ is then discarded if

a) An η-region, $\Delta\eta = [\eta_0 - x, \eta_0 + x]$ cannot be defined so $I_{2\theta}(\omega_0, \Delta\eta, t)$ shows only the diffraction spot and background for all t.

b) $I_{2\theta}(\omega_{0\pm1}, \Delta\eta, t)$ does not only contain background for all t.

c) The grain giving the diffraction spot is found to not be fully contained in the gauge volume by significant intensity increase upon widening the slits.

If a) is true, then two or more diffraction spots are overlapping, and cannot be separated without making assumptions on their shapes. If b) is true, then the background cannot be determined from $I_{2\theta}(\omega_{0\pm1}, \Delta\eta, t)$. As the ω range in this experiment is not the full 360°, this criterion excludes all diffraction spots in the first and last measured ω ($\omega = \pm 15°$).

Background is estimated as $BG_{2\theta}^{\omega_0}(\eta, t) = I_{2\theta}(\omega_{0\pm1}, \eta, t)/2$, and the normalized grain volumes are determined as $V_{2\theta}^{\omega_0\eta_0}(t) = \int_{\Delta\eta} \left[I_{2\theta}(\omega_0, \eta, t) - BG_{2\theta}^{\omega_0}(\eta, t)\right] \mathrm{d}\eta$. The equivalent spherical radii are determined as $r_{2\theta}^{\omega_0\eta_0}(t) = \sqrt[3]{3V_{2\theta}^{\omega_0\eta_0}(t)/4\pi}$. In order to determine activation energies, straight lines are least-squares fitted to a section of the curves immediately before and after

the temperature increase, the slopes of which give the radial rate of growth, see equation (1). For the grains shown here, these slopes were found to be robust with respect to the selected number of points used in the fit. When the radial rates of growth are determined at the two different temperatures, the apparent activation energy of recrystallization is determined with equation (2).

4. EXPERIMENTAL RESULTS AND DISCUSSION

A total of 471 diffraction spots were identified in the inner six Debye-Scherrer rings. Of these, seven from the {111} ring were chosen for the present analysis. Their volumes and equivalent sphere radii are shown in figures 2(a) and 2(b) respectively.

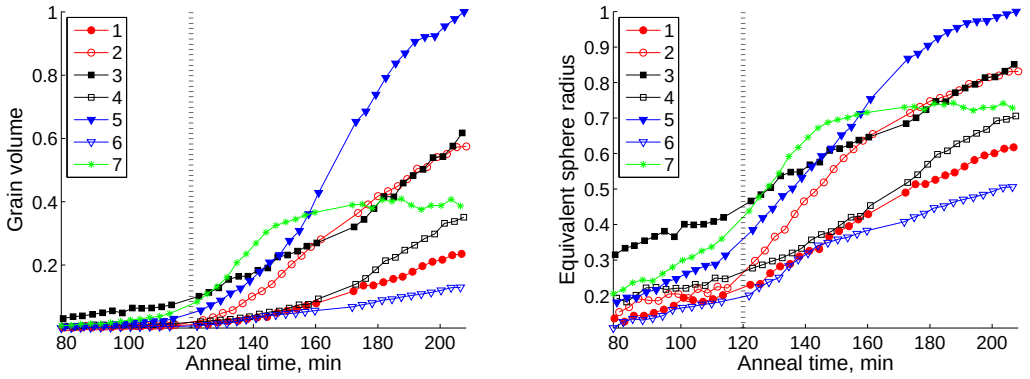

(a) (b)

Fig. 2: (a): Grain volume (arbitrary normalization), (b): Equivalent sphere radii (arbitrary normalization). The dashed lines indicate when the temperature was increased from 310°C to 325°C. The data has not been smoothened, but the measured intensity have been corrected for the beam polarization, so the data for different grains are directly comparable. The equivalent sphere radii are seen to have long stretches of linear growth.

The decrease in growth rate occuring for crystallites 5 and 7 around $t = 160$ min and 140 min respectively may well be attributed to impingement by other recrystallizing nuclei. It is found that the linear growth for all seven crystallites before impingement becomes severe are reasonably well described by a piecewise linear relationship. The radial growth rate vary only little on the timescale of consecutive measurements (3.2 min). Large differences in growth rate and apparent activation energies from grain to grain, see table 1, are observed. This cannot be explained by early size advantages, rather, it seems that each grain has its own kinetic parameters during recrystallization, as is also the conclusion in (Lauridsen, *et al.* 2000; Lauridsen, *et al.* 2003; Vandermeer, *et al.* 2004).

Table 1: Apparent activation energies

Grain #	1	2	3	4	5	6	7
Q [kJ/mole]	181	281	104	193	211	180	183

The largest abrupt change of radial growth rate occurs at the change of temperature as expected, but smaller abrupt changes are also observed, see e.g. curve 6. This shows that the recrystallization does not progress completely smoothly. However, only a few significant changes in growth rate are observed for the seven grains during the recrystallization process. This seems to be in contrast with the findings by (Lauridsen, *et al.* 2000; Lauridsen, *et. al.* 2003), where variations in the growth rates of individual crystallites are observed on the timescale of consecutive measurements. This may be related to the difference in the cold-rolled microstructure for 90% - and 50% deformation. It should be noted, however, that the timescale in the previous measurements is 50 s, whereas the timescale of consecutive measurements in this experiment is 3.2 min

The apparent activation energies are listed in table 1. The average value here, $\langle Q \rangle \approx$ 190 kJ/mole lies between the values reported in (Vandermeer 2000) for iron and silicon impurity-controlled boundary migration, $Q = 172$ kJ/mole and $Q = 217$ kJ/mole. It must however be noted, that seven grains are not enough to generate reliable statistics.

The large relative differences in activation energies are akin to those found by (Vandermeer, *et al.* 2004) investigating recrystallization in 92% cold-rolled copper. These results indicate that activation energy based modelling of the recrystallization kinetics of individual grains will need to take a wide distribution of kinetic parameters into account. Such a procedure may give accurate grain size distributions, but as the experimentally determined growth rate of the recrystallizing grains appear to be varying in time, such an approach would likely only predict the recrystallization kinetics of individual grains poorly.

5. CONCLUSIONS

Investigations of the recrystallization of individual grains in 50% cold-rolled aluminium AA1050 has been performed *in situ* using 3DXRD. The recrystallization kinetics vary not only between grains, but also in time. For the individual grains, the radial growth rates are found to be best described as approximately piecewise linear. Apparent activation energies have been determined displaying considerable variations between grains.

ACKNOWLEDGEMENT

The authors gratefully acknowledge the Danish National Research Foundation for supporting the Center for Fundamental Research: Metal Structures in Four Dimensions. The ESRF is acknowledged for provision of beam time. Additional support for this work was provided by the Danish research council SNF (via DanScatt). Fengxian Lin is thanked for EBSD microscopy.

REFERENCES

Lauridsen, E.M. (2001). Ph.D. thesis: The 3D X-ray diffraction microscope and its applications to the study of recrystallization kinetics. Risø-R-1266(EN): Risø National Laboratory

Lauridsen, E.M., Juul Jensen, D., Poulsen, H.F. and Lienert, U. (2000). Kinetics of individual grains during recrystallization. Scripta mater. 43, 561-566

Lauridsen, E.M., Poulsen, H.F., Nielsen, S.F. and Juul Jensen, D. (2003). Recrystallization kinetics of individual bulk grains in 90% cold-rolled aluminium. Acta mat. 51, 4423-4435

Poulsen, H.F. (2004). Three-Dimensional X-ray Diffraction Microscopy: Mapping Polycrystals and their Dynamics. Springer

Vandermeer, R.A. (1995). Analytical modeling of the kinetics of recrystallization. In: Microstructural and Crystallographic Aspects of Recrystallization. Risø National Laboratory. Editors: Hansen, N. Juul Jensen, D., Liu, Y. and Ralph, B. 193-213

Vandermeer, R.A. (2000). Kinetic aspects of nucleation and growth in recrystallization. In: Recrystallization - Fundamental aspects and relations to deformation microstructure. Risø National Laboratory. Editors: Hansen, N., Huang, X., Juul Jensen, D., Lauridsen, E.M., Leffers, T. Pantleon, W., Sabin, T.J. and Wert, J.A., 179-200

Vandermeer, R.A., Lauridsen, E.M. and Juul Jensen, D. (2004). Growth rate distributions during recrystallization of copper. In: Recrystallization and grain growth. Editors: Bacroix, B., Driver, J.H., LeGall, R., Maurice, C., Penelle, R., Regle, H. and Tabourot, L., 467-470

A.3 3D grain reconstruction from boxscan data

3D GRAIN RECONSTRUCTION FROM BOXSCAN DATA

A. Lyckegaard*, A. Alpers*, W. Ludwig†, R.W. Fonda‡, L. Margulies§, A. Götz†, H.O. Sørensen¶, S.R. Dey‖, H.F. Poulsen* and E. M. Lauridsen*

* Center for Fundamental Research: Metal Structures in Four Dimensions, Materials Research Division, Risø-DTU, DK-4000 Roskilde, Denmark
† European Synchrotron Radiation Facility, BP220, 38043 Grenoble, France
‡ Naval Research Laboratory, Code 6356, 4555 Overlook Avenue, SW, Washington, DC 20375, USA
§ National Synchrotron Light Source II, Brookhaven National Laboratory, Upton, NY 11973-5000, USA
¶ Department of Chemistry, University of Copenhagen, DK-2100 Copenhagen Ø, Denmark
‖ Institute of Materials, Faculty of Mechanical Engineering, Ruhr-University Bochum, D-44801 Bochum, Germany

ABSTRACT

A method for reconstructing the 3D shape of a single grain in a polycrystal from far-field diffraction data is presented. The reconstruction is performed using an iterative algorithm, algebraic reconstruction technique (ART), to solve a linear system of equations obtained from data from the Boxscan technique. The Boxscan technique is a 3D X-ray diffraction-type scanning technique, which – in geometric tomography terms – provides 2-dimensional X-rays of the object as data. In this paper, we report on the first experimental 3D grain shape reconstruction based on a beta-titanium sample. By comparing our results to high-resolution phase contrast tomography, we find that the average error on the position of the grain boundary in this sample is 2.7 micrometers for a grain radius of 17 micrometers. This result is similar to other current methods.

1. INTRODUCTION

The last decades development of nondestructive 3D characterization techniques for polycrystals has been important in the field of materials science. The outcome of such a characterization could be a map of the positions of the grain centers in 3D or even better: a full

3D description of the topology in the volume (which is usually called a 3D grain map).
Within the general approach of 3-Dimensional X-Ray Diffraction (3DXRD) several grain mapping techniques have been explored. In the first one developed (Lauridsen, Schmidt, Suter and Poulsen 2001; Poulsen 2004) the sample is illuminated layer-by-layer with a line-shaped high-energy X-ray beam and the diffracted signal is recorded on both a near-field and a far-field detector as the sample is rotated. Where the far-field signal gives information for resolving the grain orientation, the near-field detector shows a 2D projection of the diffracting grains in the illuminated sample layer. As shown in Poulsen and Fu (2003) and Fu, Knudsen, Poulsen, Herman, Carvalho and Liao (2006) applying algebraic reconstruction techniques (ART) to the near-field signal enables the possibility to produce spacefilling grain maps of the illuminated sample layer.
Ideas from 3DXRD and absorption tomography imaging triggered the development of Diffraction Contrast Tomography (DCT) (Ludwig, Schmidt, Lauridsen and Poulsen 2008; Johnson, King, Honnicke, Marrow and Ludwig 2008; Ludwig, Reischig, King, Herbig, Lauridsen, Johnson, Marrow and Buffiere 2009). While the sample is illuminated layer-by-layer in the methods mentioned above, DCT illuminates the entire volume of interest and records the absorption and the diffraction signal on the same detector positioned in the near-field as the sample is rotated. Again, the detector images show 2D projections of the diffracting grains for different rotation angles. By applying a set of criteria based on the geometry and the diffraction angles it is possible to determine the 2D projections associated with each grain. The 3D shape of the grain is computed from the 2D projections using ART. The use of data back projection is common to the 3DXRD and DCT making both methods sensitive to spot overlap on the detector.
High Energy X-ray Diffraction Microscopy (HEDM) (Suter, Hennessy, Xiao and Lienert 2006), and the methods presented in Alpers, Poulsen, Knudsen and Herman (2006) are variants of the 3DXRD but the grain maps are reconstructed by forward simulating candidate-solutions in a Monte Carlo optimization scheme. The problems with spot overlap are overcome, but powerful computer clusters might be necessary for the methods to be useful in practice.
The spatial resolutions of the methods discussed above are dependent on the pixel size of the detector and the methods require a detector placed close (1-10 mm) to the sample. Such detector positioning is in some cases prohibited due to the presence of spacious experimental equipment, e.g. a furnace or a stress rig. In this case only a far-field detector can be used. With only a far-field detector in the set-up, with 3DXRD one could obtain information on the crystallography, stress-state, volume and center of mass of more than 1000 grains (Oddershede, Schmidt, Poulsen, Sørensen, Wright and Reimers 2010). However, the spatial resolution is reduced to approximately 10 micrometers and no shape information is available. Yet the combination of position and volume makes it possible to generate approximate grain maps based on a Laguerre tesselation (Lyckegaard, Lauridsen, Ludwig, Fonda and Poulsen 2010). Laguerre tesselations are extensions of the Voronoi tesselation and are found to provide a better approximation to the underlying grain structure.
In the techniques discussed above, the limiting factor has been the detector resolution. Where the detectors have resolutions in the range of micrometers, the scanning mechanics has sub-micrometer resolution, some even down to 10s of nanometers. Thus, using the mechanics to probe the sample by translating vertically and horizontally through an extended line beam while recording the diffracted X-rays on a far-field detector could overcome the problem of limited detector resolution. A technique based on this principle has been developed through the Boxscan technique (Lyckegaard, Poulsen, Ludwig, Fonda, Margulies, Götz, Sørensen, Dey and Lauridsen 2010). The Boxscan technique is a variant of 3DXRD, but uses only a far-field detector. It is a scanning technique where two datasets are acquired: one where the sample is scanned vertically and one where it is scanned horizontally.

By combining the two datasets and using the knowledge on the diffracting angles and the geometry, the size and the positions of the grain centers in the sample can be determined with high precision. In addition to this, several projections (2D X-rays in terms of geometric tomography) of the individual grains are obtained. As before, the position of the grain center and the size enables the construction of a grain map using a Laguerre tesselation. In this paper we point out that boxscan data comprise additional information, namely 1D profiles of the grain shapes. We discuss how to exploit this information and report on the first successful 3D grain shape reconstruction directly from Boxscan data (without the use of a tesselation).

2. BOXSCAN TECHNIQUE

2.1 Experimental setup. The experimental setup for the Boxscan technique is sketched in figure 1. The sample is mounted on top of a rotation stage ω and a set of stages for translations in x, y, z (laboratory coordinatesytem). ω rotates around the z-axis. The incoming focused X-ray beam is dimensioned by the motorized slits located in front of the sample. The diffracted X-rays are recorded by a 2D detector located in the far-field, i.e. no spatial information of the grain shape is recorded.
It is convenient to introduce a sample coordinatesytem (x_s, y_s, z_s) which is fixed to the sample, thus its rotation with respect to the laboratory coordinatesytem (x, y, z) is ω. For $\omega = 0$, (x_s, y_s, z_s) and (x, y, z) coincide. Eventually, the grain positions will be expressed in the sample coordinate system.

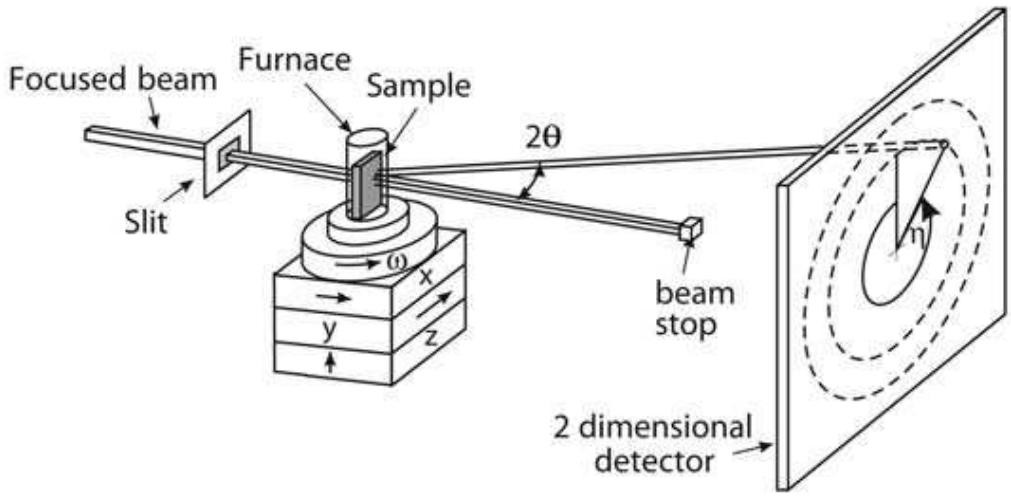

Fig. 1: Experimental setup of the Boxscan technique with definition of angles 2θ, ω and η.

2.2 Data acquisition. The data acquisition consists of two parts, one where the sample is translated vertically in z and one where it is translated horizontally in y. In the first case, the beam is slit down vertically to a horizontal line beam. For each vertical translation $z = z_1...z_c$, a set of detector images are recorded for a series of sample rotations $\omega = \omega_1...\omega_a$. In the second case, the beam is slit down horizontally to a vertical line beam. For each horizontal translation $y = y_1...y_b$, a set of detector images are recorded for the same series of sample rotations $\omega = \omega_1...\omega_a$.
2.3 Data analysis. The diffraction spots are extracted from the images and the values $(\omega, 2\theta, \eta,$

z) or $(\omega, 2\theta, \eta, y)$ of the diffraction angle and the vertical or horizontal translations are stored in a database. The subsets of diffraction spots with similar values $(\omega, 2\theta, \eta)$ and neighbouring values in y or z are denoted a profile, see figure 2. Each profile corresponds to the projection of the diffracting grain's shape onto the axis of translation in the laboratory coordinate system. Likewise, the intensity weighted average of the profile is the grains centre of mass on the axis of translation in the laboratory coordinate system, $y_{cms}(\omega)$ or $z_{cms}(\omega)$, for the given ω-value. It should be stressed here that the grain positions are fixed in the sample coordinate system but moves as a function of ω in the laboratory coordinate system. Each profile and the value $(\omega, 2\theta, \eta, y_{cms}(\omega))$ or $(\omega, 2\theta, \eta, z_{cms}(\omega))$ is stored in the database. Combining a horizontal with a vertical profile, $(\omega, 2\theta, \eta, y_{cms}(\omega))$ and $(\omega, 2\theta, \eta, z_{cms}(\omega))$, where $(\omega, 2\theta, \eta)$ are the same, i.e. from the same grain, gives a set of matches $(\omega, 2\theta, \eta, y_{cms}(\omega), z_{cms}(\omega))$ which can be used for indexing the grains in the dataset.

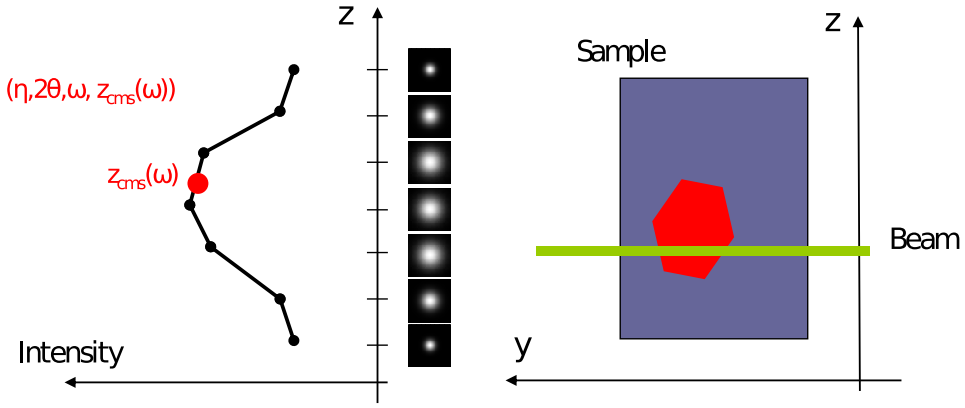

Fig. 2: Generation of vertical profile for one diffraction spot. As the sample is translated with respect to the beam (right) the diffraction spot changes appearance (middle). The profile is defined as the integrated intensity in the spot as function of z (left).

2.4 Indexing. For each match, the value $(\omega, y_{cms}(\omega), z_{cms}(\omega))$ maps to a line parallel to the (x_s, y_s)-plane in the 3D sample coordinate system and $(\omega, 2\theta, \eta)$ maps to a line in 3D orientation space, represented by Rodrigues vectors (for a definition of Rodrigues space see e.g. Morawiec and Field (1996)). A subset of the matches which fulfils $z_{cms}(\omega) = z_0 \pm \Delta z$ are extracted from the database and the intersection points (x_s, y_s, z_s) in the sample coordinate system and (r_1, r_2, r_3) in Rodrigues space for all possible combination of two matches in the subset are computed. If the intersection point (x_s, y_s, z_s) is inside the scanned volume and both exist in the Rodrigues space and is inside the fundamental zone, it is accepted and added to a list of 6D points $(x_s, y_s, z_s, r_1, r_2, r_3)$ for the subset. Now, by definition each grains centre of mass and crystallographic orientation is described by a single point in the 6D space $(x_s, y_s, z_s, r_1, r_2, r_3)$. Two matches from the same grain will intersect in exactly this point, thus the set of 6D points for the subset will have a high density of points where a grain possibly resides in 6D. To find grain candidates in the set of 6D points, a k-nearest neighbours search is performed. Points in 6D with high density are simulated and compared with the measured data. If there is agreement between the simulated grain candidates and measured data, the grain candidate is accepted as a grain.

2.5 Verification. The Boxscan technique was applied to a cylindrical beta titanium sample (300 micrometers in diameter) with an average grain size of 25 micrometers. The sample was scanned in a vertical range of 150 micrometers with a step size of $\delta_z = 4$ micrometers

and in a horizontal range of 330 micrometers with a step size of $\delta_y = 5$ micrometers. The beam had a vertical size of 20 micrometers for translations in z and a horizontal size of 30 micrometers for translations in y. The sample was probed in ω in two perpendicular 30 degrees intervals. The experimental setup used prohibited scanning the full horizontal width of the sample, allowing only a diamond shaped region inside the sample to be analysed.
In order to validate the grain centers determined by the Boxscan technique, they were compared to grain centers derived from a phase contrast tomography scan (PCT) of the same sample (Cloetens, Ludwig, Baruchel, Guigay, Pernot-Rejmankova, Salome-Pateyron, Schlenker, Buffiere, Maire and Peix 1999). The grains in the imaged volume were segmented by a series of image processing steps. First the grain boundaries were enhanced and noise suppressed by correlating with a model of a grain boundary. After this followed a binarization, Euclidean distance transform and a watershedding. After the binarization a few manual corrections were needed to segment the grains correctly.
The grain centers were computed for the grains found from PCT and compared to the ones from the Boxscan technique. The Boxscan technique determined 133 of 159 verification grains correctly. The grain that were not found were either on the limit of the scanned region or very small grains. The error on the grains centers was 2.6 micrometers, i.e. the precision of the grain centers were better than the step sizes $\delta_z = 4$ micrometers and $\delta_y = 5$ micrometers.

3. APPLICATION OF ALGEBRAIC RECONSTRUCTION TECHNIQUE TO BOXSCAN DATA

The algebraic reconstruction technique (ART) as described by Kak and Slaney (1988) is a framework for solving m linear equations in n unknowns $\mathbf{Ax} = \mathbf{b}$, with dimensions $\mathbf{A}_{m\times n}, \mathbf{x}_{n\times 1}, \mathbf{b}_{m\times 1}$. In the random version of ART, we iteratively produce solutions $\mathbf{x}_{k+1}$ by projecting the current solution $\mathbf{x}_k$ onto a random row of the $\mathbf{A}$-matrix:

$$\mathbf{x}_{k+1} = \mathbf{x}_k + \lambda \frac{\mathbf{b}_i - \mathbf{a}_i \mathbf{x}_k}{||\mathbf{a}_i||^2} \mathbf{a}_i \tag{1}$$

where $\mathbf{a}_i$ correspond to the ith row of the $\mathbf{A}$-matrix and λ is a relaxation parameter.
The Boxscan technique gives shape information of the individual grains through the profiles. For a point (t, I) in a profile, where I is the measured intensity and t is a position in y or z, I scales linearly with the integral of the grain volume which the beam illuminated at position t. The beam positions y and z and the beam widths are known, hence it is possible to set up a system of linear equations by subdividing the sample space (x, y, z) into n voxels. The voxels in the subdivided sample space are given a weight between 0 and 1 according to the fraction of the voxel that is illuminated by the beam and placed into the $\mathbf{A}$-matrix as a row. Similarly, I is stored in the same row index of the $\mathbf{b}$-vector. This is repeated for all beam positions in all profiles belonging to one grain. The unknown $\mathbf{x}$-vector holds the intensity of the voxels and will for a correct solution give a 3D description of the grain.
Assuming that the resolution is such that we can assume that the voxels are either completely void or filled by a grain, it is natural to consider $\mathbf{x}$-vectors that are either 0- or 1-valued. ART, however, typically returns solutions $\mathbf{x}$ that are real valued, and not necessarily binary. A common way to overcome this problem is to introduce a threshold. In the following, we find a suitable threshold value by using the knowledge obtainable from the profiles. Since each profile is a projection of the grain volume, it is possible to estimate the grain radius from the profiles belonging to a grain. With a sphere as grain model, a projection of the grain convoluted with the beam profile can be fitted to all profiles in a grain. The average

of all the fitted sphere radii is used for calculating the grain volume, which is used to set the threshold on the ART solution such that the volume of the binarized ART solution is equal to the estimated grain volume.

4. RESULTS

For the chosen grain in the Boxscan dataset, the sample space was voxelized with a voxel size of 2 micrometers. This in conjuction with voxel weights and profiles was used to generate the linear system $\mathbf{Ax} = \mathbf{b}$. The system had 15625 unknowns and 931 equations making it an under-determined system. The ART algorithm was run with $\lambda = 10^{-5}$ and terminated when the figure of merit $||\mathbf{Ax} - \mathbf{b}||/||\mathbf{b}||$ had converged. The average grain radius was estimated to 17 micrometers and the corresponding threshold was set as described above. In figure 3 the reconstructed binarized grain is compared to the same grain segmented from the PCT verification data resampled to a 2 micrometers resolution.

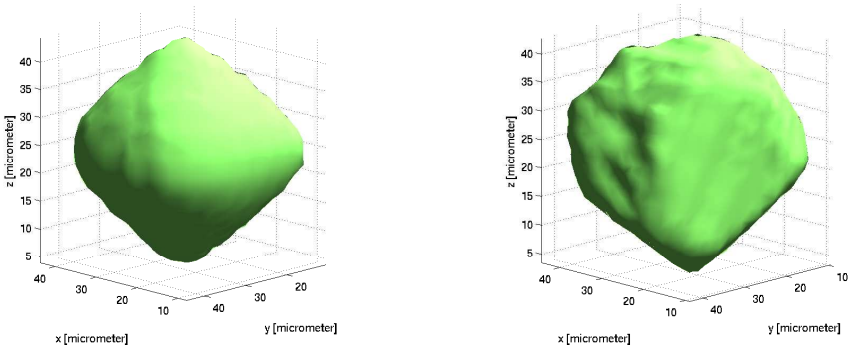

Fig. 3: Left: 3D grain shape found with ART. Right: 3D grain shape from verification data. The units on the axes are micrometers.

The grain reconstructed with ART is not as detailed as the verification data but the overall shape is caught. The ART solution labels 87% of the voxels in the verification data correctly. For a better comparison of the ART solution to the verification data, the distance between the grain boundaries of the two grains are mapped onto the surface of the grain from the verification data, see figure 4, left. As the figure shows, the smooth ART solution is not capable of reconstructing areas around corners. The average distance between the two grain boundaries is 2.7 micrometers. Figure 4, right, shows a single layer of the two grains where red is verification data, green Boxscan data and yellow is overlap. Again it is possible to see that the ART solution has a smoother and more rounded shape than the verification data.

5. DISCUSSION

As laid out in the introduction, the question to be answered was if additional projection information could improve the 3D grain shape reconstructions. Based on the Laguerre tessellation approach, in Lyckegaard et al. (2010a) the number of correctly assigned voxels was measured to be 86% for a sample similar to the one used here. The 86% was measured as an average over all grains where the grain neighbour relationship was known. In our case

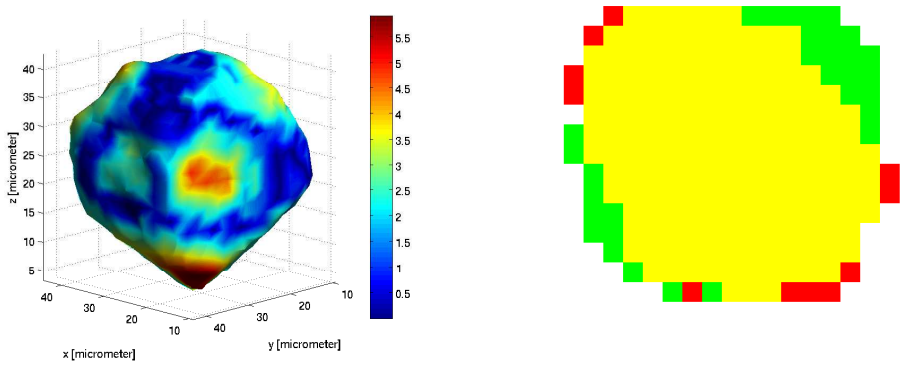

Fig. 4: Left: Distance between the grain boundaries of the ART reconstruction and the verification data for the morphology of the same grain. The colour scale is in units of micrometers. Right: A superposition of the same layer in the two reconstructions of the grain. Here red is verification data, green Boxscan data and yellow is overlap. The pixel size is 2 micrometers.

where the ART was used for reconstructing the 3D grain shape, 87% of the grains voxels were assigned correctly compared to the verification data. This indicates that the use of the additional projection information gives similar results even without information about neighbouring grains.
Since grains are positioned in a spacefilling network and thus are further constrained, it may be possible to improve the grain shape reconstruction even further by using this knowledge. In other words, the current result from ART reconstruction may be improved by extending the ART implementation to simultaneously solve the 3D grain shape of a number of grains, or by combining the output of the ART reconstruction with a Monte Carlo scheme where the shape of a number of grains are refined simultaneously by a forward simulation. Another and maybe more obvious way to improve the result would be to vary the experimental settings. Extending the ω-range such that more projections are measured or decreasing the step sizes δ_y and δ_z could also improve the result.

6. CONCLUSIONS

A method for reconstructing the 3D shape of single grains from Boxscan data was described, implemented and applied to a dataset. Comparison of the reconstructed 3D shape to verification data showed that the reconstruction was smoother and more rounded than the verification data. Despite the smoothing, it is possible to reconstruct the grain with an average error of 2.7 micrometers on the location of the grain boundary.

ACKNOWLEDGEMENT

EML, AL, and RWF gratefully acknowledge funding for this program by the Office of Naval Research as part of the Dynamic 3-D Digital Structure Program under Grant Nos. N00014-05-WX-2-0555 and N00014-05-WX-2-0116 (Dr. J. Christodoulou, program manager). AL,

AA, HOS, SRD and EML furthermore acknowledges the Danish National Research Foundation for supporting the Center for Fundamental Research: Metal Structures in 4D, within which part of this work was performed. The provision of beam time by the ESRF, Grenoble, France, is greatly acknowledged. Furthermore, the staff at Risø-DTU thanks R. Gardner for valuable discussions.

REFERENCES

Alpers, A., Poulsen, H.F., Knudsen, E., and Herman, G.T. (2006). A discrete tomography algorithm for improving the quality of 3DXRD grain maps. J. Appl. Cryst., 39 582-588.

Cloetens, P., Ludwig, W., Baruchel, J., Guigay, J.P., Pernot-Rejmankova, P., Salome-Pateyron, M., Schlenker, M., Buffiere, J.Y., Maire, E. and Peix, G. (1999). Hard x-ray phase imaging using simple propagation of a coherent synchrotron radiation beam. J. Phys. D: Appl. Phys. 32 A145A151.

Fu, X., Knudsen, E., Poulsen, H.F., Herman, G.T., Carvalho, B.M. and Liao H.Y. (2006). Optimized algebraic reconstruction technique for generation of grain maps based on three-dimensional x-ray diffraction (3DXRD). Opt. Eng. 45 116501-1.

Johnson, G., King, A., Honnicke, M.G., Marrow, J. and Ludwig, W. (2008). X-ray diffraction contrast tomography: a novel technique for three-dimensional grain mapping of polycrystals. II. The combined case. J. Appl. Cryst. 41 310-318.

Kak, C.A. and Slaney, M. (1988). Principles of computerized tomographic imaging (IEEE Press, New York).

Lauridsen, E.M., Schmidt, S., Suter, R.M. and Poulsen, H.F. (2001). Tracking: a method for structural chracterization of grains in powders or polycrystals. J. Appl. Cryst. 34 744-750.

Ludwig, W., Schmidt, S., Lauridsen, E.M. and Poulsen, H.F. (2008). X-ray diffraction contrast tomography: a novel technique for three-dimensional grain mapping of polycrystals. I. Direct beam case. J. Appl. Cryst. 41 302-309.

Ludwig, W., Reischig, P., King, A., Herbig, M., Lauridsen, E.M., Johnson, G., Marrow, T.J., and Buffiere, J.Y. (2009). Three-dimensional grain mapping by X-ray diffraction contrast tomography and the use of Friedel pairs in diffaction data analysis. Rev. Sci. Inst. 80 033905-9.

Lyckegaard, A., Lauridsen, E.M., Ludwig, W., Fonda, R.W. and Poulsen, H.F. (2010a) On the use of Laguerre tesselations for representations of 3D grain structures. Adv. Eng. Mat. Accepted.

Lyckegaard, A., Poulsen, H.F., Ludwig, W., Fonda, R.W., Margulies, L., Götz, A., Sørensen, H.O., Dey, S.R. and Lauridsen, E.M (2010b). Boxscan: A novel 3DXRD-based method for mapping of polycrystalline materials. In preparation.

Morawiec, A. and Field, D.P. (1996). Rodrigues parametrization for orientation and misorientation distributions. Philos. Mag. 73. 1113-1130.

Oddershede, J., Schmidt, S., Poulsen, H.F., Sørensen, H.O., Wright, J. and Reimers, W. (2010). Determining grain resolved stresses in polycrystalline materials using three-dimensional X-ray diffraction. J. Appl. Cryst 43 539-549.

Poulsen, H.F and Fu, X. (2003). Generation of grain maps by an algebraic recostruction technique. J. Appl. Cryst. 36 1062-1068.

Poulsen, H.F (2004). Three-dimensional X-ray diffraction microscopy (Springer, New York).

Suter, R.M., Hennessy D., Xiao, C. and Lienert, U. (2006). Forward modelling method for microstructural reconstruction using x-ray diffraction microscopy: Single-crystal verification. Rev. Sci. Instr. 77 123905-1.

A.4 Correction of Ring Artifacts in X-ray Tomographic Images

Correction of Ring Artifacts in X-ray Tomographic Images

Allan Lyckegaard[1], **Greg Johnson**[2] **and Paul Tafforeau**[3]

[1]Materials Research Division, Risø-DTU
Technical University of Denmark
DK-4000 Roskilde, Denmark
ally@transport.dtu.dk

[2]RBR Ltd.
27 Monk St.
Ottawa, Ontario, K1S 3Y7, Canada.

[3]ID19
European Synchrotron Radiation Facility
38043 Grenoble Cedex, France
paul.tafforeau@esrf.fr

ABSTRACT

Ring artifacts are systematic intensity distortions located on concentric circles in reconstructed tomographic X-ray images. When using X-ray tomography to study for instance low-contrast grain boundaries in metals it is crucial to correct for the ring artifacts in the images as they may have the same intensity level as the grain boundaries and thus make it impossible to perform grain segmentation. This paper describes an implementation of a method for correcting the ring artifacts in tomographic X-ray images of simple objects such as metal samples where the object and the background are separable. The method is implemented in Matlab, it works with very little user interaction and may run in parallel on a cluster if applied to a whole stack of images. The strength and robustness of the method implemented will be demonstrated on three tomographic X-ray data sets: a mono-phase β-titanium alloy, a fossil plant and a dual-phased AlCu alloy.

Keywords: Ring artifacts, X-ray tomography, Image analysis, Titanium alloy, Aluminum-copper alloy.

2000 Mathematics Subject Classification: 78-04, 74E15, 78A10.

1 Introduction

In many applications it is important to be able to distinguish between small differences in pixel intensities in an X-ray tomography image. artifacts of various types can make it difficult to do this hence these are unwanted in the image. A common type of artifact in X-ray tomography images are ring artifacts. Pixel errors in the tomographs which cannot be removed by flat field correction, e.g. a non-uniform beam intensity, enter into the sinograms as lines along the angular direction (Vidal, Létang, Peix and Cloetens, 2005). As a property of the reconstruction

algorithm these lines in the sinogram will become concentric (half-)circles in the reconstructed image. There exist a number of ways to reduce ring artifacts. A special mechanical scanning technique that averages the X-ray field and thereby eliminates the ring artifacts has been constructed (Davis and Elliott, 1997). Also, a reduction of the ring artifacts can be achieved with a standard scanning technique. Pre-reconstruction reduction of the ring artifacts using filtering of the sinograms in Fourier space was studied in (Raven, 1998) and in (Boin and Haibel, 2006) the sinograms are corrected by moving average filtering and normalising. For already reconstructed images it is possible to construct an artifact template from a windowed filtering of the polar transformed and masked image (Sijbers and Postnov, 2004). A more sophisticated way is to locate ring artifacts by estimating the local orientation and correct the artifacts by a normalised convolution (Axelsson, Svensson and Borgefors, 2006).
Implementation of the methods mentioned did not give satisfactory results with our data. On the contrary, a Photoshop macro developed for more complex palaeontological samples showed promising results (Tafforeau, 2004). This paper aims to describe a Matlab implementation of a method similar to the Photoshop macro. The reasons for choosing Matlab as the programming language are several: it is widely used in the academic community, it easily integrates with existing software and it has a long list of available toolboxes.

2 Method

2.1 Assumptions of the method

Before describing the method in details it is appropriate to mention the assumptions on which it is based. First of all we assume the ring artifacts are additive, i.e. the acquired image is a sum of the real imaged object and the ring artifacts. Next, for the method to work properly the imaged object must have large areas of uniform intensity which we refer to as large structures. Also, the centre of rotation used in the reconstruction must be known. Finally it is assumed that the original reconstructed image originates from scanning in a 180 degrees range, i.e there are two sets of ring artifacts in one image.

2.2 Description of the method

The method can in short be described in very few steps: First, generate a mask for each of the large structures in the image. For each of these large structures, subtract its own average intensity. Next, transform into polar coordinates (Θ, ρ) and apply a number of filters in angular direction Θ. Transform back into Cartesian coordinates (x, y) and subtract the filtered image from the original to reduce the ring artifacts.
The following sections give a more detailed description of the method.

2.2.1 Masking

Starting out with the original reconstructed image $\mathbf{I}$, figure 1 left, we construct a mask $\mathbf{M}$ annotating large structures with different levels of intensity in the image $\mathbf{I}$. For example the

background could have the value $m = 1$ in the mask and the object $m = 2$. If a more complex object with n intensity levels is imaged one could have more values, i.e. $m = 1 \ldots m_n$.

2.2.2 Large structure removal

For each value m in the mask $\mathbf{M}$, the average intensity μ_m, i.e the average of the pixel intensities $\mathbf{I}(\mathbf{M} = \mathbf{m})$, is computed. A detailed image $\mathbf{D}$ is then created with the operation:

$$\mathbf{D}(\mathbf{M} = \mathbf{m}) = \mathbf{I}(\mathbf{M} = \mathbf{m}) - \mu_{\mathbf{m}}, \quad \mathbf{m} = \mathbf{1}..\mathbf{m_n} \tag{2.1}$$

$\mathbf{D}$ will contain little or no information of the large structures and only smaller details, e.g. cracks, grain boundaries, phase contrast or other edge effects from the masking, and of course the ring artifacts will be present in the image. See figure 1 right.

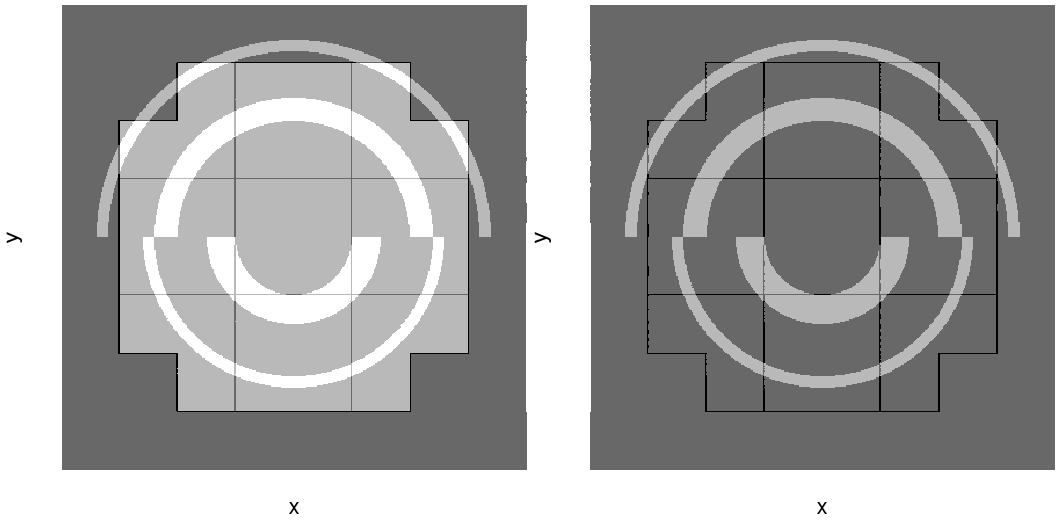

Figure 1: Left: Original image I with ring artefacts. Right: The image D where all the large structures from I are removed.

2.2.3 Small detail removal

Next, transforming $\mathbf{D}$ into polar coordinates (Θ, ρ) and median filtering along the angular direction Θ yields an image $\mathbf{P}$. Because of the circular nature of the ring artifacts, the polar transformation will make it possible to use standard filtering routines for filtering in the angular direction.

The median filtering will remove small detail while still preserving the ring artifacts, since the ring artifact vary only a little along Θ. The main reason for choosing a median filter instead of a linear filter is the presence of phase-contrast. Applying a linear filter in an area with phase-contrast, the filter output would be highly influenced by the extreme valued phase-contrast intensities. See figure 2 left.

2.2.4 Angular smoothing

The ring artifacts are assumed to span 180 degrees each, so $\mathbf{P}$ is split into two halves, $\mathbf{P_1}$ and $\mathbf{P_2}$, each covering an 180 degree ring artifact segment. A pyramid transformation is applied to $\mathbf{P_1}$ and $\mathbf{P_2}$, meaning that $\mathbf{P_1}$ and $\mathbf{P_2}$ are resampled in Θ near the center, i.e. for small ρ, to compensate for the smaller data density there.
Next, a Gaussian blurring is applied along Θ to draw up the ring artifacts and reduce noise, see figure 2 right. This is followed by an inverse pyramid transformation where $\mathbf{P_1}$ and $\mathbf{P_2}$ are resampled back to the previous resolution. All in all, the pyramid transformation followed by filtering and finally inverse pyramid transformation is just another way to filter with a variable width filter.

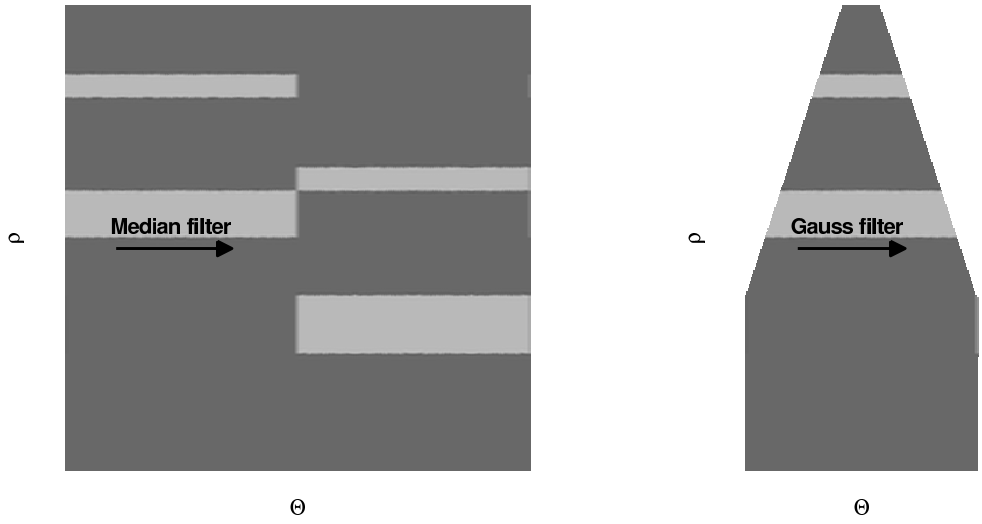

Figure 2: Left: Median filtering of P, the polar transform of D. Right: Gaussian smoothing of the pyramid transformed image $P1$.

2.2.5 Merging

The two halves $\mathbf{P_1}$ and $\mathbf{P_2}$ are now merged again at the same places they were split up and to avoid kinks at the points of merging a small linear filter is applied along Θ. Next, an inverse polar transformation is applied to give an image $\mathbf{R}$ in Cartesian coordinates containing ring artifacts only, see figure 3 left.

2.2.6 Artifact subtraction

Finally, the original image $\mathbf{I}$ has $\mathbf{R}$ subtracted from it resulting in an image where the ring artifacts are significantly reduced, see figure 3 right.

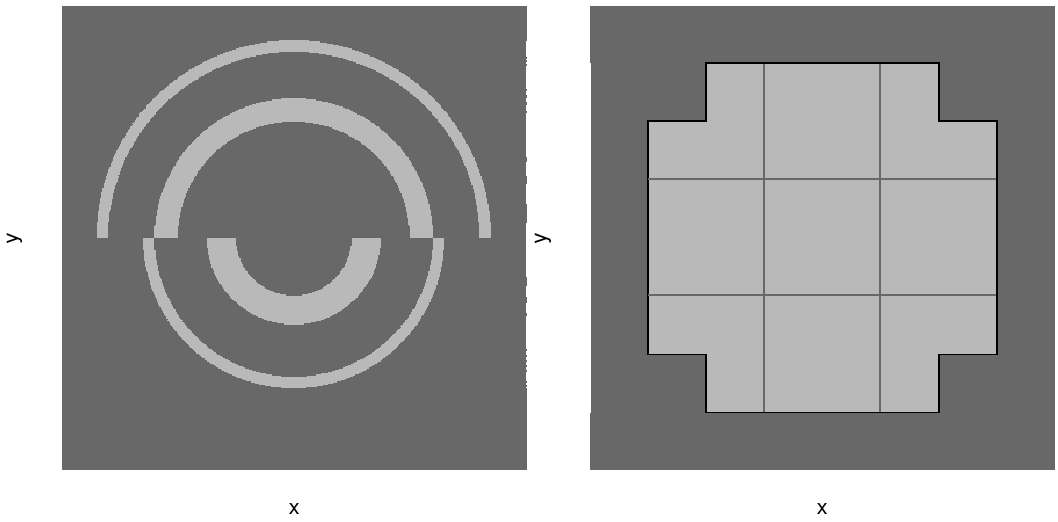

Figure 3: Left: Image of ring artefacts, R, when merging and inverse polar transforming $P1$ and $P2$. Right: Original image I subtracted the ring artefacts image R.

3 Implementation

A Matlab implementation of the method can be provided by contacting the authors. Since the method works on individual image slices it is possible to process a whole reconstructed volume in parallel on a PC-cluster for faster processing.

3.1 Choice of parameters

For a given reconstructed volume (or image), a number of parameters must be set. These parameters include the angular resolution of the polar transformation, filter widths of the median filter for removing small details, the angular Gaussian filter and the angular Gaussian merging filter and finally the height of the pyramid transformation. These parameters are dependent on the object imaged and the structure of the ring artifacts but in practice this dependence is limited, hence only small adjustments are needed. Usually the parameters are determined by trial-end-error and a visual checking of the result.
The parameter choice for processing the images in the results section is shown in table 1.

Angular resolution of the polar transformation	$\frac{1}{4}$ degree
Width of median filter for removing small details	12.25 degrees
Width of angular Gaussian filter	25.00 degrees
Width of angular Gaussian merging filter	12.50 degrees
Height of the pyramid transformation	$\frac{1}{6}$ of the image size

Table 1: Choice of parameters for processing the images in the results section.

3.2 Performance benchmarks

Some benchmarks were made for the Matlab implementation on a PC (AMD Opteron, 2.6 GHz, 64-bit). Images of various size was tested and the running time was recorded, see table 2.
The benchmarks show us that the running time scales linearly with the number of pixels in the image. Analysis of the bottlenecks in the code show that speed-ups can be achieved by implementing a faster inverse polar transformation, e.g. by using lookup-tables.

Image size [pixels]	512^2	848^2	1024^2	2048^2	4096^2
running time [seconds]	~ 2	~ 3	~ 5	~ 12	~ 35

Table 2: Running time of the implemented Matlab method for various image sizes.

4 Results

The method described above was implemented in Matlab and tested on two sets of tomographic images: A mono-phased titanium alloy and a dual-phased aluminium-copper alloy. Both sets of images were acquired at the European Synchrotron Radiation Facility (ESRF) in Grenoble with standard tomographic methods.

4.1 Mono-phase material Ti

A small cylinder (approximately 245 micrometres diameter) of the β-titanium alloy Timetal 21S was used. The size of the scanned volume was $746 \times 746 \times 1024$ pixels with an isotropic pixel size of 0.7 micrometre. Grain boundaries are formed by the α-phase content in the sample and are just visible in the reconstructed images, hence the presence of ring artifacts could give rise to errors in a subsequent automated quantification analysis. It is therefore crucial to be able to remove the ring artifacts without affecting the grain boundaries.
The implemented ring artifact reduction method was applied to each of the images in the scanned volume. Figure 4 shows the original image and the image where the ring artifacts are reduced. The ring artifacts indeed are reduced without affecting grain boundaries. Figure 5 show that even if a ring artifact has the same intensity level as the grain boundaries, the method only reduces the ring artifact.

4.2 Fossil plant

To show the methods robustness towards small details in the image the method is applied to a higly detailed fossil plant. The details of the plant have the same intensity as the ring artifacts, hence it is necessary to remove the ring artifacts before any segmentation methods are applied. Figure 6 show the fossil plant embedded in the stone before and after the ring artifacts are removed. It is clear that the ring artifacts are significantly reduced without affecting e.g. the crack in the stone. Even with a strong ring artifact the details of the plant are not affected by the ring artifact removal, see figure 7.

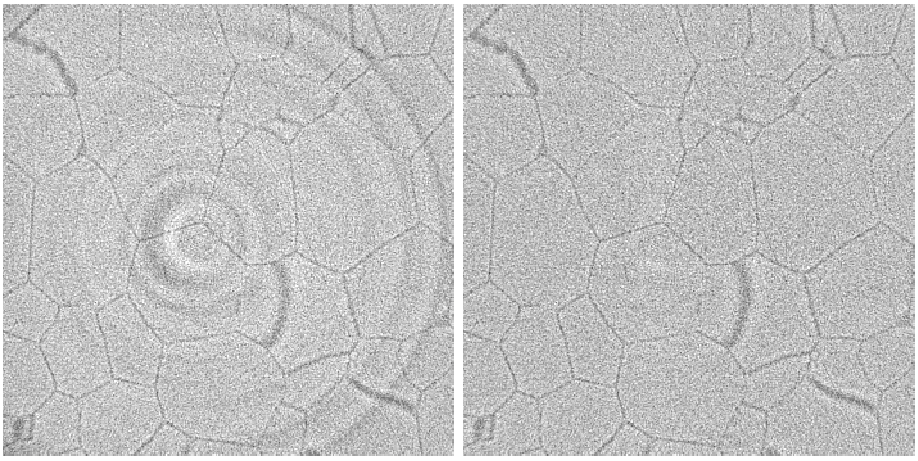

Figure 4: Titanium sample. Upper: Before removing ring artefact. Lower: After removing ring artefact.

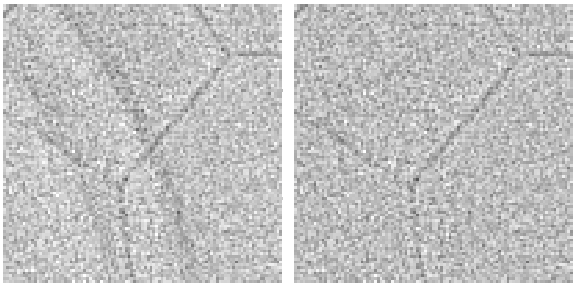

Figure 5: Titanium sample, zoom. Left: Before removing ring artefact. Right: After removing ring artefact.

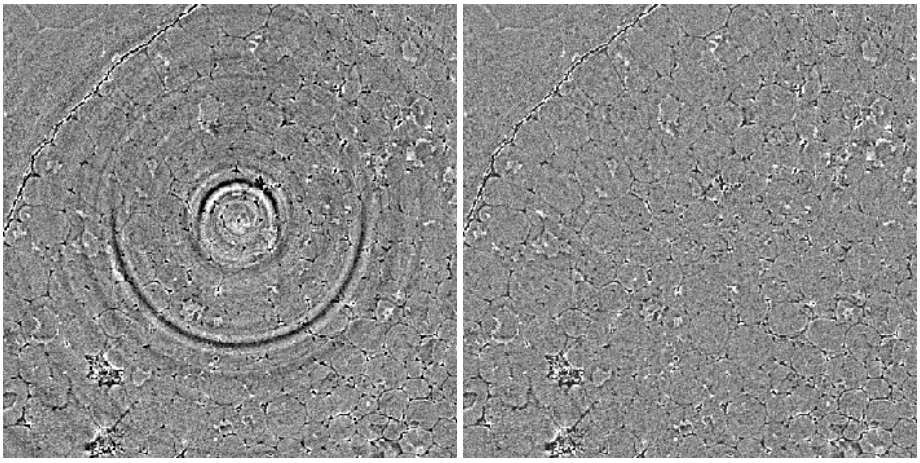

Figure 6: Fossil plant. Left: Before removing ring artefact. Right: After removing ring artefact.

4.3 Dual-phase material AlCu

Like the titanium alloy sample, a small cylinder was used but now made of an alloy of aluminium and copper. Since this sample is a rather more complex one it is necessary to add a level to

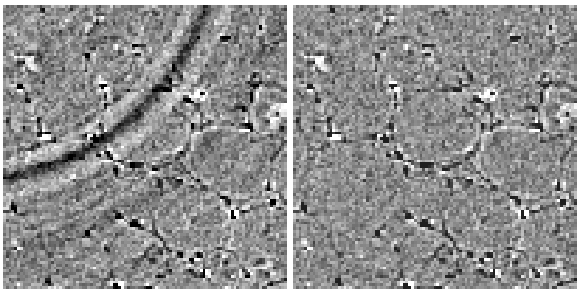

Figure 7: Fossil plant, zoom. Left: Before removing ring artefact. Right: After removing ring artefact.

the masking step. A mask $\mathbf{M}$ is constructed with three values: one for the background, one for the aluminium phase and one for copper phase. Errors in the mask most likely occurs since the ring artifacts make it difficult to perform a perfect image segmentation. Due to the method's subsequent filtering, errors in the mask does not influence the result. Figures 8 show the alloy before and after removal of the ring artifacts. Most of the ring artifacts are removed but a few smaller ones are left near the centre of the sample. Near the centre in the polar coordinate system fewer sampling points are available, thus the quality of the estimated ring artifacts closer to the centre are decreased. Despite the problems with the ring correction near the centre, the resulting image is easier to segment compared to the original.

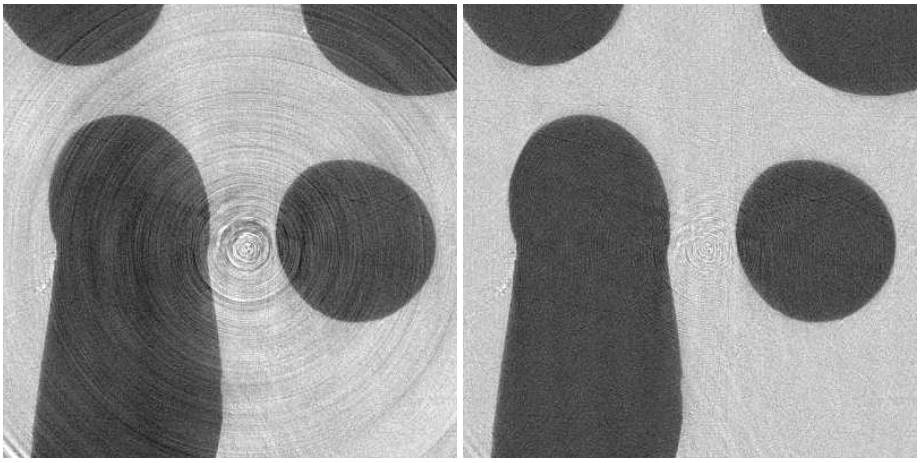

Figure 8: Dual-phase material AlCu , zoom. Left: Before removing ring artefact. Right: After removing ring artefact.

5 Discussion and conclusion

In the previous, the implementation details of a method for correcting ring artifacts in tomographic X-ray images is described. The method applies to images of simple objects and works by a set of image processing steps. The results show that the method successfully corrects ring artifacts or at least significantly reduce them in a fast and robust manner.

The previous sections raise a few questions. The method implemented applies to recon-

structed images but it may be more efficient to correct for ring artifact already in the sinograms. From a computational point, the time consuming polar transform and inverse polar transform could be saved. On the other hand, it may be easier for the user to decide on parameter values when the reconstructed image is used since the actual imaged object can be seen.
The method of course has its limitations. If the reconstructed images has circular structures or structures that are parallel to the angular direction these will be seen as ring artifacts and hence reduced. A possible way to overcome this could be adding support for active regions, i.e. a mask showing where the method could be applied and not. Furthermore, it is difficult to deal with ring artifacts that are saturated since the assumption of additive artifacts break down. If larger stacks of images are to be processed, the method can easily be run in parallel on a cluster since it is applied to individual images.

Acknowledgement

Allan Lyckegaard acknowledges the support sponsored by the Office of Naval Research as part of the Dynamic 3-D Structure Program (Grant N00015-05-1-0510). The European Synchrotron Radiation Facility (ESRF) is acknowledged for provision of synchrotron radiation facilities.

References

Axelsson, M., Svensson, S. and Borgefors, G. 2006. Reduction of Ring Artifacts in High Resolution X-Ray Microtomography Images, *Lecture Notes in Computer Science* **4174**: 61.

Boin, M. and Haibel, A. 2006. Compensation of ring artefacts in synchrotron tomographic images, *Optics Express* **14**(25): 12071–12075.

Davis, G. and Elliott, J. 1997. X-ray microtomography scanner using time-delay integration for elimination of ring artefacts in the reconstructed image, *Nuclear Instruments and Methods in Physics Research Section A: Accelerators, Spectrometers, Detectors and Associated Equipment* **394**(1): 157–162.

Raven, C. 1998. Numerical removal of ring artifacts in microtomography, *Review of Scientific Instruments* **69**: 2978.

Sijbers, J. and Postnov, A. 2004. Reduction of ring artifacts in high resolution micro-CT reconstructions, *Phys. Med. Biol* **49**(247): N253.

Tafforeau, P. 2004. *Aspects Phylogénétiques et Fonctionnels de la Microstructure de l´Email Dentaire et de la Structure Tridimensionnelle des Molaires Chez les Primates Fossiles et Actuels: Apports de la Microtomographie à Rayonnement X Synchrotron*, PhD thesis, Université de Montpellier II.

Vidal, F., Létang, J., Peix, G. and Cloetens, P. 2005. Investigation of artefact sources in synchrotron microtomography via virtual X-ray imaging, *Nuclear Inst. and Methods in Physics Research, B* **234**(3): 333–348.

Bibliography

[1] H. Sörby, "The application of very high powers to the study of the microscopical structure of steel.," *J. Iron Steel Inst.*, vol. 1, pp. 140–144, 1886.

[2] M. Knoll and E. Ruska, "Das elektronenmikroskop.," *Z. Physik*, vol. 78, pp. 318–339, 1932.

[3] M. von Ardenne and D. Beischer, "Untersuchung von metalloxyd-rauchen mit dem universal-elektronenmikroskop," *Zeitschrift Electrochemie*, vol. 46, pp. 270–277, 1940.

[4] D. Williams and C. Carter, *Transmission Electron Microscopy: A Textbook for Materials Science*. Springer, 2nd ed., 2009.

[5] M. Alam, M. Blackman, and D. Pashley, "High-angle kikuchi patterns.," *Proceedings of the Royal Society of London*, vol. A 221, pp. 224–242, 1954.

[6] P. Hirsch, "A study of cold-worked aluminium by an X-ray micro-beam technique. II. Measurement of shapes of spots," *Acta Crystallographica*, vol. 5, no. 2, pp. 168–172, 1952.

[7] P. Hirsch and J. Keller, "A study of cold-worked aluminium by an x-ray micro-beam technique. i. measurement of particle volume and misorientations," *Acta Crystallographica*, vol. 5, pp. 162–167, 1952.

[8] H. Poulsen, *Three Dimensional X-Ray Diffraction Microscopy.* Springer, 2004.

[9] R. Celotta, K. Sköld, J. Levine, and D. Price, *Methods of Experimental Physics, volume 23, part A*. Academic Press, 1986.

[10] J. Hastings, D. Siddons, L. Berman1, and J. Schneider, "Three-crystal spectrometer for 150-kev synchrotron radiation," *Review of Scientific Instruments*, vol. 60, pp. 2398–2401, 1989.

[11] K. Khor, J. Buffiere, W. Ludwig, and I. Sinclair, "High resolution X-ray tomography of micromechanisms of fatigue crack closure," *Scripta Materialia*, vol. 55, no. 1, pp. 47–50, 2006.

[12] W. Ludwig and D. Bellet, "Penetration of liquid gallium into the grain boundaries of aluminium: a synchrotron radiation microtomographic investigation," *Materials Science and Engineering A*, vol. 281, no. 1-2, pp. 198–203, 2000.

[13] W. Ludwig, S. Schmidt, E.M.Lauridsen, and H.F.Poulsen, "X-ray diffraction contrast tomography: a novel technique for three-dimensional grain mapping of polycrystals. i. direct beam case.," *Applied Crystallography*, vol. 41, pp. 302–309, 2008.

[14] G. Johnson, A. King, M. Honnicke, J. Marrow, and W. Ludwig, "X-ray diffraction contrast tomography: a novel technique for three-dimensional grain mapping of polycrystals. II. The combined case," *Journal of Applied Crystallography*, vol. 41, no. 2, pp. 310–318, 2008.

[15] W. Ludwig, P. Reischig, A. King, M. Herbig, E. Lauridsen, G. Johnson, T. Marrow, and J. Buffière, "Three-dimensional grain mapping by x-ray diffraction contrast tomography and the use of Friedel pairs in diffraction data analysis," *Review of Scientific Instruments*, vol. 80, p. 033905, 2009.

[16] P. Cloetens, W. Ludwig, J. Baruchel, D. V. Dyck, J. V. Landuyt, J. Guigay, and M. Schlenker, "Holotomography: Quantitative phase tomography with micrometer resolution using hard synchrotron radiation x rays.," *Applied Physics Letters*, vol. 75, no. 19, pp. 2912–2914, 1999.

[17] J. Spowart, "Automated serial sectioning for 3-d analysis of microstructures.," *Scripta Materialia*, vol. 55, pp. 5–10, 2006.

[18] M. Uchic, M. Groeber, D. Dimiduka, and J. Simmons, "3d microstructural characterization of nickel superalloys via serial-sectioning using a dual beam fib-sem.," *Scripta Materialia*, vol. 55, pp. 23–28, 2006.

[19] M. Laue, "Reflection of x-rays," *Physikalische Zeitschrift*, vol. 14, pp. 421–423, 1913.

[20] B.C.Larson, W. Yang, G. Ice, J. Budai, and J. Tischer., "Three-dimensional x-ray structural microscopy with submicrometre resolution.," *Nature*, vol. 415, pp. 887–890, 2002.

[21] P. Bleuet, E. Welcomme, E. Dooryhée, J. Susini, J. Hodeau, and P. Walter, "Probing the structure of heterogeneous diluted materials by diffraction tomography," *Nature materials*, vol. 7, no. 6, pp. 468–472, 2008.

[22] R. Suter, D. Hennesy, C. Xiao, and U. Lienert., "Forward modelling method for microstructure reconstruction using x-ray diffraction microscopy: Single-crystal verification.," *Review of Scientific Instruments*, vol. 77, no. 123905, pp. 1–12, 2006.

[23] C. Giacovazza, H. Monaco, D. Viterbo, F. Scordari, G. Gilli, G. Zanotti, and M. Catti, *Fundamentals of Crystallography*. Oxford University Press, 1992.

[24] J. Als-Nielsen and D. McMorrow, *Elements of Modern X-ray Physics*. Wiley, 2001.

[25] J. K. Mason and C. A. Schuh, *Electron Backscatter Diffraction in Materials Science*, ch. 3. Springer Science+Business Media, 2009.

[26] A. Morawiec, "Rodrigues parametrization for orientations and misorientation distributions," *Philosophical Magazine A*, vol. 73, pp. 1113–1130, 1996.

[27] A. Heinz and P. Neumann, "Representation of orientation and disorientation data for cubic, hrxagonal, tetragonal and orthorhombic crystals," *Acta. Cryst.*, vol. 47, pp. 780–789, 1991.

[28] Y. He and J. J. Jonas, "Representation of orientation relationships in rodrigues-frank space for any two classes of lattice," *Applied Crystallography*, vol. 40, pp. 559–569, 2007.

[29] A. Morawiec and J. Pospiech, "Some information on quaternions useful in texture calculations," *Textures and microstructures*, vol. 10, pp. 211–216, 1989.

[30] C. Miehe, "Exponential map algorithm for stress updates in anisotropic multiplicative elastoplaticity for single crystals," *International Journal for Numerical Methods in Engineering*, vol. 39, pp. 3367–3390, 1996.

[31] G. Shakhnarovich, T. Darrell, and P. Indyk, *Nearest-Neighbor Methods in Learning and Vision: Theory and Practice*. MIT Press, 2005.

[32] P. J. Huber and E. M. Ronchetti, *Robust statistics*. John Wiley & Sons Inc, 2009.

[33] R. Kahn, R. Fourme, A. Gadet, J. Janin, C. Dumas, and D. André, "Macromolecular crystallography with synchrotron radiation: photographic data collection and polarization correction," *Journal of Applied Crystallography*, vol. 15, no. 3, pp. 330–337, 1982.

[34] A. Hammersley, S. Svensson, A. Thompson, H. Graafsma, Å. Kvick, and J. Moy, "Calibration and correction of distortions in two-dimensional detector systems," *Review of Scientific Instruments*, vol. 66, p. 2729, 1995.

[35] G. Wertheim, M. Butler, K. West, and D. Buchanan, "Determination of the Gaussian and Lorentzian content of experimental line shapes," *Review of Scientific Instruments*, vol. 45, p. 1369, 1974.

[36] C. Kelley, *Iterative methods for optimization*. Society for Industrial Mathematics, 1999.

[37] Y. Ge, C. R. Maurer Jr, and J. M. Fitzpatrick, "Surface-based 3D image registration using the iterative closest-point algorithm with a closest-point transform," in *Proceedings of SPIE*, vol. 2710, p. 358, 1996.

[38] C. Lautensack, "Fitting three-dimensional Laguerre tessellations to foam structures," *Journal of Applied Statistics*, vol. 35, no. 9, pp. 985–995, 2008.

[39] A. Okabe, B. Boots, K. Sugihara, and S. Chiu, *Spatial tessellations*. Wiley Chichester, 2000.

[40] M. Nygårds and P. Gudmundson, "Three-dimensional periodic Voronoi grain models and micromechanical FE-simulations of a two-phase steel," *Computational Materials Science*, vol. 24, no. 4, pp. 513–519, 2002.

[41] K. Zhang, M. Wu, and R. Feng, "Simulation of microplasticity-induced deformation in uniaxially strained ceramics by 3-D Voronoi polycrystal modeling," *International journal of plasticity*, vol. 21, no. 4, pp. 801–834, 2005.

[42] S. Kumar, S. Kurtz, J. Banavar, and M. Sharma, "Properties of a three-dimensional Poisson-Voronoi tesselation: a Monte Carlo study," *Journal of Statistical Physics*, vol. 67, no. 3, pp. 523–551, 1992.

[43] H. Telley, T. Liebling, and A. Mocellin, "The Laguerre model of grain growth in two dimensions I. Cellular structures viewed as dynamical Laguerre tessellations," *Philosophical Magazine Part B*, vol. 73, no. 3, pp. 395–408, 1996.

[44] H. Telley, T. Libeling, and A. Mocellin, "The Laguerre model of grain growth in two dimensions II. Examples of coarsening simulations," *Philosophical Magazine Part B*, vol. 73, no. 3, pp. 409–427, 1996.

[45] X. Xue, F. Righetti, H. Telley, T. Liebling, and A. Mocellin, "The Laguerre model for grain growth in three dimensions," *Philosophical Magazine Part B*, vol. 75, no. 4, pp. 567–585, 1997.

[46] E. Schüle, "A justification of the Hillert distribution by spatial grain growth simulation performed by modifications of Laguerre tessellations," *Computational Materials Science*, vol. 5, no. 4, pp. 277–285, 1996.

[47] M. Kühn and M. Steinhauser, "Modeling and simulation of microstructures using power diagrams: Proof of the concept," *Applied Physics Letters*, vol. 93, p. 034102, 2008.

[48] D. Mika and P. Dawson, "Effects of grain interaction on deformation in polycrystals," *Materials Science and Engineering: A*, vol. 257, no. 1, pp. 62–76, 1998.

[49] P. Rios and M. Glicksman, "Topological and metrical analysis of normal grain growth in three dimensions," *Acta materialia*, vol. 55, no. 5, pp. 1565–1571, 2007.

[50] A. Kak and M. Slaney, *Principles of Computerized Tomographic Imaging.* IEEE Press, 1988.

[51] R. Gordon, R. Bender, and G. T. Herman, "Algebraic Reconstruction Techniques (ART) for three-dimensional electron microscopy and X-ray photography," *Journal of theoretical Biology*, vol. 29, no. 3, pp. 471–481, 1970.

[52] S. Kaczmarz, "Angenäherte auflösung von systemen linearer gleichungen," *Bull. Int. Acad. Polon. Sci. A*, vol. 355, p. 357, 1937.

[53] K. Tanabe, "Projection method for solving a singular system of linear equations and its applications," *Numerische Mathematik*, vol. 17, no. 3, pp. 203–214, 1971.

[54] G. T. Herman, *Fundamentals of computerized tomography: image reconstruction from projections.* Springer Verlag, 2009.

[55] X. Fu, H. F. Poulsen, S. Schmidt, S. F. Nielsen, E. M. Lauridsen, and D. Juul Jensen, "Non-destructive mapping of grains in three dimensions," *Scripta Materialia*, vol. 49, no. 11, pp. 1093–1096, 2003.

[56] X. Fu, E. Knudsen, H. F. Poulsen, G. T. Herman, B. M. Carvalho, and H. Y. Liao, "Optimized algebraic reconstruction technique for generation of grain maps based on three-dimensional x-ray diffraction (3DXRD)," *Optical Engineering*, vol. 45, p. 116501, 2006.

[57] H. F. Poulsen and X. Fu, "Generation of grain maps by an algebraic reconstruction technique," *Journal of Applied Crystallography*, vol. 36, no. 4, pp. 1062–1068, 2003.

[58] P. C. Hansen, H. Sørensen, Z. Sükösd, and H. F. Poulsen, "Reconstruction of single-grain orientation distribution functions for crystalline materials," *Reconstruction*, vol. 2, no. 2, pp. 593–613, 2009.

[59] G. Herman and A. Kuba, *Discrete Tomography: Foundations, Algorithms, and Applications.* Birkhauser, 1999.

[60] G. Herman, A. Kuba, and I. ebrary, *Advances in discrete tomography and its applications.* Citeseer, 2007.

[61] R. J. Gardner, *Geometric tomography.* Cambridge University Press, 2006.

[62] R. Gardner and M. Kiderlen, "A solution to Hammer's X-ray reconstruction problem," *Advances in Mathematics*, vol. 214, no. 1, pp. 323–343, 2007.

[63] L. Kantorovich, "Mathematical methods of organising and planning production (translated from a report in russian, dated 1939)," *Management Science*, vol. 6, no. 4, pp. 366–422, 1960.

[64] G. Danzig, "Linear programming and extensions," *Princeton Univ Pr*, 1963.

[65] J. Von Neumann, O. Morgenstern, A. Rubinstein, and H. Kuhn, *Theory of games and economic behavior*. Princeton Univ Pr, 2007.

[66] R. Vanderbei, *Linear programming: foundations and extensions*. Springer Verlag, 2008.

[67] T. Terlaky, *Interior point methods of mathematical programming*. Kluwer Academic Pub, 1996.

[68] I. CPLEX, "ILOG CPLEX 11.0 User's Manual," *ILOG SA, Gentilly, France*, 2007.

[69] I. CPLEX, "ILOG CPLEX 11.0 File Formats," *ILOG SA, Gentilly, France*, 2007.

[70] K. Mosegaard and A. Tarantola, "Monte Carlo sampling of solutions to inverse problems," *J. geophys. Res*, vol. 100, no. 12, pp. 431–47, 1995.

[71] N. Meteopolis and S. Ulam, "The monte carlo method," *Journal of the American Statistical Association*, vol. 44, no. 247, pp. 335–341, 1949.

[72] K. J. Batenburg and J. Sijbers, "DART: a fast heuristic algebraic reconstruction algorithm for discrete tomography," in *Proceedings of the IEEE International Conference on Image Processing, San Antonio, Texas*, 2007.

[73] A. Schrijver, *Theory of linear and integer programming*. John Wiley & Sons Inc, 1998.

[74] A. Wirgin, "The inverse crime," *Arxiv preprint math-ph/0401050*, 2004.

[75] L. Margulies, G. Winther, and H. Poulsen, "In situ measurement of grain rotation during deformation of polycrystals," *Science*, vol. 291, no. 5512, p. 2392, 2001.

[76] C. Efstathiou, D. Boyce, J. Park, U. Lienert, P. Dawson, and M. Miller, "A method for measuring single-crystal elastic moduli using high-energy X-ray diffraction and a crystal-based finite element model," *Acta Materialia*, vol. 58, no. 17, pp. 5806–5819, 2010.

[77] G. Taylor and H. Quinney, "Plastic deformation of metals," *J. Inst. Metals*, vol. 62, p. 307, 1938.

[78] G. Sachs, "Zur ableitung einer fliessbedingung," *Z. Ver. Dtsch. Ing*, vol. 72, no. 103, pp. 734–736, 1928.

Risø DTU is the National Laboratory for Sustainable Energy. Our research focuses on development of energy technologies and systems with minimal effect on climate, and contributes to innovation, education and policy. Risø DTU has large experimental facilities and interdisciplinary research environments, and includes the national centre for nuclear technologies.

Risø DTU
National Laboratory for Sustainable Energy
Technical University of Denmark

Frederiksborgvej 399
PO Box 49
DK-4000 Roskilde
Denmark
Phone +45 4677 4677
Fax +45 4677 5688

www.risoe.dtu.dk